EFFECTS OF SKEWED ANGLE ABUTMENTS ON THE SEISMIC RESPONSE OF A BRIDGE WITH HYBRID SLIDING-ROCKING COLUMNS

A Thesis

by

HAREESH REDDY GOLI

Submitted to the Office of Graduate and Professional Studies of
Texas A&M University
in partial fulfillment of the requirements for the degree of

MASTER OF SCIENCE

Chair of Committee,	Petros Sideris
Committee Members,	Mary Beth D. Hueste
	Amir Behzadan
Head of Department,	Robin Autenrieth

August 2019

Major Subject: Civil Engineering

ABSTRACT

This study computationally investigates the performance of bridges with hybrid sliding-rocking (HSR) columns and skewed angle seat type abutments, and experimentally explores the frictional response of interfaces for application in HSR joints.

The HSR columns are segmental columns with end rocking joints, intermediate sliding joints (also termed HSR joints) along their length, and internal unbonded posttensioning tendons. A two-span bridge with a single column bent and an original abutment skew of 33º was selected for this study. The original monolithic cast-in-place column bridge and the HSR bridge, i.e. the same bridge with an HSR column instead of monolithic one, were modeled with five different abutment skew angles (0º, 15º, 30º, 45º and 60º) in the OpenSees structural analysis software. Time history analyses were performed on both bridges using the 1994 Northridge Earthquake ground motion for two hazard levels; one with a return period of 1000 years and another with 2500-year return period; termed DE and MCE hazard levels, respectively. The analyses results showed higher demands of column drift, abutment seat length and shear key strength for bridges with abutment skew compared to bridge designs without abutment skew for both monolithic and HSR column bridges. All the analyses results showed a lesser damage to HSR columns than the monolithic column. The damage was in the form of concrete spalling for the HSR column at the MCE hazard level. No tendon yielding was observed for the HSR column.

An experimental program was also carried out to investigate the frictional behavior of PTFE-on-PTFE interfaces that are used in HSR joints. The variation of the coefficient of friction with contact pressure, sliding velocity and type of lubrication was studied by testing four types of specimen. The first two types of specimens had dry concrete-to-concrete interfaces, while the third and fourth specimen types had lubricated interfaces with two different grades of the same grease. Two different sliding and pressure protocols were considered, combining different sequences of pressures and sliding velocities. The contact pressures covered a range between 250 and 2000 psi, while, the peak sliding velocities vary between 0.39 in/sec and 4.71 in/sec. The test results showed that the coefficient of friction decreases with contact pressures and increases with the sliding velocity. Lubrication decreased the coefficient of friction approximately by 50%. A friction model was developed based on the test results that can be used in HSR joint modeling.

DEDICATION

To my parents, Somi Reddy and Sujatha, and my sister, Mounika, for their love and support. No achievements would be possible without their encouragement.

ACKNOWLEDGEMENTS

I would like to gratefully thank my advisor, Dr. Petros Sideris, for his guidance and support throughout the course of this research and for his effort in helping me in experimental testing, modeling and review of this document, and providing financial support to help me with graduation. I also wish to sincerely thank the contribution of my thesis committee members, Dr. Mary Beth D. Hueste and Dr. Amir Behzadan for their guidance and review of this document.

I would like to sincerely thank Ph.D. Candidate Mohammad Salehi Najafabadi for his help with modeling and analyses using OpenSees and with my experimental testing, and for always being there for me to help over the course of this research. I would also like to thank Charlie Droddy and Kirk Martin at the High Bay Structural Testing and Materials Laboratory for their help to successfully execute the frictional testing program. I would also like to thank Ph.D. Candidate Mohammad Taghi Nikoukalam for his help with the Data Acquisition System in the laboratory.

Special thanks to my roommate and friend, Hemant Thurumella, for all his help over the past two years. I wish to thank my family in India for their constant support and encouragement and always believing in me at every step in my career. Finally, I wish to thank all my friends in College Station for making my time at Texas A&M University a memorable one.

CONTRIBUTORS AND FUNDING SOURCES

Contributors

This work was supervised by a thesis committee consisting of Dr. Petros Sideris (advisor) and Dr. Mary Beth D. Hueste of the Department of Civil Engineering and Dr. Amir Behzadan of the Department of Construction Science.

The modeling described in Chapter 3 was developed in part with Ph.D. Candidate Mohammad Salehi Najafabadi and under the guidance of Dr. Sideris. The experimental work described in Chapter 5 was conducted at the Structural and Materials Testing Lab at the Center for Infrastructure Renewal (CIR) facility of the Texas A&M University. The model presented in Chapter 5 was developed under the guidance of Dr. Petros Sideris.

All other work conducted for the thesis was completed by the student independently.

Funding Sources

Partial support for this thesis was provided by the National Science Foundation (CMMI # 1748031). Its contents are solely the responsibility of the authors and do not necessarily represent the official views of the National Science Foundation.

TABLE OF CONTENTS

Page

LIST OF FIGURES

Page

LIST OF TABLES

Page

1. INTRODUCTION

1.1. Problem Statement

Skewed bridges are prone to deck rotation during a seismic event, during which they are subjected to ground motions in multiple directions. The in-plane deck rotation occurs due to the collision of the deck with the abutments or adjacent spans. This induces a torsional moment in the bridge piers, and the combination of axial, flexural, shear and torsional loading decreases the capacity of a reinforced concrete (RC) bridge column.

The use of precast segmental columns post-tensioned with unbonded tendons incorporating hybrid sliding-rocking (HSR) joints could mitigate the seismic damage on bridge piers. These columns have self-centering capabilities and exhibit energy dissipation through sliding at joint interfaces. This torsional joint sliding can prevent damage to the columns. These columns also allow faster construction and could replace monolithic cast-in-place columns in moderate and high seismicity areas.

1.2. Research Objectives and Scope

The objectives of this research are to investigate the effects of HSR columns on the seismic performance of bridges with skew-angled seat-type abutments and compare the damage pattern with that of the monolithic cast-in-place column bridges. Further, an experimental program is conducted to study the frictional properties of the PTFE-on-PTFE interface. The objectives are achieved by performing the following tasks:

- Computational modeling and analyses were performed on a bridge selected from the literature using conventional monolithic column and hybrid sliding-rocking

(HSR) column, and five abutment skew angles (0^o,15^o,30^o,45^o and 60^o) were considered.

- An experimental program was executed on PTFE-on-PTFE (Polytetrafluoroethylene) interface to study the frictional properties, and a numerical model that can be used in HSR joint modeling was developed. The coefficient of friction of the interface was investigated for various normal pressures and sliding velocities.

1.3. Thesis Outline

The thesis is organized as follows: the introduction in Chapter 1 briefly explains the problem statement, objectives and scope of this research. Chapter 2 summarizes the past research and studies carried out in seismic analysis of bridges and experimental testing for evaluation of frictional properties that was helpful in carrying out the research. Chapter 3 describes the physical properties of the case study bridge and its modeling in OpenSees software. Chapter 4 summarizes the various analyses carried on the bridge models, their responses and comparison of the results and damage patterns of monolithic column bridge and HSR column bridge. Chapter 5 describes the experimental study carried out to evaluate the frictional response of PTFE-on-PTFE interfaces. It also summarizes the effects of sliding velocity and normal pressure on the coefficient of friction and describes the proposed numerical model. Finally, Chapter 6 summarizes the whole research and proposes recommendation for future studies based on this research.

2. LITERATURE REVIEW

This section describes the past research on seismic analysis of bridges with skew-angled seat-type abutments, performance of hybrid sliding-rocking column bridges and the effects of combined loading on bridge piers. Previous experimental studies on sliding surfaces used in bridge bearings and seismic isolation is also discussed.

2.1. Seismic Analysis of Skewed Bridges

2.1.1. Description of Skewed Bridges

Bridges are often skewed to maintain a straight alignment of the roadway above or below it and also at intersections where, railway or waterway crossings are not perpendicular to the bridge. The skew angle of a bridge is defined as the angle between a line normal to the centerline of the bridge and the centerline of the support (abutment or pier) as shown in Figure 2.1.

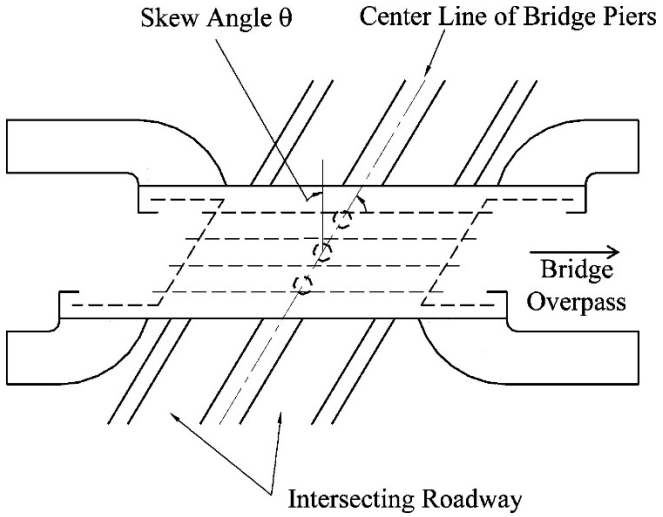

Figure 2.1. Plan view of a bridge with skewed abutments
[reprinted with permission from Wang & Helwig (2008)]

During an earthquake the skewed bridge deck collides with the abutment and possibly rotates about the center of stiffness of the superstructure thereby inducing torsional moment in the bridge piers (Figure 2.2). The combined axial, flexural and shear loading together with the applied torsion decreases the capacity, stiffness and ductility of a reinforced concrete bridge pier.

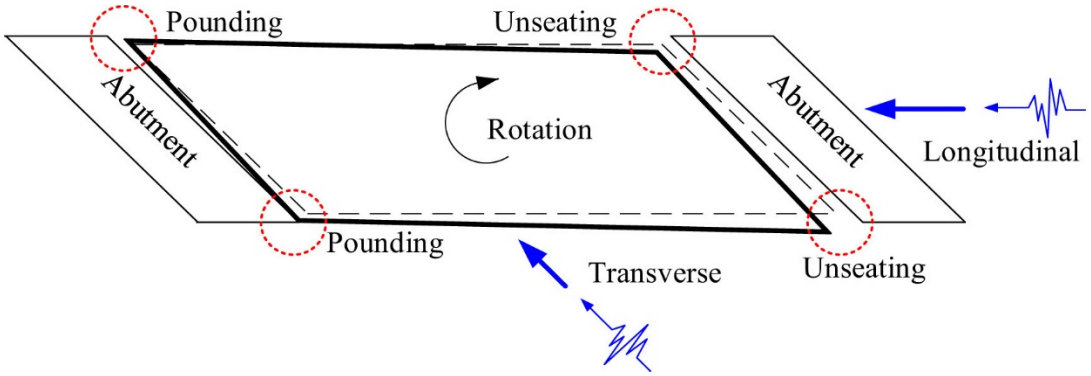

Figure 2.2. Rotation mechanism of skewed bridges
[reprinted with permission from Chen et al. (2017)]

2.1.2. Performance of Skewed Bridges

PEER Report 2014/01 (Kaviani et al., 2014) investigated the performance of bridges with abutment skew. Three bridges were selected from California, one with two spans single column bent, second with two spans two column bent and third with three spans three column per bent as seed bridges. A bridge model matrix was developed with two column heights, symmetric and unsymmetrical spans, and five abutment skew angles (0º,15º,30º,45º and 60º), while three ground motion sets were selected from the PEER (Pacific Earthquake Engineering Research) Transportation Research Program Ground Motion Database with each set consisting of 40 unscaled three-component motions. They

have listed the possible damages of skewed bridges and defined two collapse criteria as maximum column bent drift ratio as 8% and the deck displacement relative to abutment in longitudinal unseating direction is greater than the seat length. The time history analyses were performed in OpenSees and a simplified bridge modeling approach is proposed. The analyses results were categorized into three different damage states 1. Bridge collapse, 2. Bridge survival after shear key failure and 3. Bridge survival with shear key survival. The results reported that the greatest number of collapses were observed with the three-span bridge and all bridges with large abutment skew angles. Peak ground velocity (PGV) which is the maximum of resultant of both horizontal components of the ground motion was opted as the intensity measure (IM). For the no collapse cases, planar deck rotation was considered as one of the engineering demand parameter (EDP) and it was reported that the probability of shear key failure and hence deck rotation have increased with increasing abutment skew angle. The two-span single-column bent bridge was more susceptible to shear key failure and bridges with symmetric span and 0^o skew also rotated due to asymmetric damage in column bents during strong ground motions. It was concluded that the span arrangement had minimal effects on the seismic demands whereas increase in column heights resulted in greater seismic demands.

2.2. Performance of Hybrid Sliding-Rocking (HSR) Columns

In the study by Sideris (2012) and Sideris et al. (2014a, 2014b), a novel precast concrete segmental bridge system was introduced and experimentally investigated. The proposed structure consists of precast segmental columns incorporating hybrid sliding-

rocking joints at segment ends designed to exhibit slip-dominant or rocking-dominant behavior.

2.2.1. Description of HSR Columns

HSR columns were developed as part of an Accelerated Bridge Construction (ABC) technique intended for use in moderate and high seismicity regions. The segments are post-tensioned by high strength unbonded tendons. The end joints are designed to exhibit rocking, whereas the intermediate joints distributed over the column height are designed to exhibit sliding (Figure 2.3). Yet, the intermediate joints can still exhibit rocking, if such a load is applied. In the event of a seismic motion the sliding at joints provides energy dissipation and rocking helps in self-centering of the structure by the use of tendons. Both the top and bottom end joints in an HSR bridge column are provided with sufficiently rough surfaces to attain high friction at the joint and thereby prevent sliding and only allow rocking. Joint sliding is controlled by providing duct adaptors at the joints which are short length tubes with diameter comparatively larger than the tendon ducts.

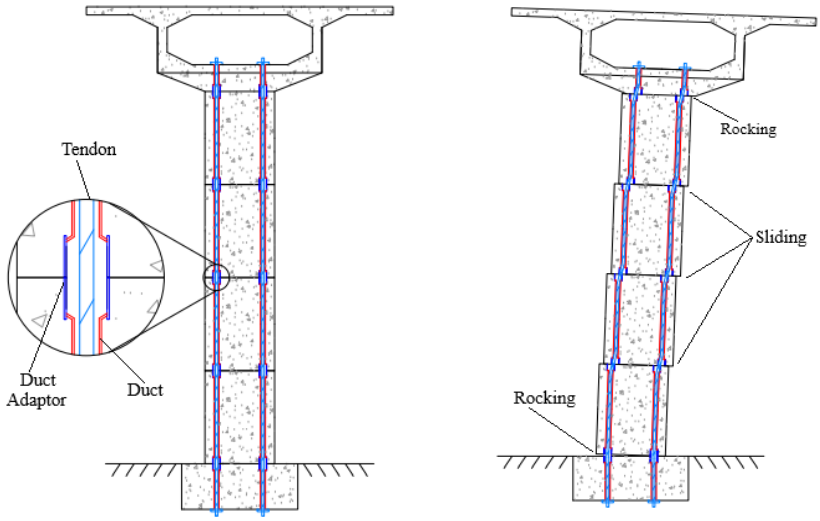

Figure 2.3. HSR bridge column (a) undeformed state; (b) deformed state [adapted from Sideris et al. (2014a)]

2.2.2. HSR Joint Mechanism

For a monotonically increasing horizontal load the intermediate joints which are slip-dominant slide until there maximum capacity is reached. The sliding response can be categorized into two phases: *1.* The initial sliding amplitude until the tendons come into contact with duct, and *2.* The sliding due to the additional gap present between the tendons and duct adaptors at joint ends. Once the sliding capacity is reached the moment at joints increases and a potential rocking response is initiated as shown in Figure 2.4. The rocking is typically limited to the end joints where the moment demand is higher. These joints are not provided with a sliding interface thereby making them rocking dominant. Shear keys can also be used at those joints to further prevent sliding.

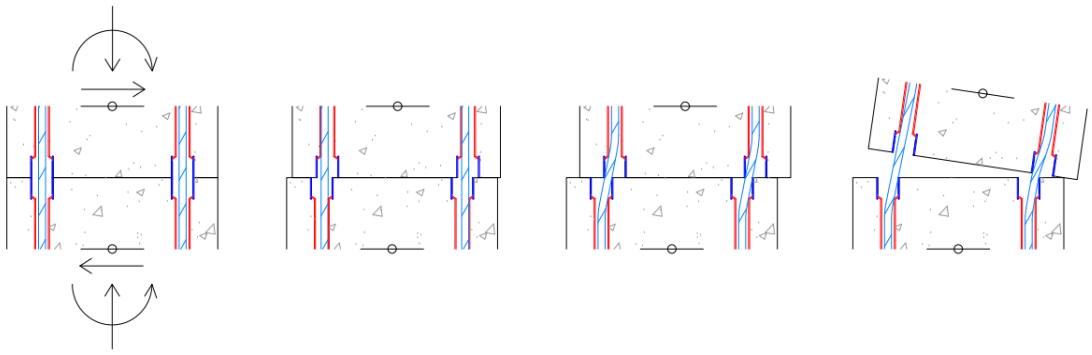

(a) (b) (c) (d)

Figure 2.4. HSR joint response (a) undeformed state; (b) sliding initiation; (c) maximum sliding capacity; (d) rocking [adapted from Sideris et al. (2014a)]

Energy dissipation is provided by the friction at sliding joints while self-centering of the column segments is provided by the tendon bearing forces. The post-tensioned (PT) tendons thereby provide member stability against loading in all directions by offering high resistance against torsional sliding and high flexural strength.

2.2.3. Numerical Modeling of the HSR Columns

2.2.3.1. General

Salehi et al. (2017) developed a novel element formulation for the dynamic analysis of posttensioned segmental columns with HSR joints. A two-node HSR element formulation was proposed which combines a gradient inelastic (GI) flexibility-based (FB) beam-column element which accounts for the member material deformations and joint rocking with a hysteretic friction model which accounts for joint sliding. Rocking is considered within the GI FB formulation through a section with zero tensile strength at the HSR joint.

The GI FB theory developed by Sideris & Salehi (2016) and Salehi & Sideris (2017) eliminates strain localization phenomenon by associating the macroscopic section strains of the strain versus displacement equations with the material or local section strains of the constitutive relations via a set of gradient non locality equations. The gradient nonlocality relations introduce a characteristic length, which is practically an equivalent plastic hinge length and represents the spreading of locally induced damage over its vicinity. In the case of a segmental column with HSR joint the compressive damage due to joint rocking is spread over the characteristic length away from the rocking joint improving the converging properties of the numerical solution. The GI FB element formulation also helps in predicting the section strain field in the vicinity of the HSR joints.

A pressure-dependent hysteretic friction model was developed to simulate the joint sliding at the HSR joint by using a uniaxial plasticity model with constant loading/unloading stiffness with a bounding surface defined as the product of the coefficient of friction and the normal contact stress.

2.2.3.2. Modeling Strategy in OpenSees

The HSR element formulation was implemented in structural analysis program OpenSees (Salehi et al., 2017). Each HSR element had a single sliding-rocking joint and the modeling of an HSR column requires use of one HSR element for each joint in the column. The first node of the HSR element is located in the segment prior to the HSR joint and the second node is located in the segment after the joint with an exception for the bottom joint, where the first node of the HSR element is located at the lower end of the

bottom segment and the second node is located in the same segment above the joint. Similar approach is followed for the upper joint in the top segment. The sliding-rocking joint is placed within the HSR element at its physical location, typically middle of the element in intermediate joints, at the first node for the bottommost joint and second node for the topmost joint.

The interior part of each precast segment was modeled using GI FB beam-column element which is connected to the ends of two HSR elements located the ends of that segment. The length of the HSR element is equal to the length of the duct adaptor. The tendons were modeled using corotational truss elements and the gap between the tendon and duct, and tendon and duct adaptor was simulated using zero-length gap elements which are connected to the HSR element ends using rigid links modeled as elastic beam elements with high stiffness. The tendon material was modeled using a tension-only uniaxial model with Mattock's backbone curve (Mattock, 1979). The potential fracture of tendon was simulated using a damage reduction factor and initial posttensioning force was simulated by assigning an initial strain to the material model. Figure 2.5 summarizes the HSR element formulation and modeling strategy described above.

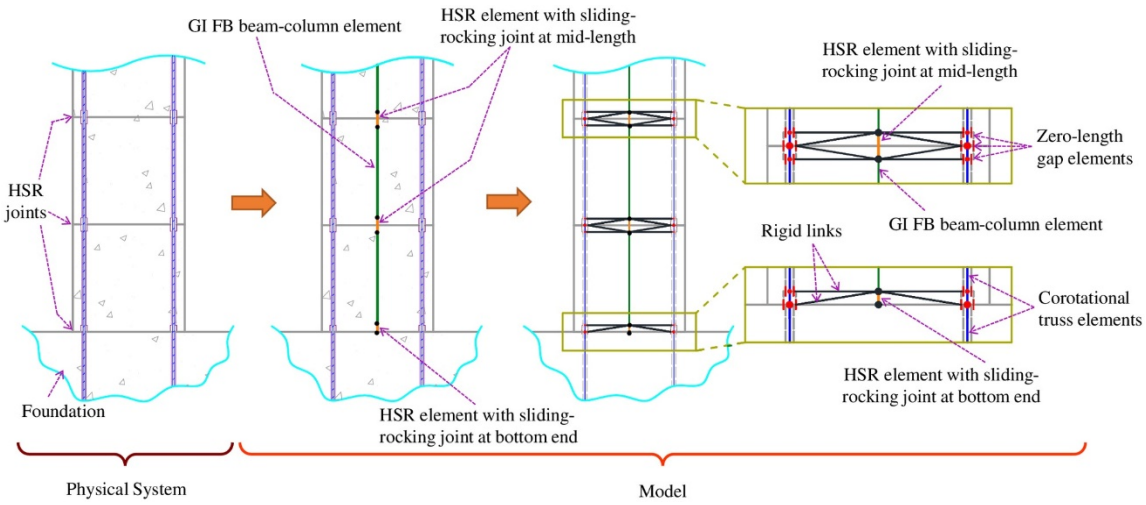

Figure 2.5. Modeling strategy of HSR column
[reprinted with permission from Salehi et al. (2017)]

2.3. Effect of Torsional Loading on Seismic Performance of Bridge Columns

Prakash et al. (2012) carried out experimental research on the torsional effects on seismic performance of square and circular reinforced concrete bridge columns. They stated that bridge columns when subjected to multidirectional ground motions result in a combination of axial force, shearing force, flexural and torsional loading and the significance of torsion increases due to skewed abutments and curved decks. The experiments were conducted on half-scale specimens with loading cases: pure torsion, pure bending, and combination of bending and torsion. A constant axial load, 7% of the column's capacity was applied by unbonded tendons in all the tests. The results reported that the columns tested under flexure and shear developed cracks at the bottom with concrete spalling at 3.2% drift, followed by flexure plastic hinge formation, core degradation and longitudinal rebar buckling at drift ratio of 12.7%. Under pure torsion diagonal cracks developed at the mid height of the column followed by concrete spalling

and formation of torsional plastic hinge. Columns subjected to combined loading failed due to combination of severe shear and flexural cracks followed by concrete cover spalling and core degradation and rebar buckling. The addition of shearing stresses due to both flexural and torsional loading decreased the load resistance capacity of columns.

2.4. PTFE for Sliding Surfaces

2.4.1. General

Polytetrafluoroethylene (PTFE) is the most common material used in sliding surfaces especially in bridge bearings. It is also known by the name Teflon and has one of the lowest coefficients of friction among solids. Its chemical inertness, resistance to water absorption and wearing has made it one the best materials used for sliding bearings and in seismic isolation. Vaziri et al. (1988) conducted an experimental study on PTFE-on-PTFE interfaces to measure the static and dynamic coefficients of friction. The static coefficient of friction was reported as 0.15, while the dynamic coefficient of friction at low sliding velocities (<0.39 in/s) was reported as 0.13.

2.4.2. PTFE in Bridge Bearings

Ala et al. (2015) did experimental study to evaluate the functioning of high-performance sliding surfaces for bridge bearings. They stated a drawback of plain PTFE, where the material wears under high contact pressure, high rates of movement and low temperatures. Experiments were carried out on plain PTFE, Glass-Filled Reinforced PTFE (GFR-PTFE) and Ultrahigh-Molecular-Weight Polyethylene (UMWP) to evaluate their performance at high contact pressure and fast sliding speeds by varying the level of applied pressure, sliding frequency and amplitude. All the materials had stainless steel as their

mating surface. The steel was 0.06 in. thick and highly polished to #8 mirror finish. Contact pressures were varied from 1000 to 5000 psi at a maximum sliding velocity of 25 in/min. Both static and dynamic coefficient of friction (COF) values were reported, where the static value is defined as the initial spike and dynamic COF as the more stable value after the number of cycles increased. Plain PTFE exhibited the lowest values of static friction ranging between 7-8% with dynamic values ranging between 5-6%. GFR-PTFE had static friction ranging between 7-9% and dynamic COF approximately in 6-7% range, the UMWP had large static friction values in 10-17% range and dynamic values in 9-10% range. The test results exhibited a decrease in COF with lubrication and increasing in COF with the increase in number of cycles due to wear. The decrease in COF due to increase in contact pressure was not reported for all the specimen tested. The continual use of same samples for varying pressures was reported as a possible reason for the observed trend. Plain PTFE was subjected to high wearing while GFR-PTFE reported the best overall performance with high wearing resistance and low COF at unlubricated state.

2.4.3. PTFE in Seismic Isolation

Dolce et al. (2005) conducted experimental research on the frictional behavior of steel-PTFE interfaces for use in seismic isolation. Experiments were carried out to check the variability of sliding friction coefficient while varying contact pressure, velocity, air temperature, displacement amplitude, state of lubrication of the interfaces and a numerical model was developed for the mechanical behavior of steel-PTFE sliding bearings. A 5.45 mm thick PTFE sheet with dimpled recesses and 3 mm thick stainless polished to mirror finish with surface roughness less than 0.1 μm were used as sliding surfaces and silicone

grease as lubrication. The contact pressures were varied among 1.35, 2.7 and 4.07 ksi with maximum sliding velocities up to 11.8 in/s at temperatures -10, 20 and 50ºC. The tests were performed at both sinusoidal and saw-tooth motions and similar results were reported for both. Both breakaway and kinetic friction coefficients were observed in the tests. Lubrication produced a decrease in coefficient of friction by up to 8 times at 50ºC and up to 5 times at -10 and 20ºC. The values of COF for non-lubricated interfaces were between 0.08 and 0.2 at large sliding velocities, while the COF for lubricated interfaces was always below 0.04. It was reported that the COF decreases with increase in number of cycles at high sliding velocities and high contact pressures due to self-heating of the interfaces up to a certain extent and later follows a negative trend due to increase in wear. The results showed a rapid increase in COF with increase in velocity up to 6 in/s and later remained almost constant. It was also stated that the COF decreases with increasing contact pressure, while the reduction rate is dependent on the sliding velocity and air temperature.

3. MODELING OF BRIDGE ARCHETYPES

3.1. Introduction

This chapter presents the modeling of monolithic column bridge and HSR column bridge with skewed angle seat-type abutments. A two-span single column bridge (Bridge-A) used in research by Kaviani & Zareian (2014) was selected for this study. The following sections describe the properties of the bridge and analytical modeling of both the bridges: 1. Original bridge with monolithic cast-in-place column and 2. The same bridge with hybrid sliding-rocking (HSR) column.

3.2. Description of Bridge-A

The selected bridge, Jack Tone road on-ramp overcrossing, is located in the city of Ripon, San Joaquin County, California over the state route 99 (Figure 3.1). It is a highway bridge built in 2001 with two spans and a single-column bent and carries two lanes of traffic. The bridge has seat-type abutments with a skew angle of 33°. The superstructure of the bridge is a prestressed concrete continuous three-cell box girder, while the substructure consists of a single reinforced concrete column cast-in-place with a cap beam integral with the deck (Figure 3.2 and Figure 3.3). Each abutment had four elastomeric bearings and both the abutments and the column are supported by steel piles. Table 3.1 lists the detailed properties of Bridge-A taken from structural drawings provided by Caltrans (California Department of Transportation) and PEER Report 2014/01 (Kaviani et al., 2014).

(a)

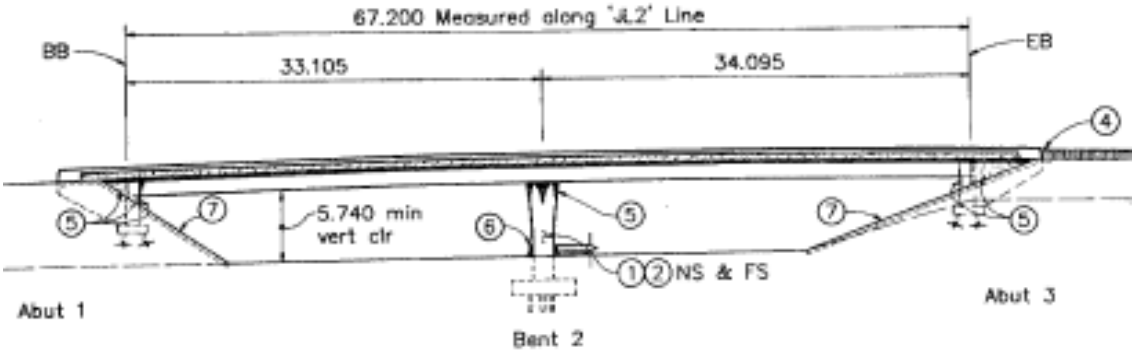

(b)

Figure 3.1. (a) Image of Bridge-A (Google Maps); (b) Elevation view (structural drawings by Caltrans)

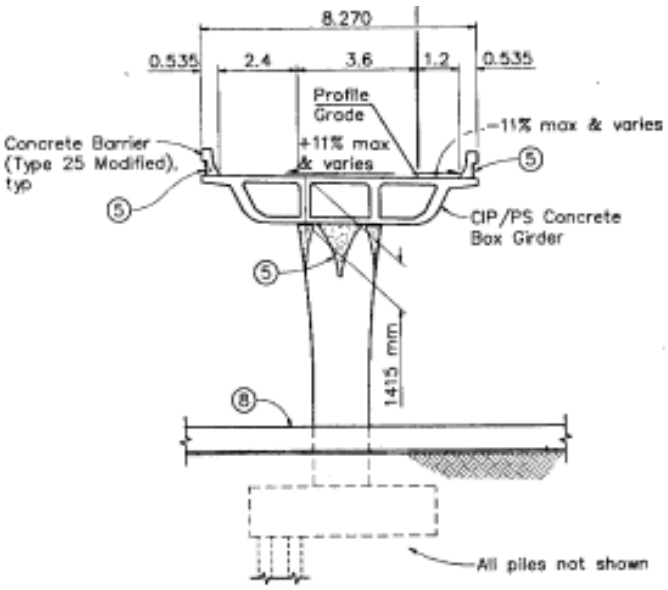

Figure 3.2. Typical section view of Bridge-A (structural drawings by Caltrans)

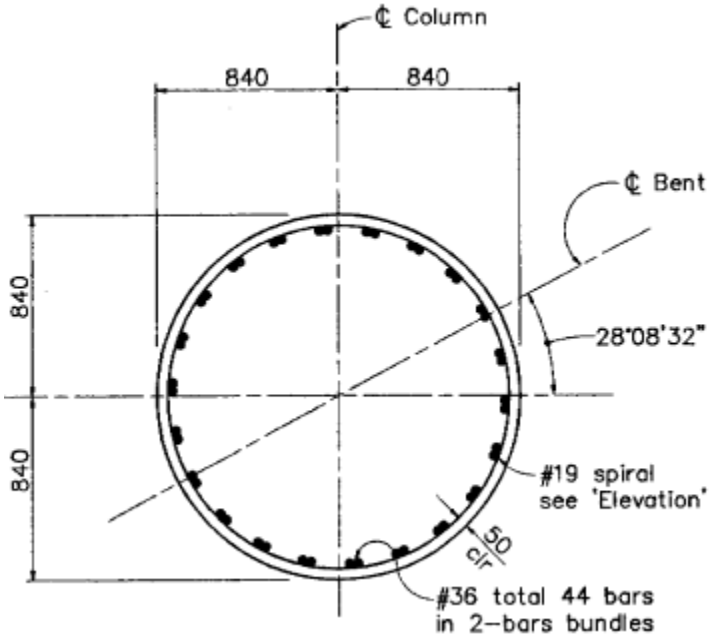

Figure 3.3. Cross-section of Bridge-A column (structural drawings by Caltrans)

Table 3.1. Description of Bridge-A

Bridge location	Jack Tone Road On-Ramp Overcrossing at Ripon, California
National Bridge Inventory (NBI) Location ID	10-SJ-099-2.36-RIP
Structure number	29 0315K
Bridge description	Two span, single column per bent bridge
Skew	33º
Length of the bridge	220.4 ft
Span details	Left span length-108.58 ft., Right-111.82 ft.
Column height	19.68 ft.
Column diameter	5.51 ft.
Deck centroid height (from top of the column)	2.48 ft.
Deck width	27.13 ft.

Table.3.1. Continued

Deck depth	4.64 ft.
Deck cross sectional properties	A=97.546 ft^2, J=341.442 ft^4 I_z=180.328 ft^4, I_y=3797.9 ft^4,
Boundary conditions	Fixed foundation
Bearing pads per Abutment	4 (elastomeric bearing pads)
Concrete and Reinforcement details of column bent	Concrete: f'_c = 4 ksi (28 MPa) Steel: f_y = 60 ksi (420 MPa) -ASTM A706 Longitudinal reinforcement: 44#11 (bundles of 2), ρ_l=2% Transverse reinforcement: Spiral, #6 @3.34 in.

3.3. Description of HSR Column

The HSR column was designed for a lateral strength of 550 kips, with an ultimate sliding capacity of 1.65% drift which was assumed close to the design earthquake drift demand. The designed HSR column had three precast segments, with four sliding-rocking joints as shown in Figure 3.4 and a hollow cross-section as shown in Figure 3.5. The top and bottommost joints were rocking-dominant joints with concrete-on-concrete interfaces with high coefficient of friction. Both intermediate joints were sliding-dominant joints with PTFE-on-PTFE interfaces with very low coefficient of friction. The height and diameter of duct adaptors and the coefficient of friction for sliding joints were chosen as per the guidelines in Sideris et al. (2014). Detailed description of the column is shown in Table 3.2. The design of HSR column is not discussed in detail here as it is beyond the scope of this study.

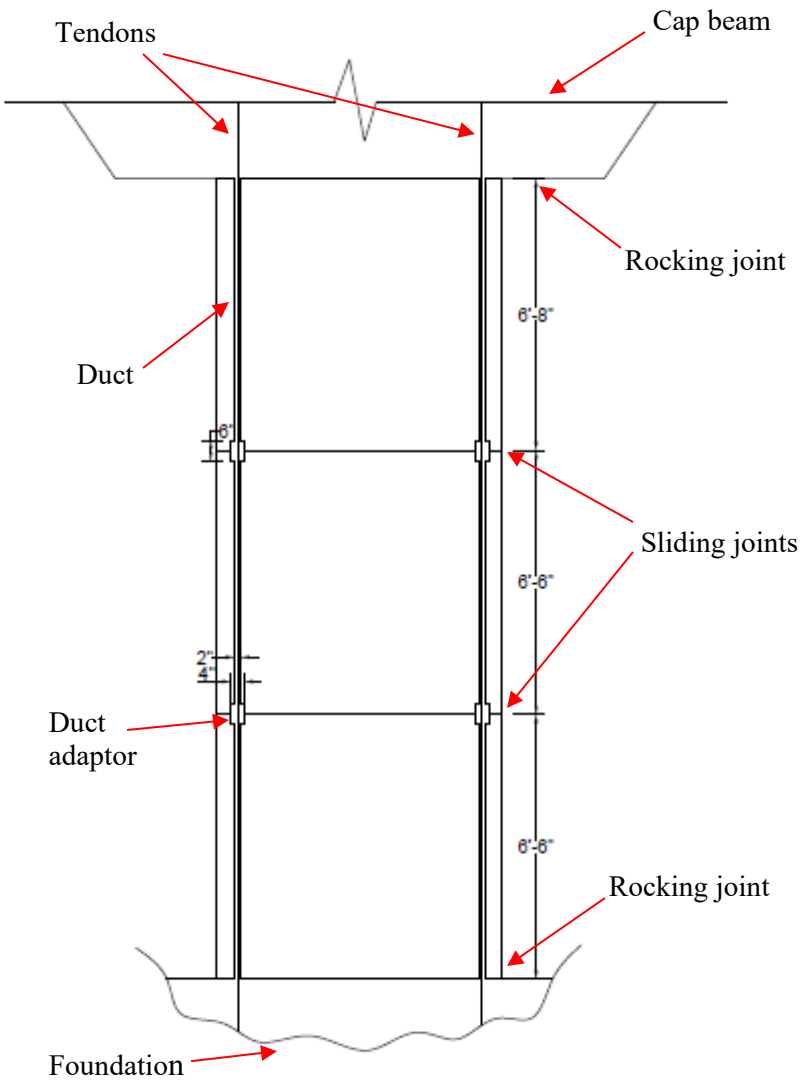

Figure 3.4. Schematic section view of the HSR column for Bridge-A

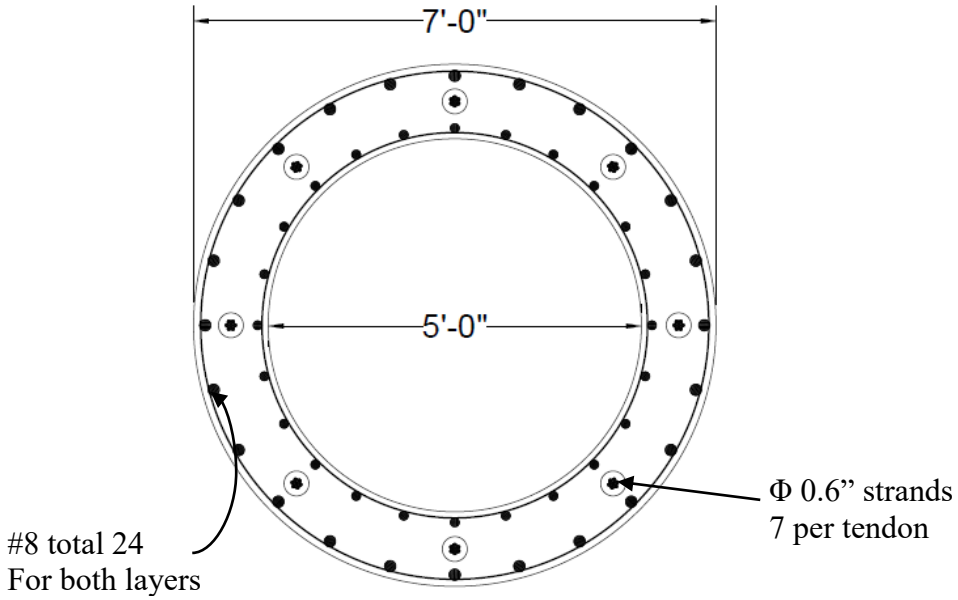

Figure 3.5. Cross-section of HSR column

Table 3.2. Details of the HSR column

Column height	19.68 ft.
Number of segments	3
Height of individual segments (from bottom)	6.5 ft, 6.5 ft, 6.68 ft
Deck centroid height (from top of the column)	2.48 ft.
Outer radius of column	3.5 ft.
Inner radius of column	2.5 ft.
Duct diameter	2 in.
Duct adaptor diameter	4 in.
Duct adaptor height	6 in.

Table 3.2. Continued

Concrete and Reinforcement details	Concrete: f'c = 8 ksi (55 MPa) Mild Steel: fy = 60 ksi (420 MPa) -ASTM A706 Longitudinal reinforcement: 24 #8 (per circular layer) PT steel: 8 tendons, 0.6" diameter strands (7 per tendon)
Distance between column top and top tendon anchorage point	2 ft.
Depth of tendon anchors in footing	2 ft.

3.4. Analytical Modeling of Bridges

3.4.1. Introduction

The bridge models, both with monolithic column and HSR column were developed in OpenSees (Open System for Earthquake Engineering Simulation) software, a nonlinear finite element program developed for simulating the seismic response of structural and geotechnical systems (McKenna et al., 2000). A version of the software upgraded with new and modified material models and elements (Salehi & Sideris, 2017; Salehi et al., 2017) was used. The bridges were modeled in accordance with the Guidelines for Nonlinear Analysis of Bridge Structures in California (Aviram et al., 2008) and Chapter 4 of Bridge Design and Practice by Caltrans (Caltrans, 2015). Detailed description of modeling is explained in the following sections.

3.4.2. Nodes and Mass Assignment

The bridges were modeled in three dimensions with six degrees of freedom using a spine-type model along the centroid of bridge components. The bridge components were divided into adequate segments for better distribution of mass and prediction of fundamental mode shapes. Both translational and rotational mass (mass moment of inertia) were assigned to all the nodes along the deck as lumped mass.

The masses were calculated using Eq. (3-1).

$$M = \rho_m AL \tag{3-1}$$

where:

ρ_m is the concrete unit mass $\left(\rho_m = \frac{\rho_w}{g}\right)$

ρ_w is the unit weight of pre/post tensioned reinforced concrete =165 lb/ft^3

g is the acceleration due to gravity (ft/s^2)

A is the cross-sectional area (ft^2)

L is the tributary length corresponding to the node (ft)

The rotational masses (moment of inertia) were calculated using the following equations

$$M_{xx} = \rho_m JL \tag{3-2}$$

$$M_{yy} = \rho_m \left(\frac{AL^3}{12} + I_y L\right) \tag{3-3}$$

$$M_{zz} = \rho_m \left(\frac{AL^3}{12} + I_z L\right) \tag{3-4}$$

where:

x is the longitudinal axis joining the nodes while y and z are the axis in the plane of cross section in the local coordinate system of the segments

I_y and I_z are the second moment of area about y and z axis respectively (ft^4)

J is the polar moment of inertia/torsional constant of the segment (ft^4)

3.4.3. Super Structure Modeling

The super structure elements in the bridges are continuous box girders and were modeled as elastic beam-column elements.

3.4.4. Column-Bent Modeling

3.4.4.1. Monolithic Column

Columns are considered as the most critical components of a bridge in the event of an earthquake. These components are likely to exhibit nonlinear response and they were modeled using a gradient inelastic flexibility-based (GI FB) beam-column element (Salehi & Sideris, 2017; Sideris & Salehi, 2016). A single element with a height equal to the column height was used.

The column's cross section was modeled as a fiber section where the cross section was discretized in both angular and radial directions as shown in Figure 3.6. Different material properties were assigned to confined (core) and unconfined (cover) concrete. The material properties used in column modeling are listed in the following sections.

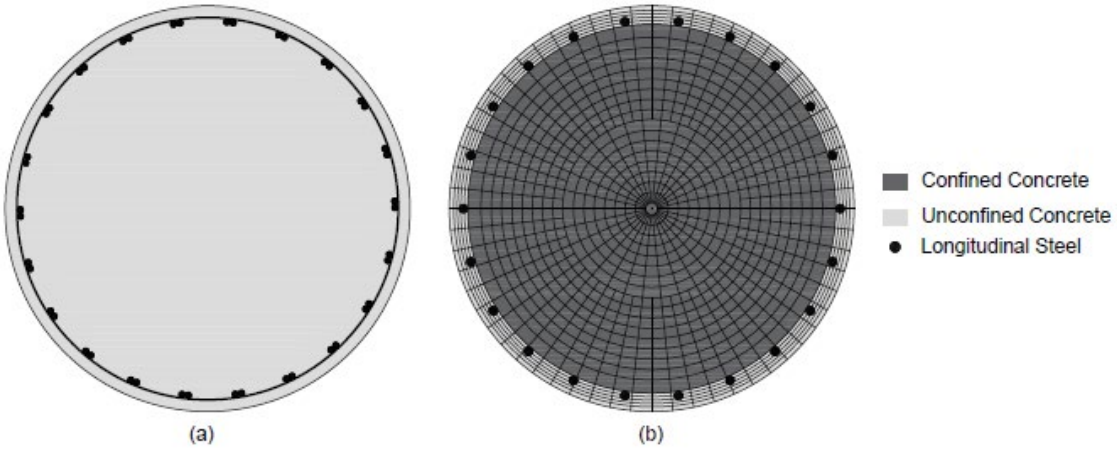

Figure 3.6. Monolithic column's cross-section: (a) archetype cross-section; (b) fiber discretization

Concrete Material Model

The OpenSees uniaxial material model *Concrete01* was used to represent both unconfined and confined concrete. This material model constructs a uniaxial Kent-Scott-Park concrete material object with degraded linear unloading/reloading stiffness according to the work of Karsan-Jirsa and considers no tensile strength.

The properties used in defining this model were calculated per Mander et al. (1988) and Karthik & Mander (2010). The expected material properties were used in the modeling instead of the nominal values according to the guidelines in Caltrans Seismic Design Criteria (Caltrans, 2013), as shown in Table 3.3. The modified material command, which incorporated the response post crushing strength of concrete was used. A residual stress of zero and one percent were used for cover and core concrete respectively as shown in Figure 3.7.

Table 3.3. Monolithic column: concrete material properties

Concrete properties		**Unconfined (cover concrete)**	**Confined (core section)**
fpc	compressive strength at 28 days *(ksi)*	5.27	7.07
epsc0	concrete strain at maximum strength	0.002	0.0054
fpcU	concrete crushing strength *(ksi)*	1.74	3.53
epscU	concrete strain at crushing strength	0.0036	0.027

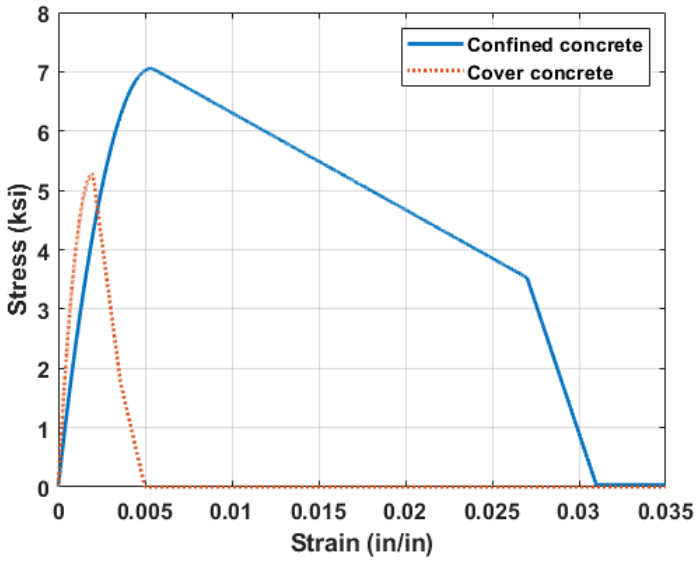

Figure 3.7. Monolithic column: concrete stress-strain backbone curves

Steel Material Model

The uniaxial material model *Steel02* was used to represent longitudinal rebars. This model constructs a uniaxial Giuffre-Menegotto-Pinto steel material model, while it

was further modified to include strength and stiffness deteriorations through implementation of a damage reduction factor. The expected mechanical properties were used in defining the model (Table 3.4). The material behavior is shown in Figure 3.8.

Table 3.4. Monolithic column: steel material properties

Longitudinal steel properties		
fy	yield strength	68 *ksi*
Eo	initial elastic tangent	29000 *ksi*
b	strain hardening ratio	0.01
eps1	strain at which deterioration starts	0.12
eps2	strain at which deterioration ends	0.15
rf_min	minimum strength deterioration ratio	0.01

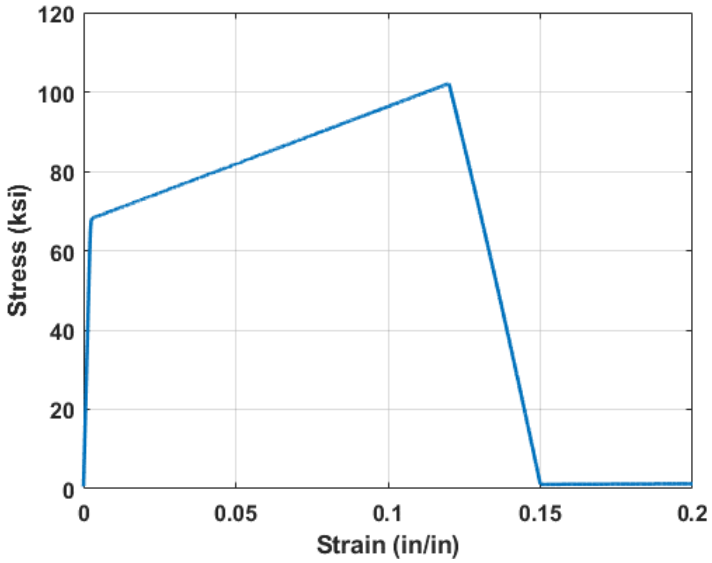

Figure 3.8. Monolithic column: steel material stress-strain backbone curve

Shear and Torsion

The uniaxial material model *Hysteretic* is used to represent the overall shear force vs. shear strain and torsion vs. torsional curvature responses of each cross-section of the monolithic column. This material model produces a uniaxial trilinear hysteretic response with pinching of force and deformation, damage due to ductility and energy, and degraded unloading stiffness based on ductility.

Nonlinear hysteretic models were used in defining both the torsional and shear responses of the column to more accurately predict the column's response under combined axial, torsional, flexural and shear loading during an earthquake. These material models were aggregated with the fiber sections described earlier. Improved Softened Truss Model (Mondal & Prakash, 2015) was used to predict the analytical torsion and shear responses of the column and three points were manually chosen in defining the hysteretic models as shown in Figure 3.9 and Figure 3.10.

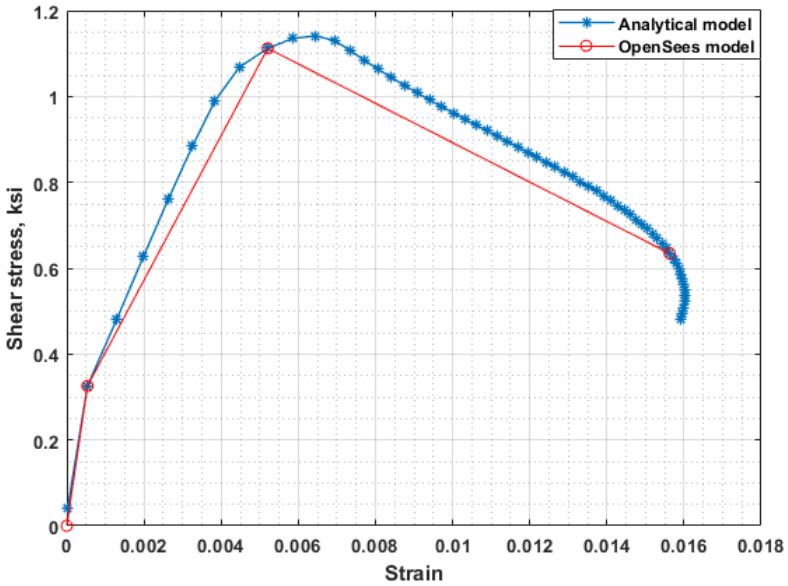

Figure 3.9. Monolithic column: shear force vs. shear strain backbone curve

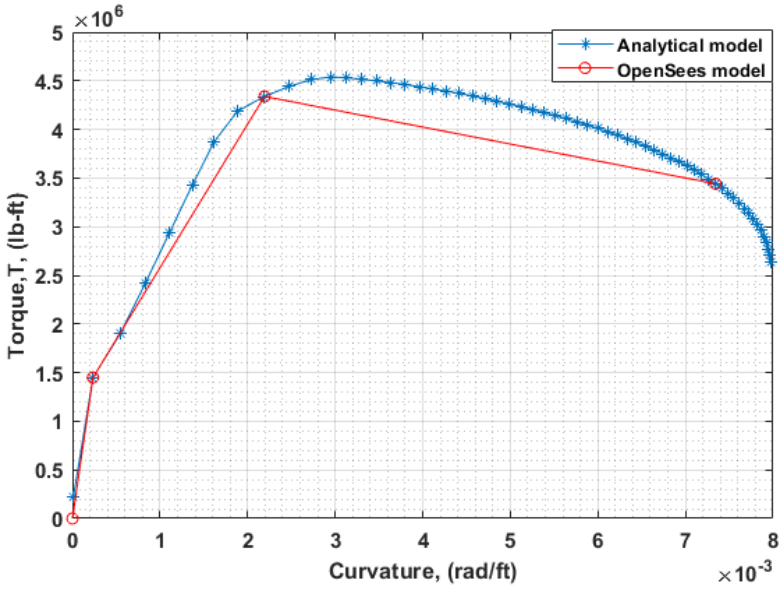

Figure 3.10. Monolithic column: torsion vs. torsional curvature backbone curve

3.4.4.2. HSR Column

HSR column was modeled using the modeling strategy proposed by Salehi et al. (2017). The schematic element configuration used to simulate the HSR column is shown in Figure 3.11. All the elements employed co-rotational formulation to capture the finite rotation effects. The modeling of each component of the HSR column is separately described in the following sections.

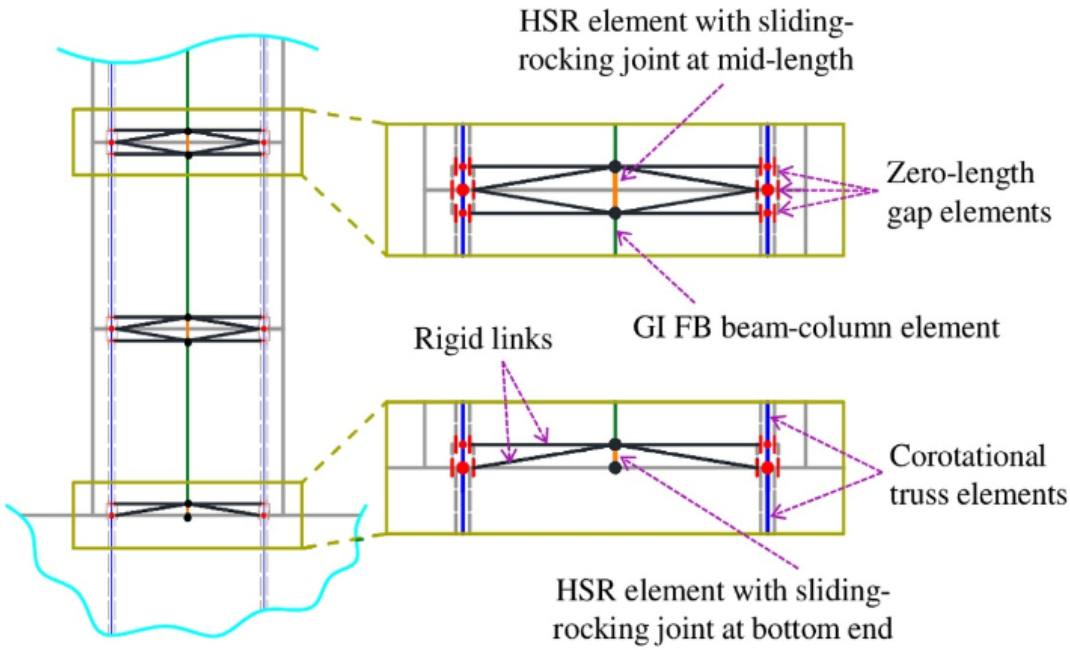

Figure 3.11. Schematic element configuration of HSR column
[reprinted with permission from Salehi et al. (2017)]

Modeling of Joints

Each joint and its close vicinity was modeled using an HSR element (Salehi et al., 2017). The HSR element spanned along the heights of duct adaptors and utilized fiber sections representing the column's hollow cross-section (Figure 3.12). A pressure dependent friction model with a maximum coefficient of friction as 0.17 was used in defining the sliding joints of HSR column as shown in Figure 3.13.

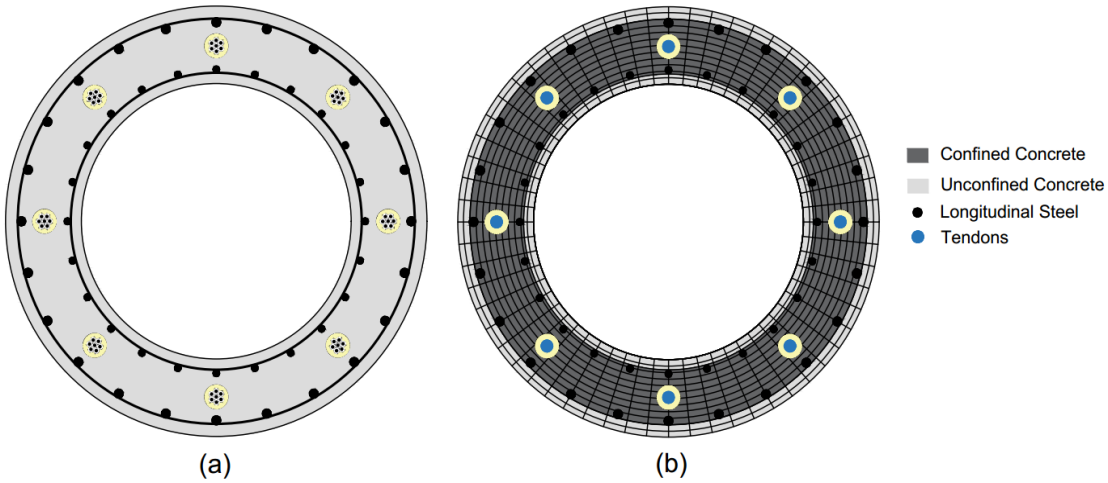

Figure 3.12. HSR column's cross-section: (a) archetype cross-section; (b) fiber discretization and tendons

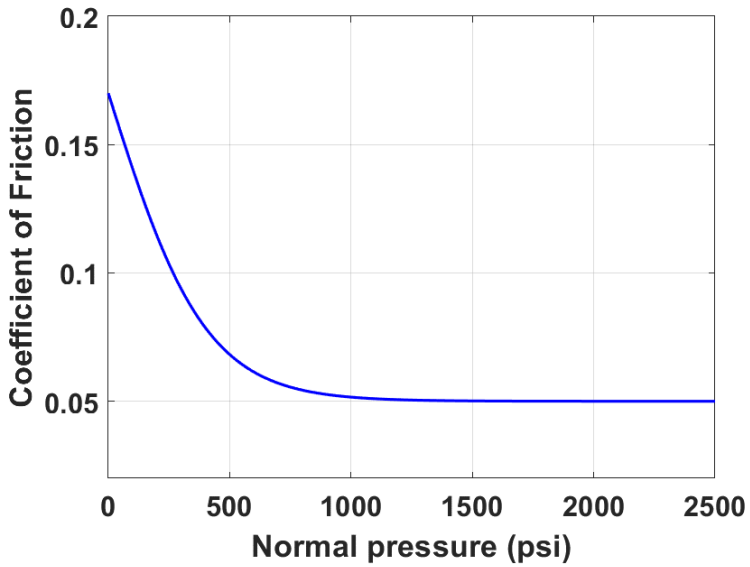

Figure 3.13. Variation of coefficient of friction with normal pressure at sliding joints

Modeling of Precast Segments

The interior part of each precast segment was modeled using a gradient-inelastic flexibility-based (GI FB) beam column element with its ends connected to the HSR elements. Similar concrete material model used in monolithic column modeling was used

in defining the core and cover concrete of the precast segmental columns with the properties mentioned in Table 3.5 and the material behaviors shown in Figure 3.14. The mild steel reinforcement was modeled using the same properties as mentioned in Table 3.4.

Table 3.5. HSR column: concrete material properties

Concrete properties		**Unconfined (cover concrete)**	**Confined (core section)**
fpc	compressive strength at 28 days *(ksi)*	8	10.4
epsc0	concrete strain at maximum strength	0.002	0.005
fpcU	concrete crushing strength *(ksi)*	1.74	4.86
epscU	concrete strain at crushing strength	0.0036	0.025

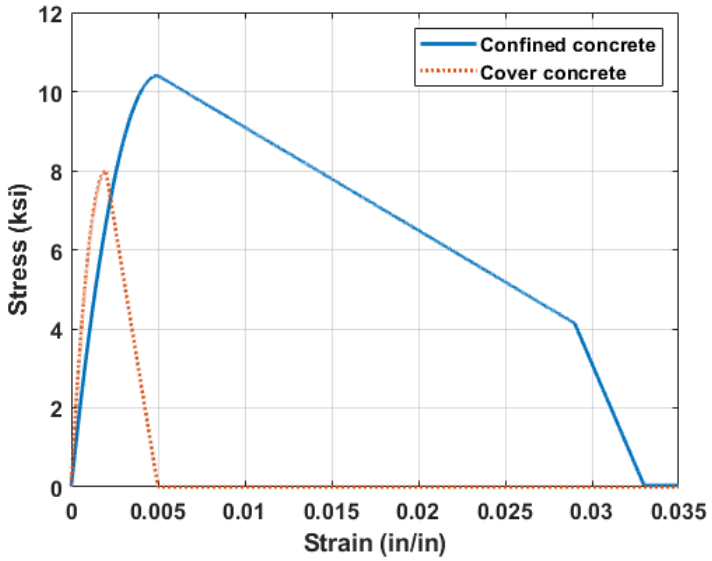

Figure 3.14. HSR column: concrete material behavior

Modeling of Tendons

Tendons were modeled using the so-called continuous multi-node truss elements with a cross-section area equal to the combined area of all strands. The uniaxial material model *PTSteel*, developed in accordance with Mattock (1979), was used to simulate the high-strength steel behavior. This material model does not withstand compression and also incorporates an initial strain to produce initial posttensioning stress. The model further uses a damage reduction factor for simulating the potential fracture in tendon (Figure 3.15). The properties used to define the PTSteel material model are listed in Table 3.6.

The lateral movement of tendons within the duct and duct adaptors was constrained using zero length gap elements which were connected to the HSR element ends using rigid links.

Table 3.6. HSR column: tendon material properties

Tendon material properties		
fy	yield strength	243 *ksi*
E	initial elastic tangent	28500 *ksi*
ry	strain hardening ratio	0.015
eps1	strain at which deterioration starts	0.025
eps2	strain at which deterioration ends	0.09
rf_min	minimum strength deterioration ratio	0.01
Fpt	initial post-tensioning force per tendon	140 kips

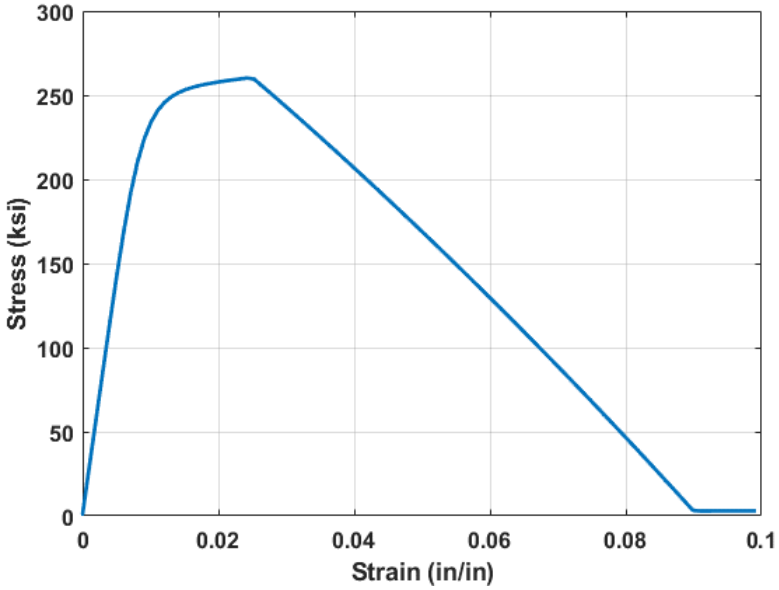

Figure 3.15. HSR Column: Post-tensioning steel behavior

3.4.5. Abutment Modeling

The simplified approach proposed by Kaviani & Zareian (2014) with some modification was used in the modeling of abutments in the bridge models. According to this approach, each abutment was modeled as a rigid massless element divided into segments of uniform lengths on either side of the bridge superstructure's center line. The abutment's behavior in longitudinal, transverse and vertical directions was modeled using zero-length springs in the respective directions.

3.4.5.1. Longitudinal Abutment Response

In the longitudinal direction, the gap between superstructure and backwall (expansion joint), and backfill passive response were represented by the hyperbolic gap uniaxial material model. The direction of backfill response was assumed perpendicular to the abutment backwall for all skew angles. The guidelines specified by Caltrans for

abutment modeling were used in defining the material properties (Caltrans, 2013). The initial embankment stiffness, K_i, was given by

$$K_i = \frac{50\ kip/in}{ft} \tag{3-5}$$

The initial stiffness was later adjusted proportional to the backwall width and height, given by Eq. (3-6):

$$K_{abt} = K_i * w * \left(\frac{h}{5.5\ ft}\right) \tag{3-6}$$

where:

w is the width of the abutment backwall segment (ft)

h is the height of the backwall (ft) (assumed three times the depth of deck)

The ultimate longitudinal force capacity (in kips) of the abutment was given by:

$$P_{bw} = (h * w) * 5.0\ ksf * \left(\frac{h}{5.5\ ft}\right) \tag{3-7}$$

The overall bilinear response of the abutment in the longitudinal direction was idealized as shown in Figure 3.16.

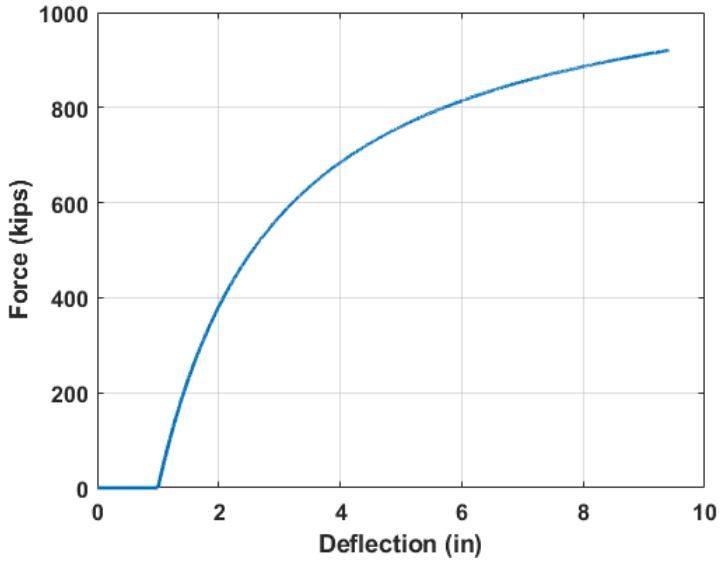

Figure 3.16. Abutment: Longitudinal response

The strength/stiffness variation due to the skew angle was considered by multiplying a factor β defined by Kaviani & Zareian (2014) for a skew angle α, which is given by the following equation:

$$\beta = 0.3\left(\frac{tan \propto}{tan\, 60^o}\right) \tag{3-8}$$

3.4.5.2. Transverse Abutment Response

The exterior shear keys were assumed to have a trilinear backbone curve, which degrades to zero strength upon reaching the failure deformation. The capacity of the shear key calculated using strut-and-tie method by Kaviani & Zareian (2014) was used in defining the shear key response.

The uniaxial material model *Concrete02* was used to represent the shear force vs. deformation of the shear keys as shown in Figure 3.17. The values considered for the arguments defining this model are listed in Table 3.7.

Table 3.7. Abutment: shear key properties

Material properties		Bridge A
fpc	Ultimate strength	756 kips
epsc0	Deformation at ultimate strength	1 in
fpcU	Strength at crushing	0.0
epscU	Deformation at crushing strength	2.45 in
lambda	Ratio between unloading and initial slope	0.2

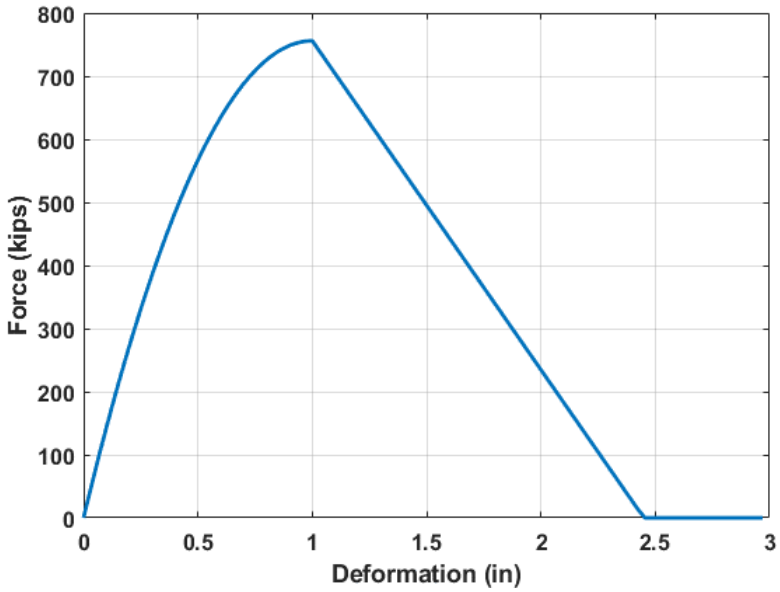

Figure 3.17. Abutment: shear key force-deformation backbone curve

The four shear keys in the bridge model were labeled as left near, left far, right near and right far as shown in Figure 3.19.

3.4.5.3. Vertical Abutment response

The vertical response of the abutment was modeled using two springs in parallel (Figure 3.18), one representing the bearing pad with stiffness K_1 and the other representing the rigid stem wall with stiffness K_2. The response of the stem wall was modeled using an

elastic perfectly plastic gap material model and the response of the bearing pads was modeled using an elastic no-tension material. The bearing height was assigned as the gap value in the stem wall material model.

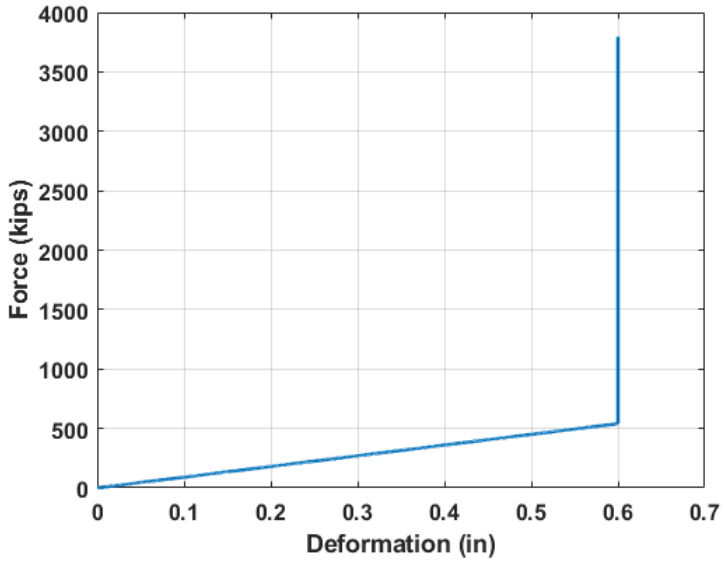

Figure 3.18. Abutment: vertical response

3.4.6. Inherent Damping

Rayleigh damping with 5% damping ratios for the first two modes was considered in the models. Per this model, the classical damping matrix, $[c]$, is given by (3-9) (Chopra, 2012)

$$[c] = a_0[m] + a_1[k] \tag{3-9}$$

where:

$[m]$ and $[k]$ are the mass and stiffness matrices

a_0 and a_1 are the constants corresponding to mass- and stiffness-proportional damping terms, respectively

The damping ratio for the *n*th mode can be calculated as

$$\zeta_n = \frac{a_0}{2}\frac{1}{\omega_n} + \frac{a_1}{2}\omega_n \tag{3-10}$$

By assuming the same damping ratio for first two modes, the constants a_0 and a_1 were found by

$$a_0 = \zeta\frac{2\omega_1\omega_2}{\omega_1 + \omega_2} \tag{3-11}$$

$$a_1 = \zeta\frac{2}{\omega_1 + \omega_2} \tag{3-12}$$

where:

ω_1 and ω_2 are the frequencies corresponding to first two modes of the bridge.

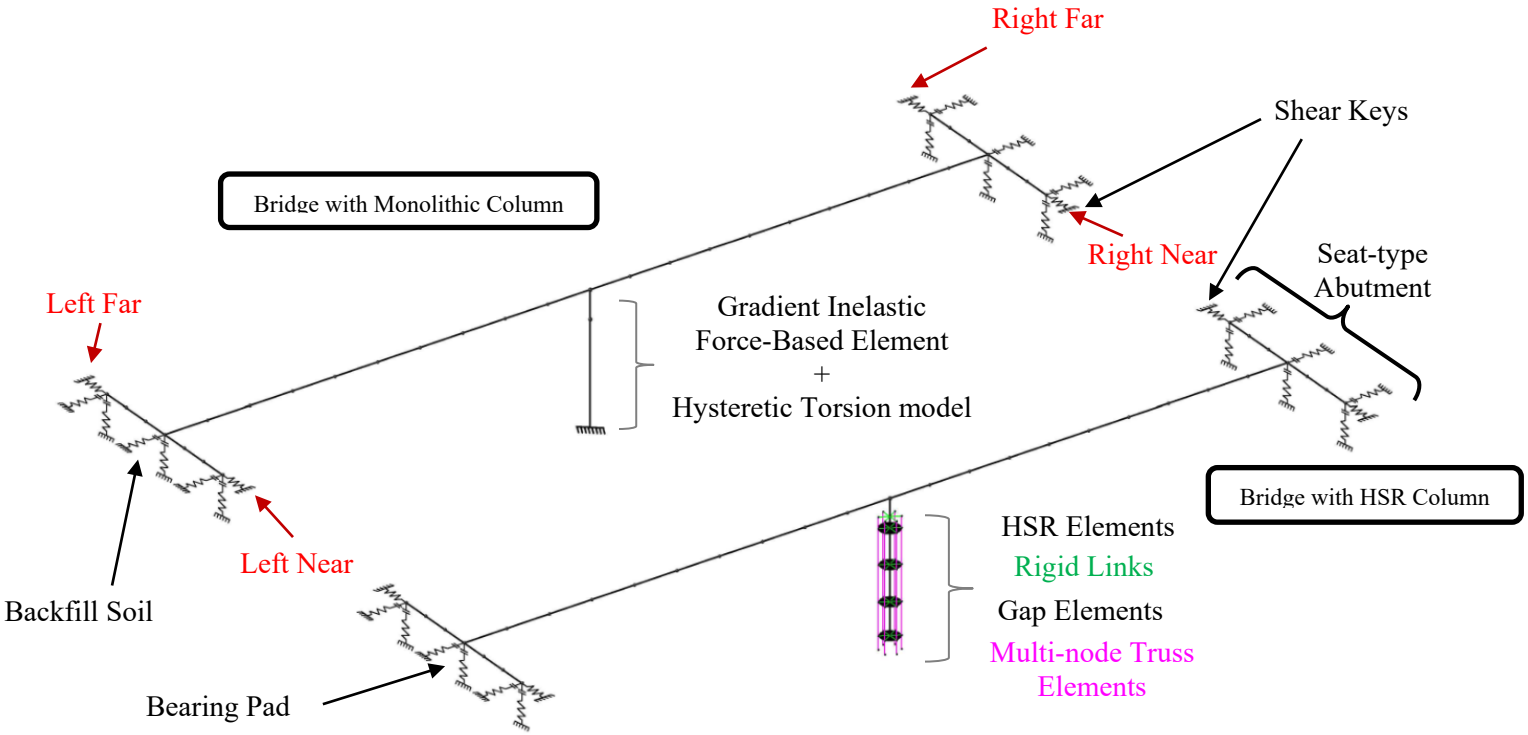

Figure 3.19. Schematic model of the bridges in OpenSees

4. ANALYSES OF THE BRIDGE MODELS

4.1. Introduction

This section describes the analysis carried out on the OpenSees bridge models and the general responses of both bridges with monolithic column and HSR column with various abutment skew angles are compared. The damage patterns of both the bridge models are stated and their performance is compared for two hazard levels.

4.2. Modal Analysis

Modal analysis is carried out initially to identify the fundamental frequencies of the bridge structure and their corresponding mode shapes. Table 4.1 summarizes the first six natural time periods of the monolithic column bridge. It can be observed that the abutment skew angle does not have a significant effect on the fundamental time periods, and the time periods decrease with an increasing abutment skew angle.

Table 4.2 summarizes the fundamental time periods of HSR column bridge. Unlike the monolithic column bridge the time periods of HSR bridge increase with an increase in abutment skew angle. However, the fundamental mode shapes of both the bridges are similar with the translational modes in longitudinal lateral direction of bridge being dominant. Figure 4.1 shows the typical first six mode shapes observed in monolithic column bridge and HSR column bridge models.

Table 4.1. Fundamental time periods of Bridge-A with monolithic column

Mode	Abutment Skew Angle				
	0º	**15º**	**30º**	**45º**	**60º**
1st	0.598843	0.597897	0.594564	0.586818	0.568731
2nd	0.368631	0.370964	0.373903	0.376649	0.377726
3rd	0.366628	0.363809	0.359027	0.351546	0.338487
4th	0.350649	0.349593	0.346051	0.338498	0.322475
5th	0.221392	0.221387	0.221368	0.221325	0.221221
6th	0.141502	0.141458	0.141303	0.140925	0.139932

Table 4.2. Fundamental time periods of Bridge-A with HSR column

Mode	Abutment Skew Angle				
	0º	**15º**	**30º**	**45º**	**60º**
1st	0.546574	0.549149	0.565163	0.688583	0.744368
2nd	0.351018	0.358805	0.386707	0.470435	0.554642
3rd	0.346175	0.345055	0.349307	0.442497	0.45267
4th	0.322854	0.326355	0.338151	0.340811	0.345633
5th	0.216361	0.21723	0.219722	0.264903	0.275623
6th	0.131299	0.140643	0.19122	0.22755	0.232594

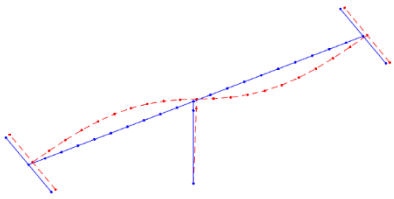

1st Mode

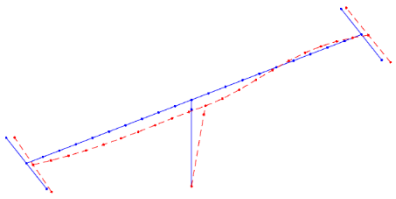

2nd Mode

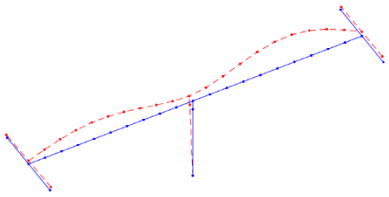

3rd Mode

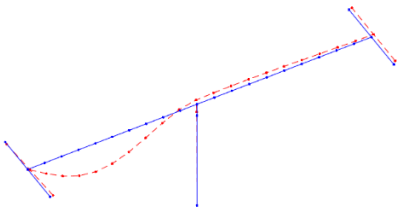

4th Mode

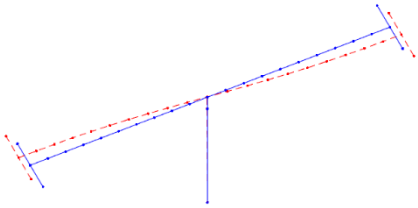

5th Mode

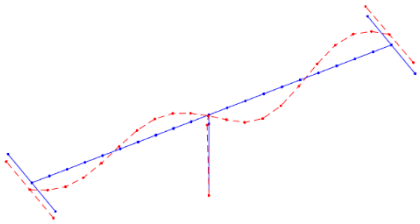

6th Mode

Figure 4.1. Fundamental mode shapes of Bridge-A with 30º abutment skew

4.3. Analyses on Cantilever Column

4.3.1. Quasi-Static Pushover

A quasi-static push over analysis was performed on both the monolithic and HSR column alone to check and compare their behavior. An axial load equivalent to the load applied on the column due to the bridge superstructure was applied during the pushover. Figure 4.2 shows the comparison of pushover curves for both the columns. The initiation of sliding is evident in the pushover curve of HSR column at a shear of approximately 150 kips. The shear of HSR column is always lower than that of the monolithic column at any given drift, after the initiation of sliding.

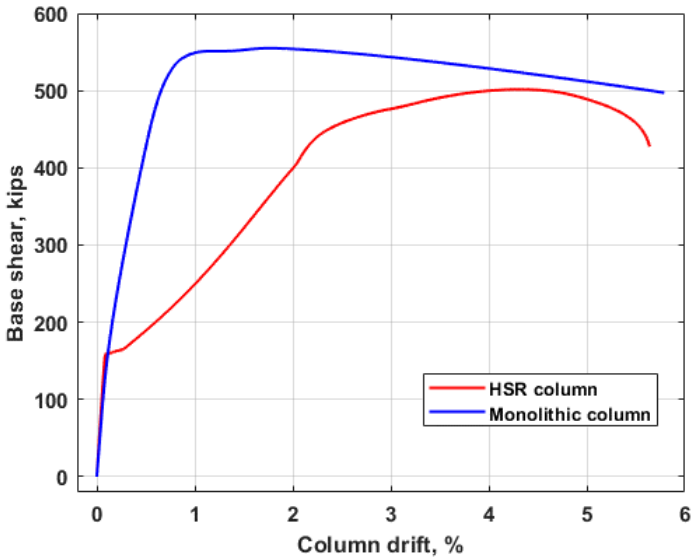

Figure 4.2. Comparison of pushover curves of monolithic and HSR cantilever columns

4.3.2. Quasi-Static Cyclic Loading

A quasi-static cyclic loading was applied about the vertical axis of the columns to check and compare their torsional responses. A trilinear hysteretic model was used for

modeling the torsional behavior of monolithic column, while a linear elastic model was used in the modeling of HSR column. Figure 4.3 shows the response of both the columns for applied loading pattern. The torsional response for HSR column is comparatively much lower than the monolithic column due to sliding and rotation at HSR joints of the individual segments in the column.

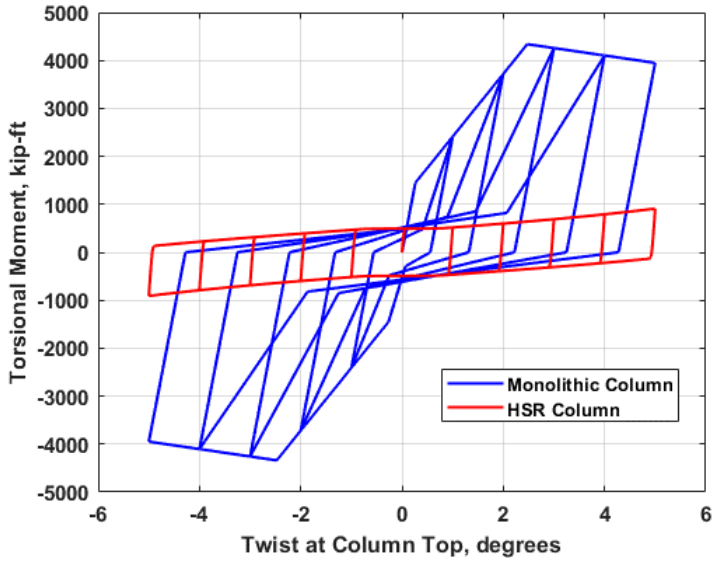

Figure 4.3. Comparison of torsional response of monolithic and HSR cantilever columns

4.4. Time History Analyses

4.4.1. Design Spectrum

The 5%-damped design response spectrum was generated for the bridge site based on the guidelines specified in AASHTO-LRFD-2012-Bridge-Design-Specifications-6th-Ed (AASHTO, 2012). The spectrum was determined as shown in Figure 4.4, using the mapped peak ground acceleration coefficients and the spectral acceleration coefficients

obtained from U.S. Geological Survey (USGS) with reference to AASHTO-2009. The data used for determining design spectrum is summarized in Table 4.3.

Table 4.3. Design spectrum parameters for Bridge-A site

Location	Ripon, CA, USA (37.75 N -121.14 W)
Site Class	D (Stiff soil)
Reference document	AASHTO-2009
Design peak ground acceleration (As, in g)	0.343
Design 0.2-second spectral acceleration (SDS, in g)	0.839
Design 1-second spectral acceleration (SD1, in g)	0.456
Seismic Design Category (SDC)	C

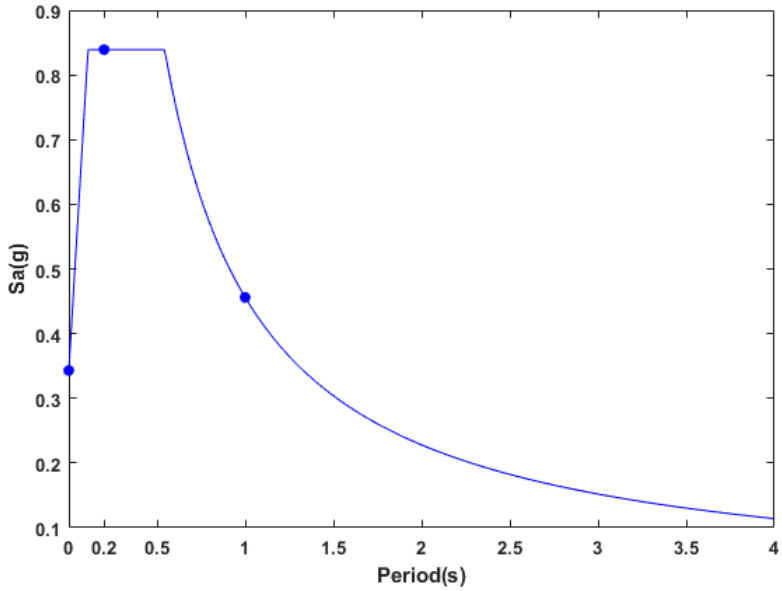

Figure 4.4. Design spectrum for Bridge-A site

4.4.2. Ground Motion

The 1994 Northridge earthquake was considered for the dynamic analysis of the bridges. The earthquake had a magnitude of 6.7 with peak ground acceleration (PGA) 0.52g. The horizontal components recorded at Beverly Hills – Mulholland drive station were used. These components are identified as NORTHR/MUL009 and NORTHR/MUL279 in Pacific Earthquake Engineering Research Center (PEER) ground motion database.

Earthquakes with return periods of 1000 years (design earthquake per AASHTO-2012) and 2500 years are considered as the two hazard levels in the time history analysis. The earthquake hazard of 1000-year return period is herein termed as Design Earthquake (DE) and the earthquake hazard of 2500 return period is termed as Maximum Considered Earthquake (MCE). Figure 4.5 show the time histories of the ground motion components. The component MUL009 was applied in the longitudinal direction of the bridge which is the direction of traffic flow and the component MUL279 was applied in the lateral direction, perpendicular to the direction of traffic flow.

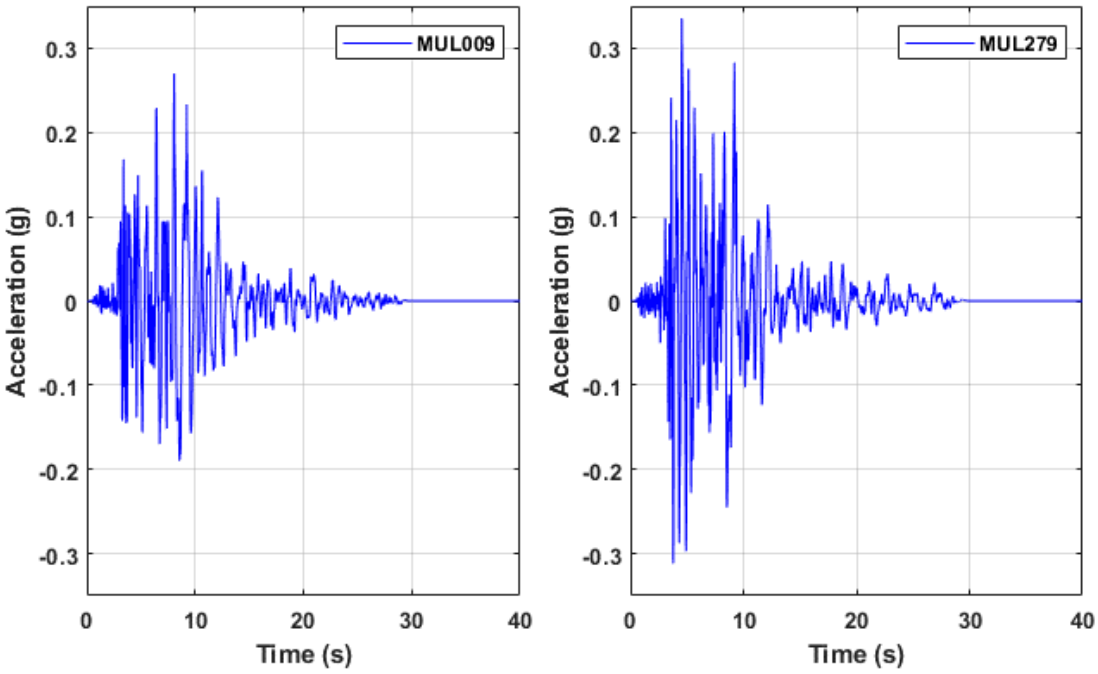

Figure 4.5. Time histories of the ground motion components

The response spectra of the ground motion components are shown in Figure 4.6. The geometric mean of the both the components was used in scaling the ground motion. The first and second mode shapes, dominant in longitudinal and lateral translation of the bridge were considered by using the geometric mean of the first two time periods to identify the corresponding spectral acceleration in the response spectrum and using it for scaling to the design spectrum (Baker & Cornell, 2006). A single scale factor was considered for all the models with different skew angles by using the geometric mean of their time periods; 0.48 seconds for monolithic bridge models and 0.5 seconds for HSR bridge models.

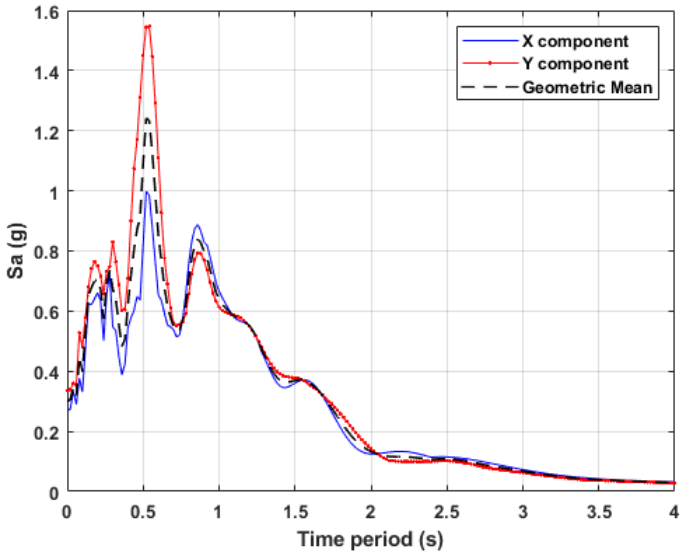

Figure 4.6. Response spectra of the ground motion components

4.4.3. General Trend Observations

A total of 20 analyses were performed, where each type of bridge with a unique abutment skew angle (0º, 15º, 30º, 45º and 60º) was analyzed for two hazard levels. The following plots show the general trends observed in the analyses that help in identifying the difference in responses of monolithic and HSR column bridges at DE and MCE hazard level.

4.4.3.1. Response of Monolithic and HSR Bridge with 30º Abutment Skew Angle

This section compares the general recorded response of monolithic and HSR column bridges at a single abutment skew angle of 30º for both hazard levels. Figure 4.7 through Figure 4.11 show the time histories of column deflection and base shear recorded of both the bridges for DE and MCE hazard level.

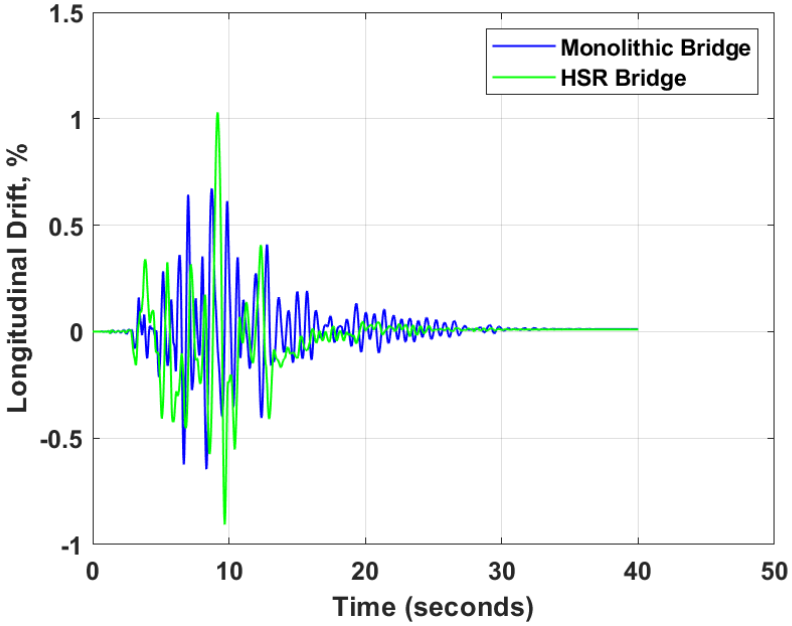

(a)

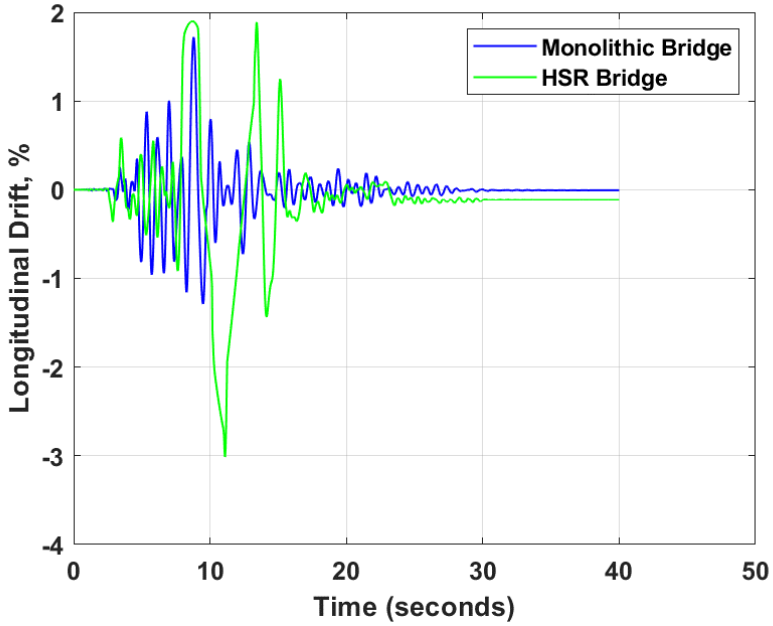

(b)

Figure 4.7. Time histories of the column deflection in longitudinal direction the bridge with 30^{o} abutment skew angle (a) DE hazard level; (b) MCE hazard level

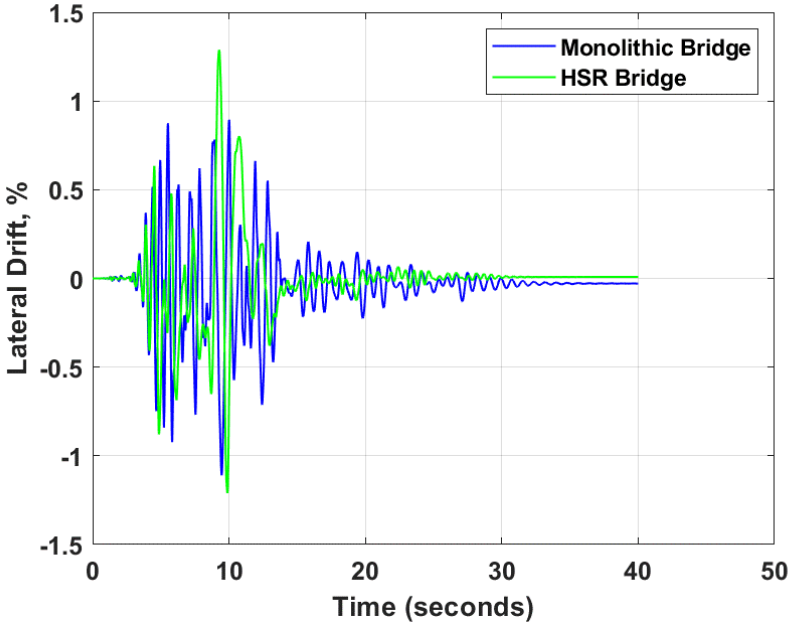

(a)

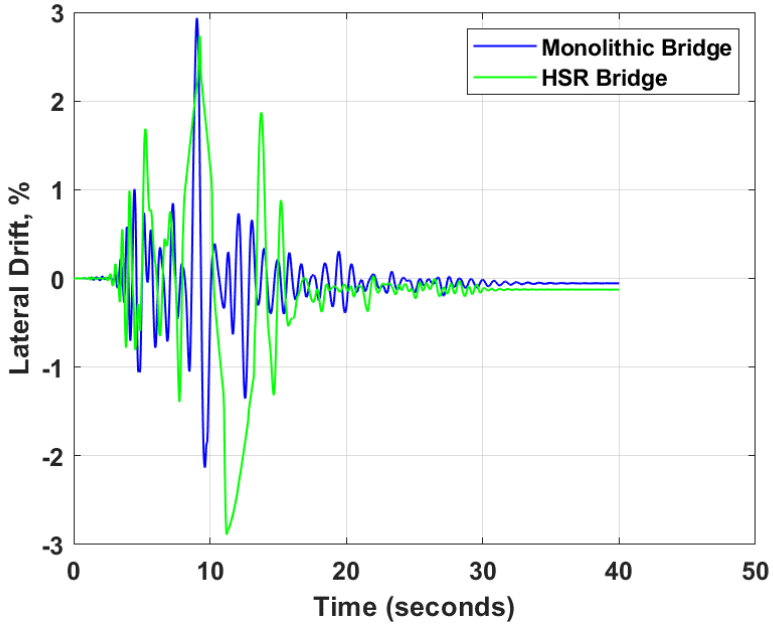

(b)

Figure 4.8. Time histories of the column deflection in lateral direction of the bridge with 30^{o} abutment skew angle (a) DE hazard level; (b) MCE hazard level

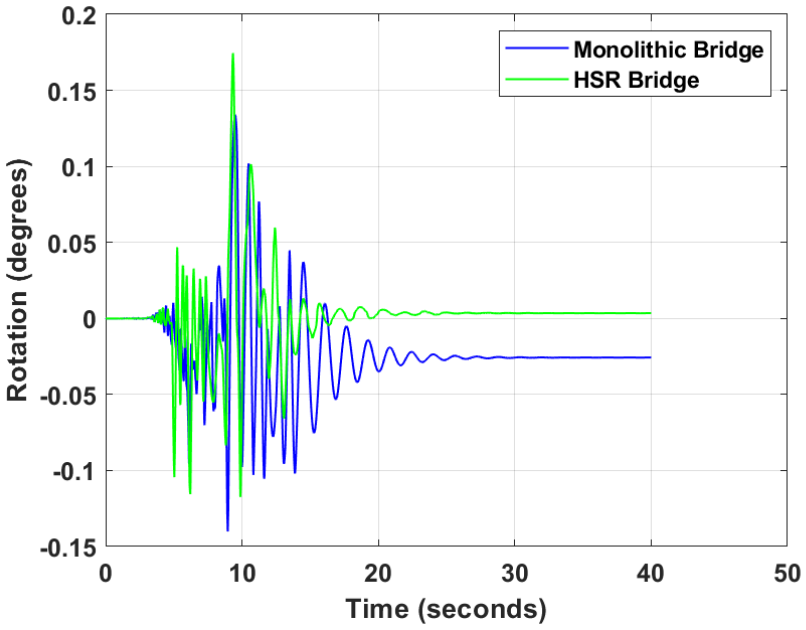

(a)

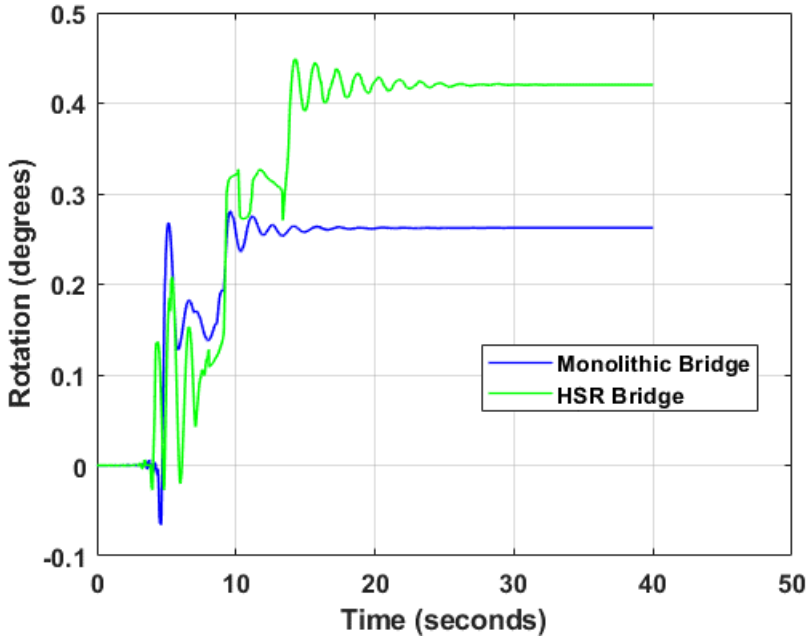

(b)

Figure 4.9. Time histories of the column rotation of bridge with 30° abutment skew angle (a) DE hazard level; (b) MCE hazard level

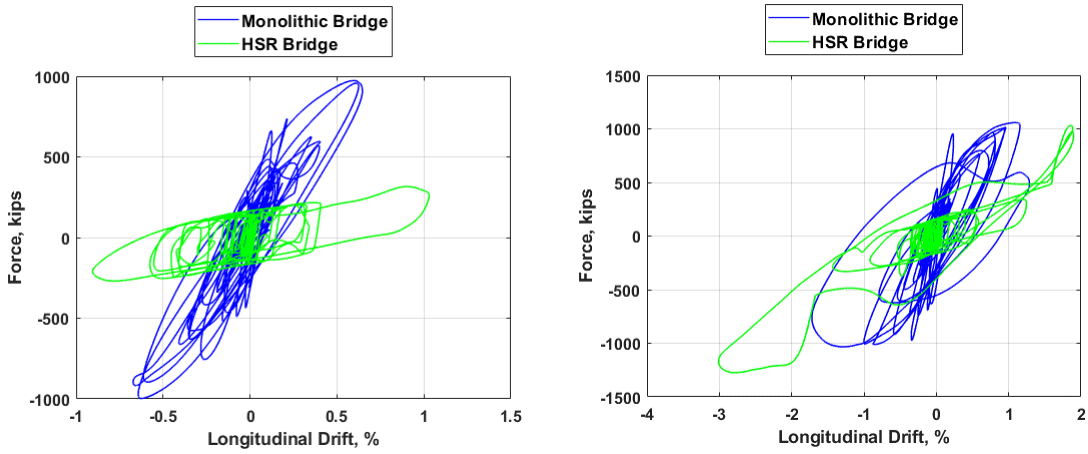

(a) (b)

Figure 4.10. Plots of base shear vs. column drift in longitudinal direction of bridge with 30° abutment skew angle (a) DE hazard level; (b) MCE hazard level

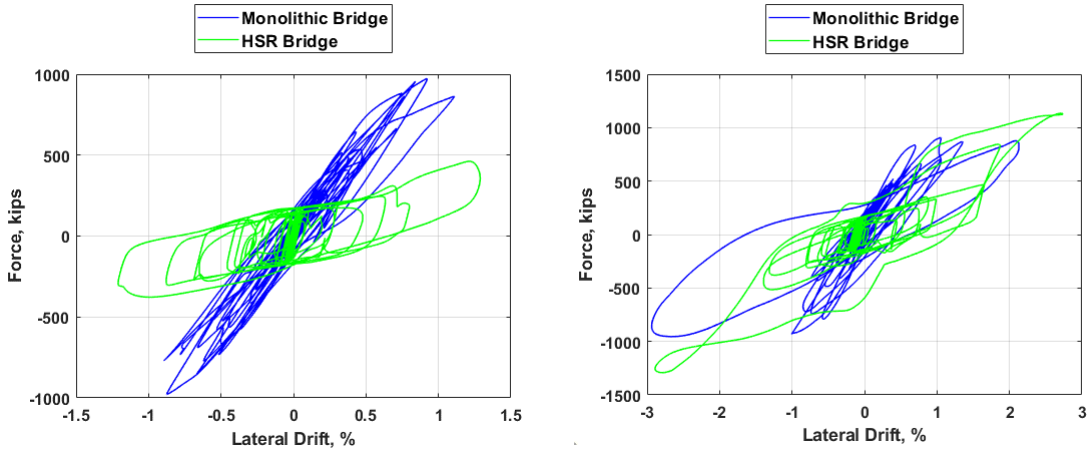

(a) (b)

Figure 4.11. Plots of base shear vs. column drift in lateral direction of bridge with 30° abutment skew angle (a) DE hazard level; (b) MCE hazard level

It can be observed from the above figures that the displacement demands of HSR column bridges are higher than monolithic column bridges due to the sliding at individual HSR joints. However, the base shear recorded is comparatively lower for HSR bridges at DE hazard level as most of the seismic energy dissipation is facilitated by the sliding of

HSR joints. Thus, the HSR column seems to impose lower demands for the design of the foundations.

4.4.3.2. Response of Monolithic and HSR Bridge with Varying Abutment Skew Angles

This section compares the base shear vs. column drift response of monolithic and HSR bridge separately with varying abutment skew angles of 0º, 15º and 30º for both hazard levels. Figure 4.12 and Figure 4.13 show the plots of base shear vs. column drift in both longitudinal and lateral directions of monolithic and HSR bridge, respectively, at DE hazard level, while Figure 4.14 and Figure 4.15 show the plots in monolithic and HSR bridge respectively at MCE hazard level. An increase in shear demand with increase in abutment skew angle is observed in the plots corresponding to DE hazard level for both monolithic and HSR bridges. However, the response of base shear vs. column drift is nearly similar with varying abutment skew angle for MCE hazard level for both bridges.

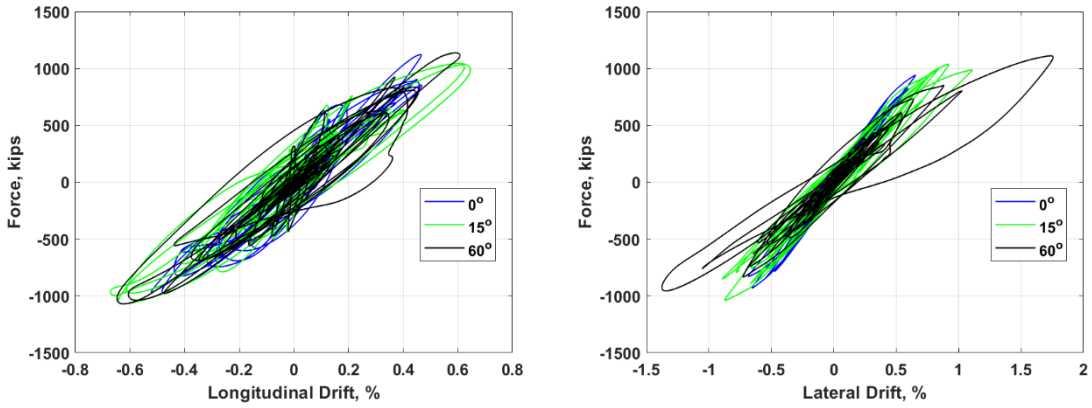

(a) (b)

Figure 4.12. Plot of base shear vs. column drift of monolithic column bridge for DE hazard level (a) longitudinal direction; (b) lateral direction

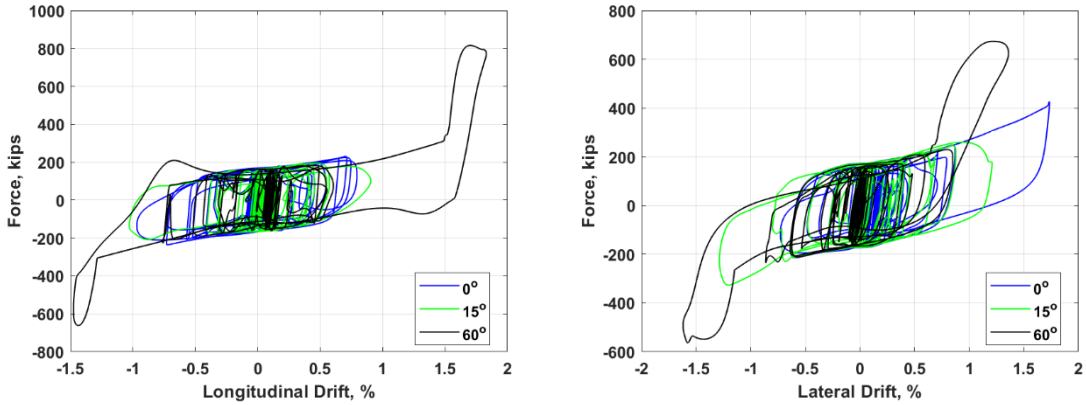

(a) (b)

Figure 4.13. Plot of base shear vs. column drift of HSR column bridge for DE hazard level (a) longitudinal direction; (b) lateral direction

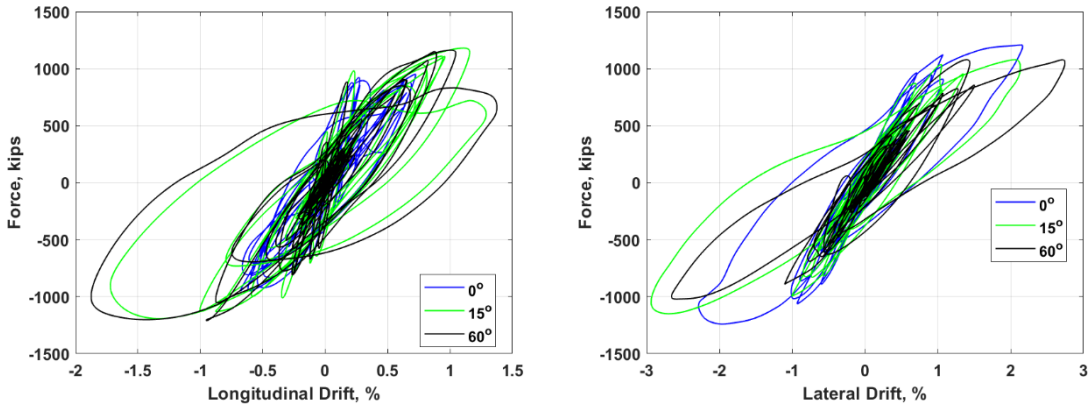

(a) (b)

Figure 4.14. Plot of base shear vs. column drift of monolithic column bridge for MCE hazard level (a) longitudinal direction; (b) lateral direction

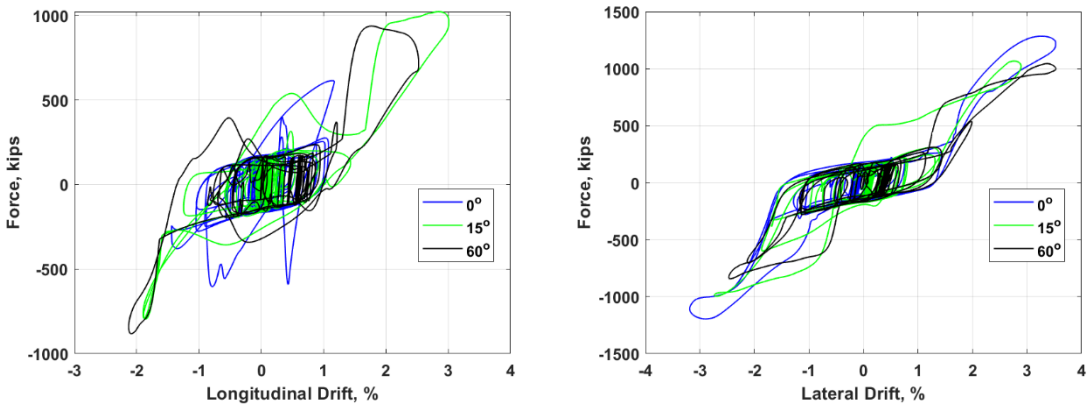

(a) (b)

Figure 4.15. Plot of base shear vs. column drift of HSR column bridge for MCE hazard level (a) longitudinal direction; (b) lateral direction

4.4.3.3. Trends in Deck Rotation

Deck rotation is influenced by the strength of shear keys and the rotation of HSR joints in case of HSR column bridges. An increase in deck rotation is observed with an increase in abutment skew angle for monolithic column bridge for both hazard levels (Figure 4.16). A similar trend is not observed in the case of HSR column bridge and the HSR bridge with an abutment skew of 30° has the maximum deck rotation among all the analyses. At large abutment skew of 60° the deck rotation is lower than that of the monolithic column bridge.

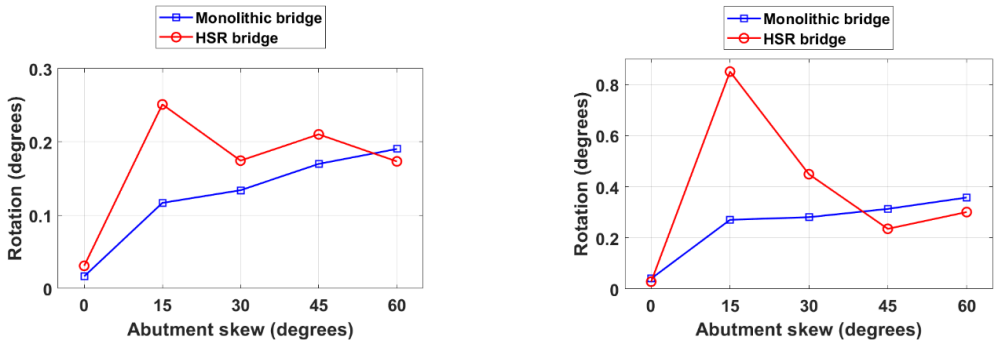

(a) (b)

Figure 4.16. Maximum deck rotation (a) DE hazard level; (b) MCE hazard level

4.5. Performance Evaluation and Comparison of Monolithic and HSR Bridges

4.5.1. Global Collapse Criteria

The collapse criteria considered in this study are column-bent peak drift ratio of 8% and deck displacement relative to the abutment in the longitudinal unseating direction greater than the seat length which is 29.5 in. as defined in PEER Report 2014/01 (Kaviani et al., 2014). The column's maximum residual drift is also checked with an allowable drift limit of 1% (JRA, 1996).

4.5.1.1. Column Drift

Both peak and residual column drift are extracted by post processing the analysis results of both monolithic an HSR column bridges for DE and MCE hazard levels with varying abutment skew angles. Figure 4.17 through Figure 4.20 show the peak and residual column drift in longitudinal and lateral direction of the bridges with respect to abutment skew angle. A stable trend in column drift cannot be established with increasing abutment skew angle from the plots, however a potential increase in column drift demand is observed for skew angles other than zero degrees.

The peak column drift observed in all the analyses is less than 4%, while the maximum residual drift observed is less than 0.6%. In case of HSR bridge, the column drift excluding sliding is also plotted as the sliding in an HSR column is recoverable using mechanical devices. Though the HSR bridge columns have a higher drift compared to monolithic column for a given hazard level, the drift excluding sliding is always lower than that of the monolithic column. The residual drifts of HSR columns are always lower

than the residual drifts of monolithic column and are nearly equal to zero for both hazard levels.

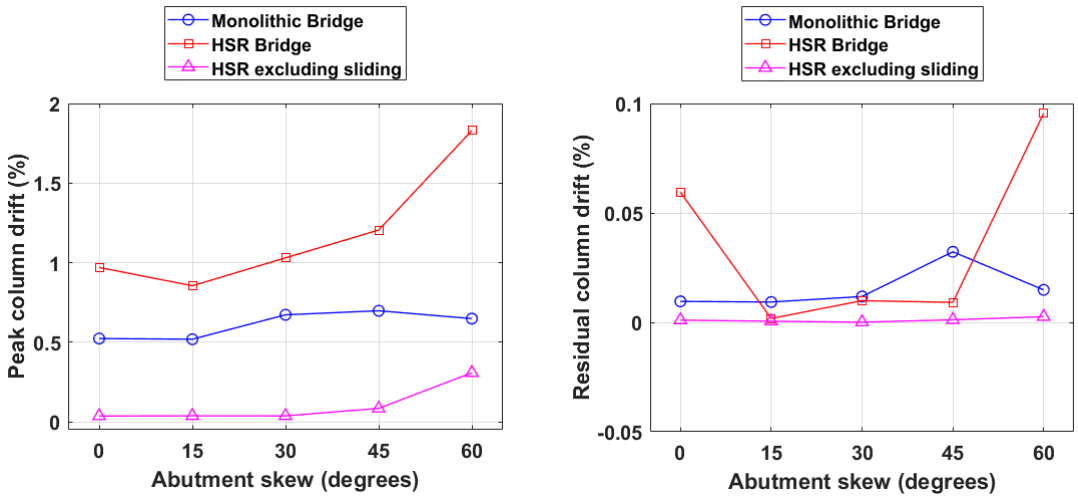

(a) (b)

Figure 4.17. Plot of column drift vs. abutment skew angle in longitudinal direction for DE hazard level (a) Maximum drift (b) Residual drift

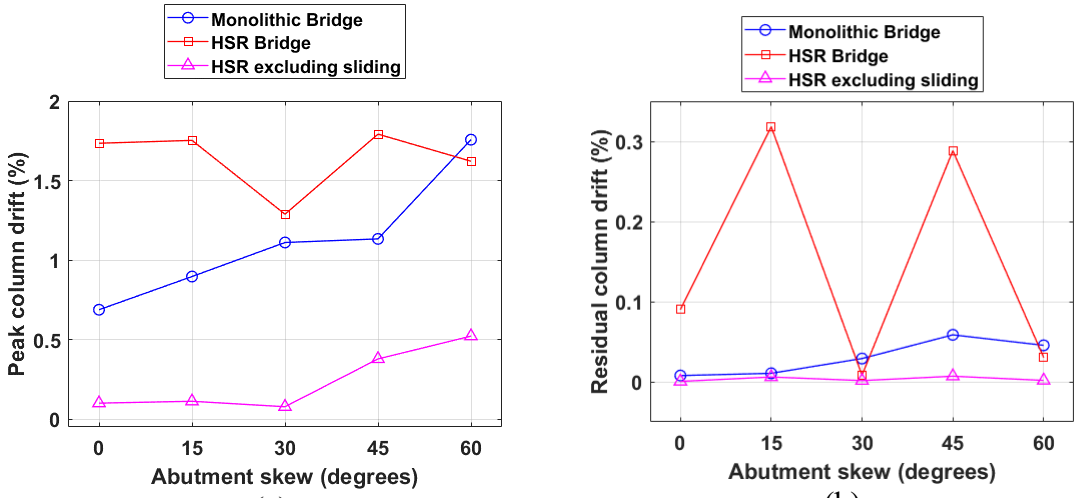

(a) (b)

Figure 4.18. Plot of column drift vs. abutment skew angle in lateral direction for DE hazard level (a) Maximum drift (b) Residual drift

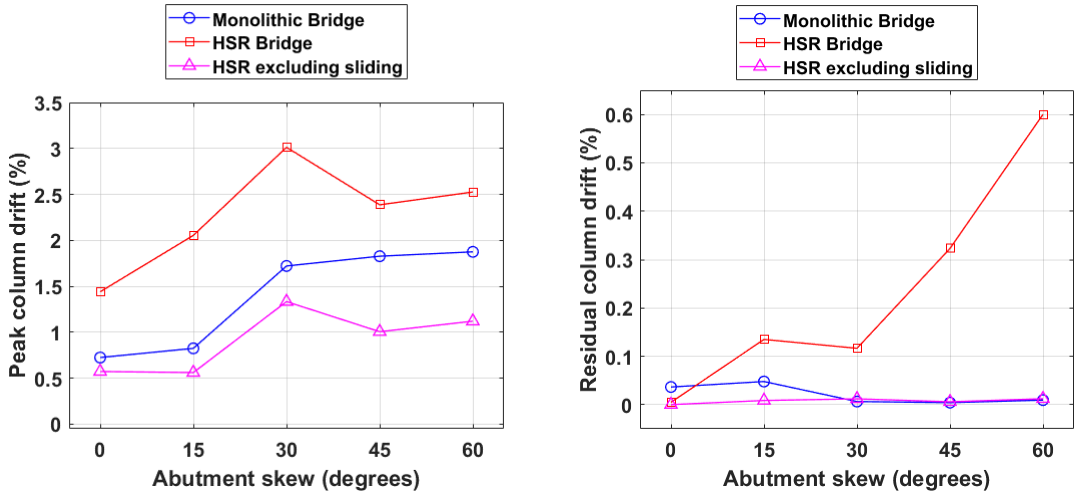

(a) (b)

Figure 4.19. Plot of column drift vs. abutment skew angle in longitudinal direction for MCE hazard level (a) Maximum drift (b) Residual drift

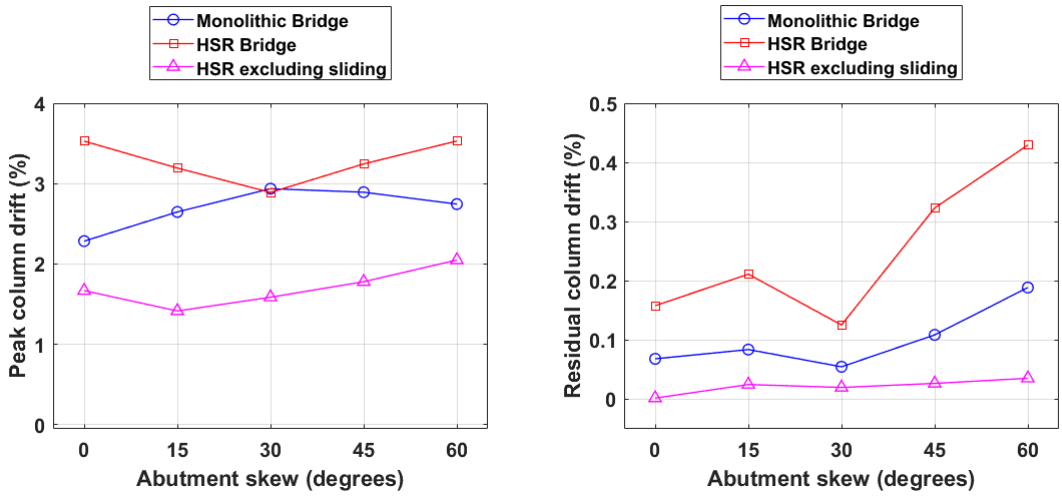

(a) (b)

Figure 4.20. Plot of column drift vs. abutment skew angle in lateral direction for MCE hazard level (a) Maximum drift (b) Residual drift

4.5.1.2. Deck Unseating

The comparison of maximum deck-end displacements with varying abutment skew angles is of both monolithic and HSR column bridges for two hazard levels are shown in Figure 4.21 and Figure 4.22 respectively. The maximum allowable displacement is 29.5 in. to avoid deck unseating and the maximum deck-end displacement observed in all the analyses on monolithic column bridge is 5 in. while the maximum displacement observed in HSR column bridge analyses is 8 in. Both the values are observed for MCE hazard level. The deck-end displacements are larger for HSR column bridge than the monolithic column bridge which is due to the sliding at HSR joints. However, the maximum displacements are well within the allowable displacement of 29.5 in. A linear increasing trend of deck-end displacement is not observed with increasing abutment skew angle; however, the displacements are large for angles greater than 15°.

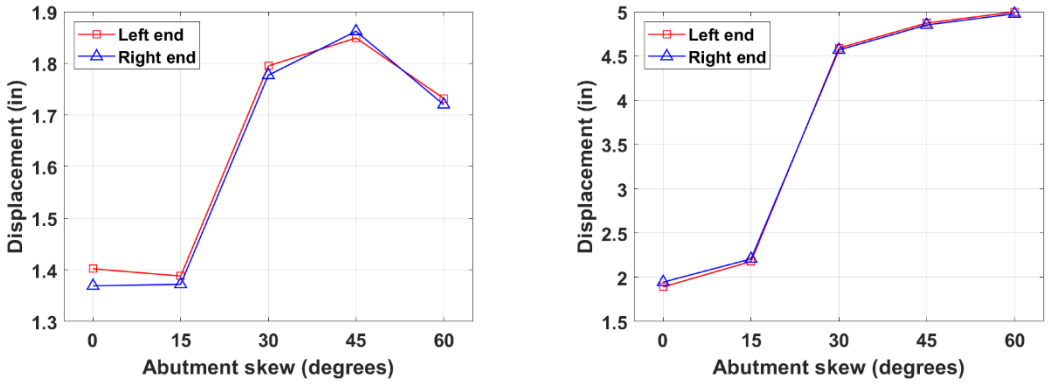

(a) (b)

Figure 4.21. Deck end displacements of monolithic column bridge (a) DE hazard level (b) MCE hazard level

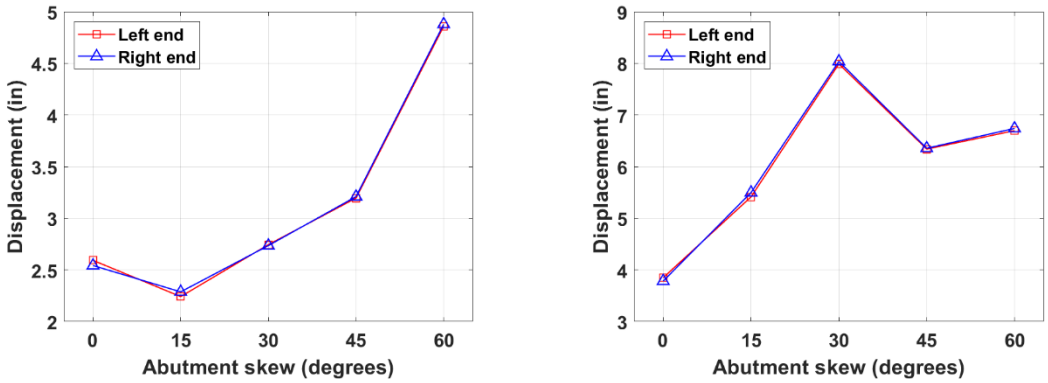

(a) (b)

Figure 4.22. Deck end displacements of HSR column bridge (a) DE hazard level (b) MCE hazard level

The yield and ultimate displacement of bearings were assumed to be 150% and 300% of the shear strain (Aviram et al., 2008). The modeled elastomeric bearings have a yield and ultimate sliding capacity of 3.75 in. and 7.5 in. respectively, beyond which the bearings are assumed failed. This affects the serviceability of the bridge structure as there is a need for repair or replacement of the bridge bearings. The ultimate capacity of bearing has exceeded only in the case of HSR column bridge with 30° abutment skew at MCE hazard level (Figure 4.22).

4.5.2. Shear Keys

Shear keys prevent the damage to abutments due to deck displacements in the event of a seismic motion and any damage to the shear keys affects the serviceability of the bridge. The maximum allowable deformation of shear keys is given as 2.45 in., beyond which the shear key is determined as failed. Figure 4.23 through Figure 4.26 show the deformation of all four shear keys of both the bridges with varying abutment skew angle. A horizontal line depicting the failure deformation is shown in the figures to check the

status of the shear key. It can be observed from Figure 4.23 and Figure 4.24, that the deformation of shear keys increases with increase in abutment skew angle in monolithic column bridge, which is not the case in HSR column bridge. All the shear keys of both monolithic column bridge and HSR column bridge have failed for MCE hazard level, with the later having large deformations compared to the monolithic column bridge's shear keys. Large number of shear key failures are observed in the analyses of HSR column bridge, which is due to the larger rotation of HSR bridge deck than the monolithic bridge deck.

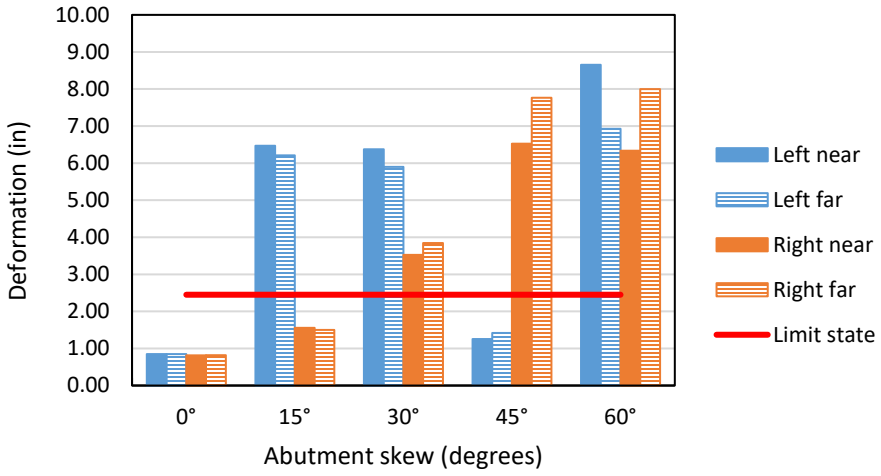

Figure 4.23. Status of shear keys of monolithic column bridge for DE hazard level

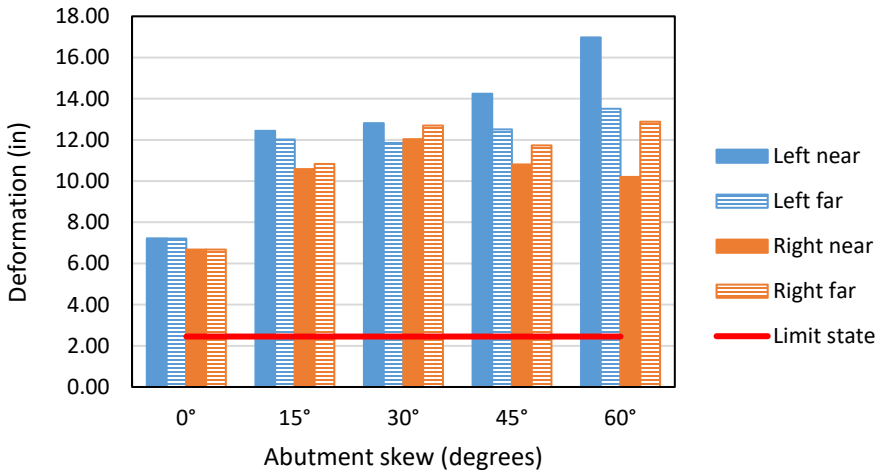

Figure 4.24. Status of shear keys of monolithic column bridge for MCE hazard level

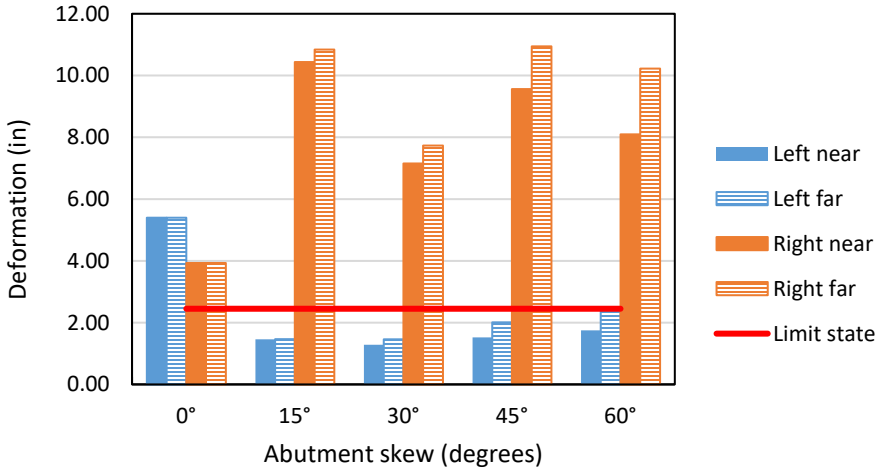

Figure 4.25. Status of shear keys of HSR column bridge for DE hazard level

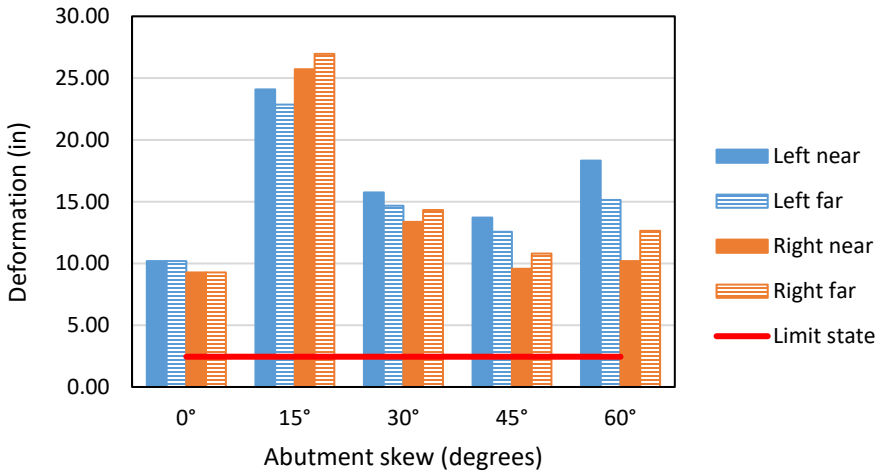

Figure 4.26. Status of shear keys of HSR column bridge for MCE hazard level

4.5.3. Column

The bottommost section deformations of both monolithic and HSR columns were recorded for all the analyses and the results are post-processed to calculate the maximum strains in cover concrete, core concrete and longitudinal mild steel reinforcement. Tendons strain is also recorded in HSR column to check their damage state. The maximum of each type of strain recorded at eight different locations as shown in Figure 4.27 and Figure 4.28 is used to check the damage state with its corresponding limit state as shown in Table 4.4. The following sections describe the damage state of individual material in detail.

Table 4.4. Limit state strains of column materials

Damage	Monolithic column	HSR column
Cover concrete spalling	0.005	0.005
Core concrete crushing	0.031	0.033
Longitudinal steel yielding	0.0023	0.0023*
Tendon yielding	n/a	0.0085

* The bottommost section of HSR column is a compression only fiber section with no steel

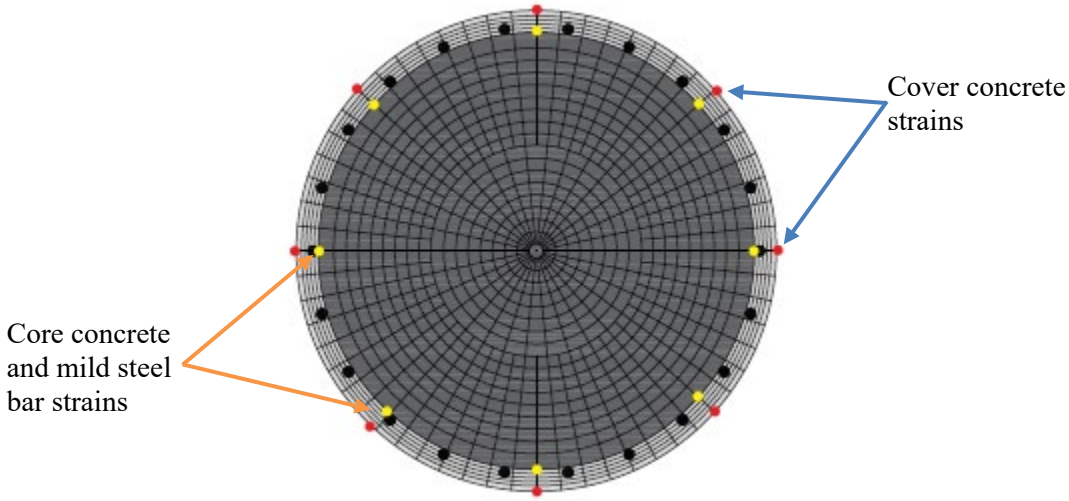

Figure 4.27. Bottommost cross-section of monolithic column shown strain recording locations

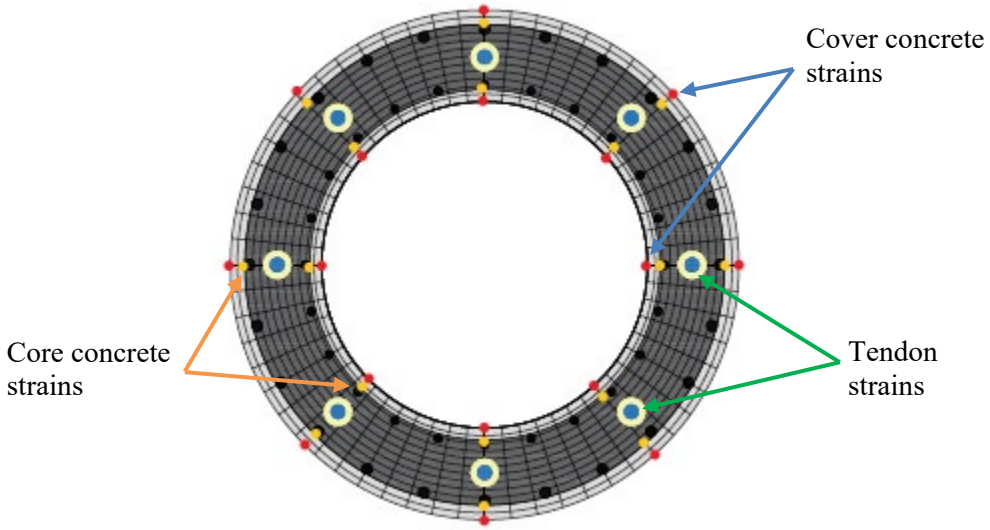

Figure 4.28. Bottommost section of HSR column showing strain recording locations

4.5.3.1. Cover Concrete

Spalling of cover concrete is not observed in HSR column for all abutment skew angles at DE hazard level as shown in Figure 4.29. However, at MCE hazard level spalling is observed in both monolithic and HSR columns (Figure 4.30).

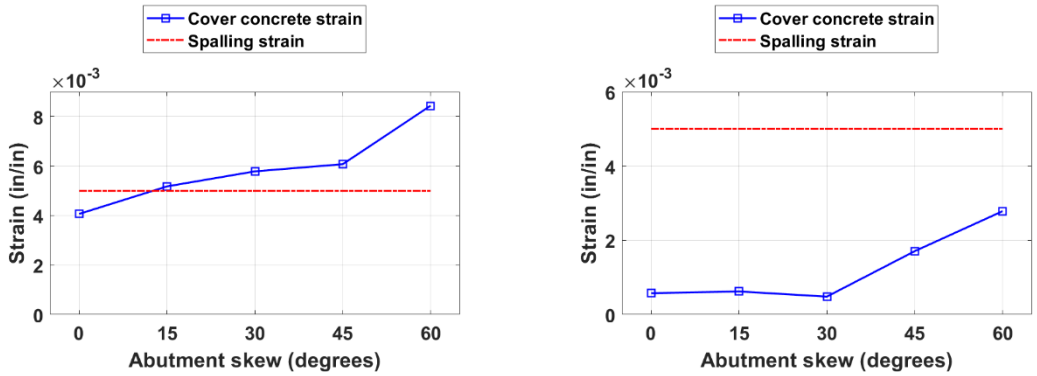

(a) (b)

Figure 4.29. Cover concrete strains at DE hazard level (a) monolithic column bridge; (b) HSR column bridge

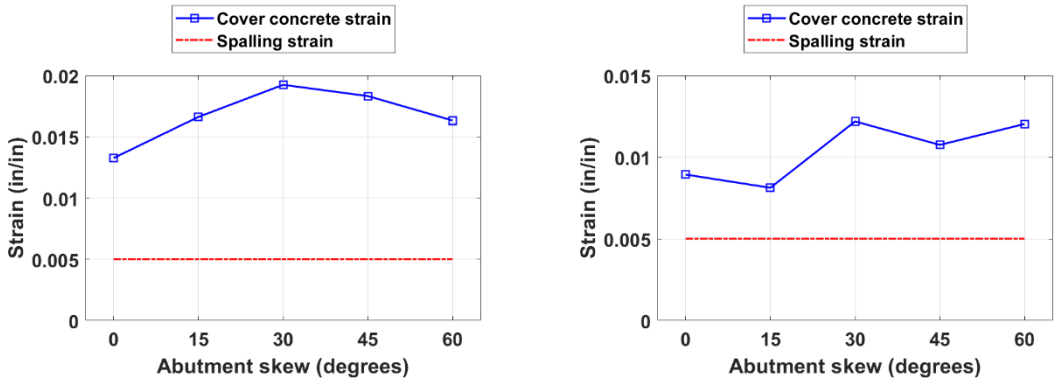

(a) (b)

Figure 4.30. Cover concrete strains at MCE hazard level (a) monolithic column bridge; (b) HSR column bridge

4.5.3.2. Core Concrete

Core concrete crushing was not observed in either monolithic column or HSR column at both DE and MCE hazard levels as shown in Figure 4.31 and Figure 4.32. It can also be inferred from the figures that; the core concrete strain is approximately three times lower than the crushing limit state in both monolithic and HSR columns.

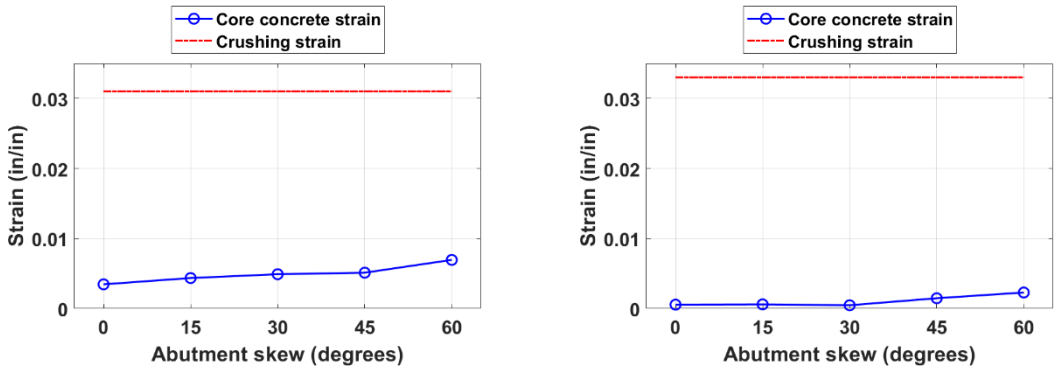

Figure 4.31. Core concrete strains at DE hazard level (a) monolithic column bridge; (b) HSR column bridge

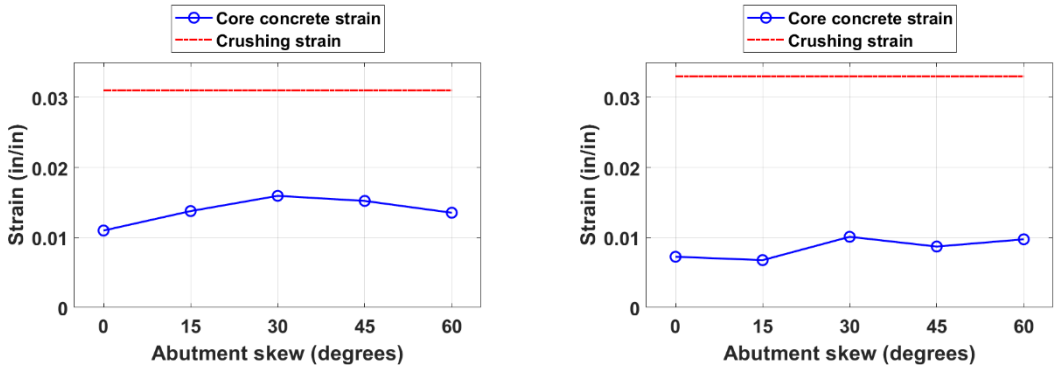

Figure 4.32. Core concrete strains at MCE hazard level (a) monolithic column bridge; (b) HSR column bridge

4.5.3.3. Longitudinal Mild Steel in Monolithic Column

Yielding in longitudinal steel bars is observed in the monolithic column for all abutment skew angles for both hazard levels as shown in Figure 4.33. From Figure 4.33(a) it can also be observed that the maximum strain in steel bars increases with increase in abutment skew angle, where the strain recorded at 60° abutment skew is more than two strains the strain observed at 0° abutment skew.

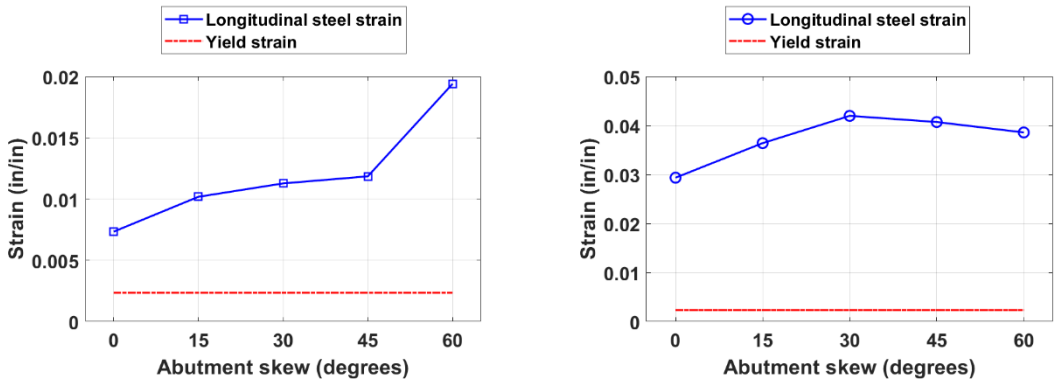

Figure 4.33. Longitudinal steel bar strains in monolithic column (a) DE hazard level; (b) MCE hazard level

4.5.3.4. Tendons in HSR Column

The status of tendons is considered critical as any damage to the tendon leads to a loss in prestressing force and demands for repair or replacement of the tendon. The maximum strain recorded from all the eight tendons is used to check the damage state of the tendons at each abutment skew angle for both hazard levels. It can be observed from Figure 4.34 that none of the tendons have yielded even at MCE hazard level and large abutment skew angles.

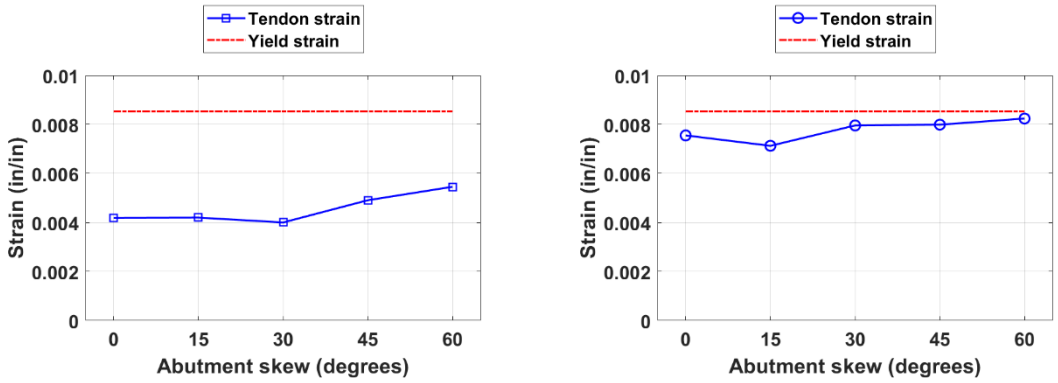

Figure 4.34. Tendons strains in HSR column (a) DE hazard level; (b) MCE hazard level

5. TESTING OF HSR INTERFACE DESIGNS

5.1. Introduction

This chapter presents the experimental study conducted to investigate the frictional properties and bond strength of the PTFE-on-PTFE interface to be used in the design of HSR columns. Normal force and sliding velocity were varied and the variation of frictional response was recorded for both dry and lubricated interfaces. Results are used to develop a numerical model that can be used in the HSR joint modeling. The testing program was performed in the Structural and Materials Testing Lab at the Center for Infrastructure Renewal (CIR) facility of the Texas A&M University.

5.2. Test Setup

5.2.1. Specimen Description and Preparation

The test specimen consists of PTFE bonded to thin steel plate which was subsequently bonded to concrete. Both the steel plate and PTFE sheet are 1/8 in. thick. The PTFE sheet was filled with 25 % glass fiber by weight, which increases the wear resistance compared to unfilled PTFE. Commercially available two-component epoxy adhesive cement was used for bonding both steel-PTFE and concrete-steel. A minimum tensile shear strength of 3100 psi was specified for the epoxy at an operating temperature of 25ºC. For lubrication, commercially available Super Lube synthetic grease with syncolon (PTFE) with both NLGI (National Lubricating Grease Institute) grades 1 and 2 were used. The NLGI number is a measure of relative hardness of the grease.

Concrete prisms of two different sizes were used to form a testing setup, where the smaller concrete prism was held between two identical longer prisms by a normal force as shown in Figure 5.1. The longer prisms had dimensions of 6”x2.5”x2”, while the central sliding prism had dimensions 4”x2.5”x2” to ensure full contact of the sliding surface at all times for maintaining a constant normal pressure. The dimensions of contact surfaces are 6”x2” for longer prisms and 4”x2” for the intermediate sliding prism, which leaves an effective contact area of 8 in^2 at all the times during testing.

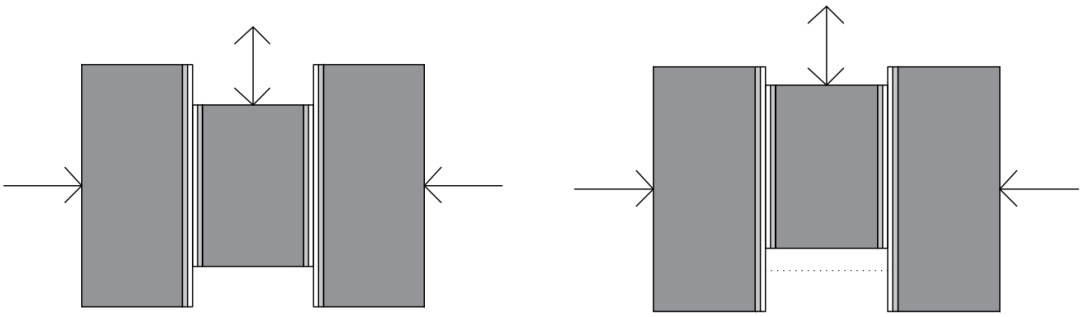

(a) (b)

Figure 5.1. Concept of the test: (a) initial state; (b) sliding state

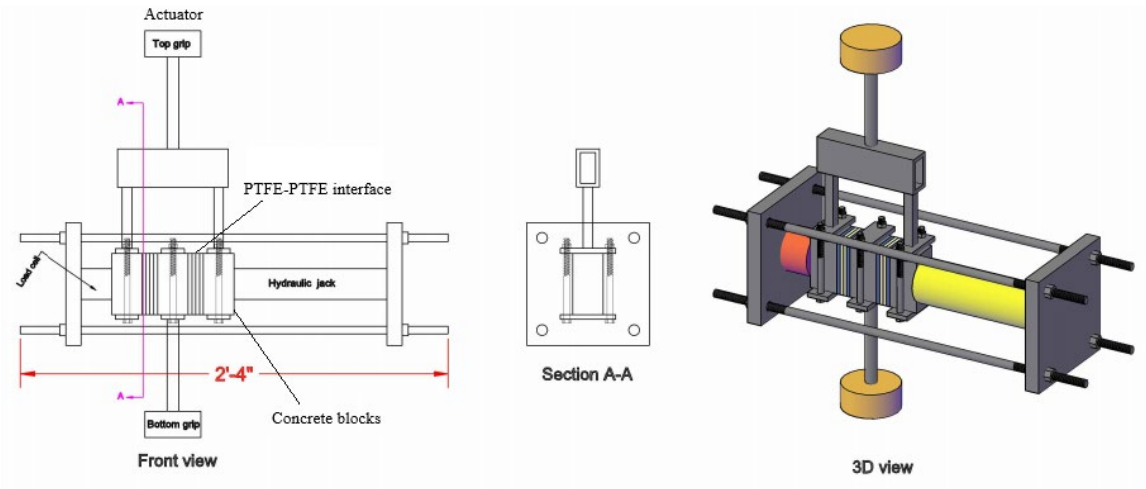

Figure 5.2. Overview of test setup

Wooden molds were prepared and readily mixable concrete with strength 5 ksi and maximum size of aggregate 0.75 in. was used to prepare the specimens (Figure 5.3). They were cured at 20°C and 85% relative humidity for more than 28 days and later cut using a concrete saw to get rid of any irregularities and maintain smooth and perpendicular surfaces.

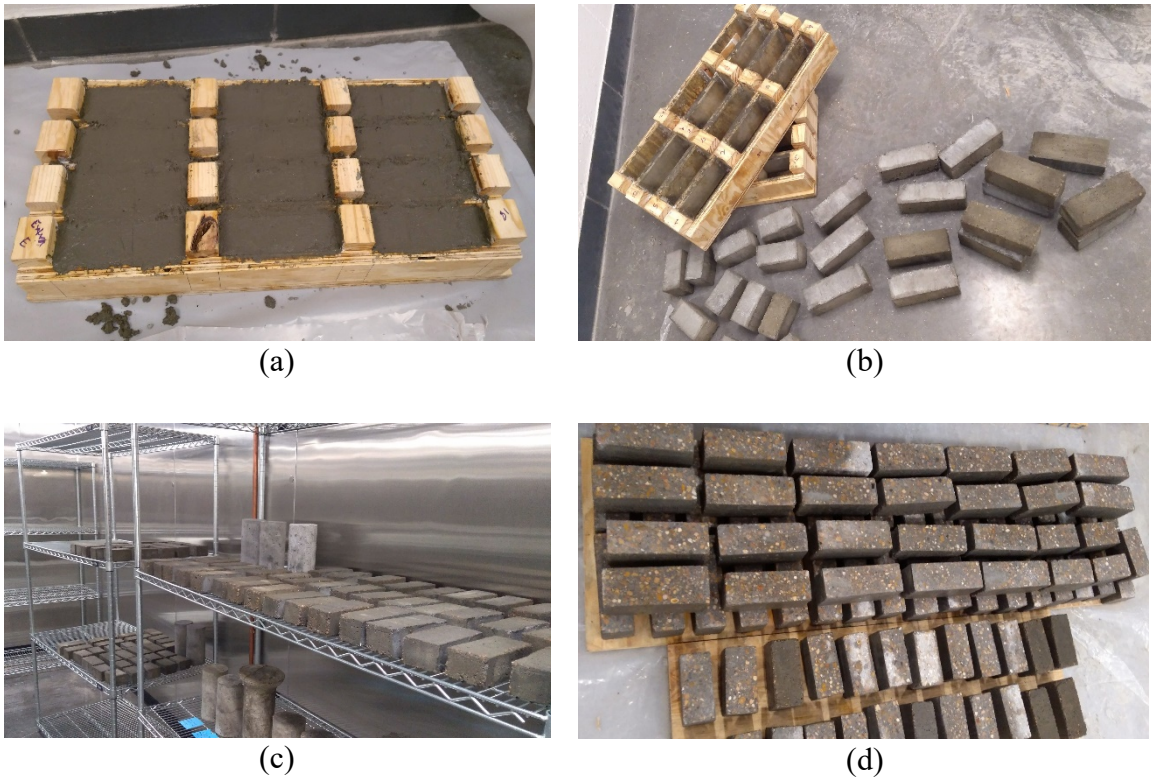

(a) (b)

(c) (d)

Figure 5.3. Concrete prisms preparation: (a) concrete pouring; (b) removal of formwork; (c) curing; (d) concrete specimen after cutting

Before bonding, the rough surfaces and dust on concrete were cleaned. Steel plates were ground using a sand paper and cleaned with acetone to remove dirt and grease. The etched surface of PTFE was also cleaned with acetone (Figure 5.4). The epoxy was

applied uniformly on the concrete surface as a thin layer and the steel sheet was placed. Similar procedure was followed to glue the PTFE to the steel. The whole specimen was left undisturbed overnight, for curing, after applying pressure using clamps.

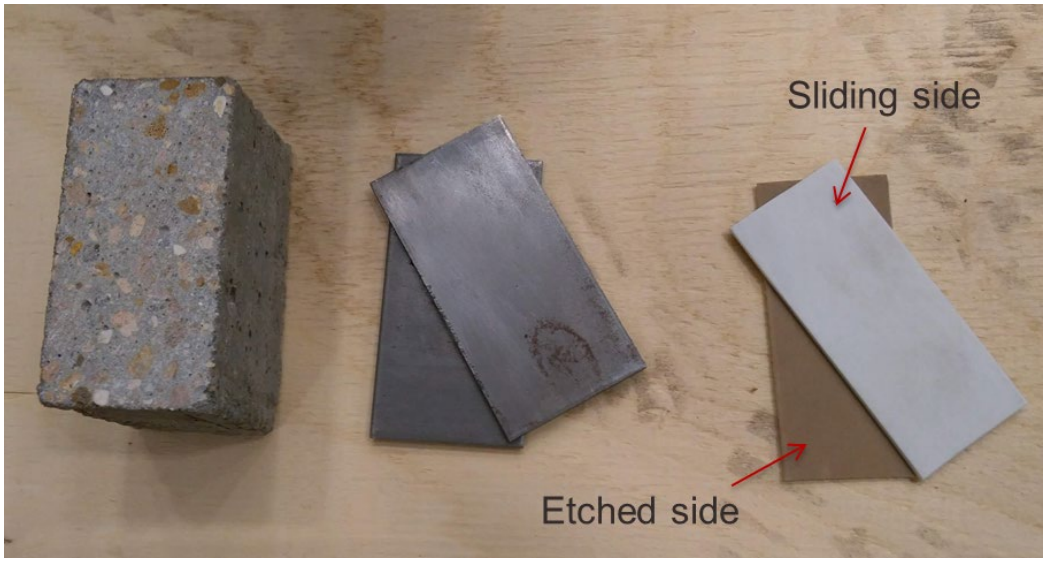

Figure 5.4. Specimen surface preparation

5.2.2. Experimental Setup and Instrumentation

The experimental setup was designed to hold the specimen and facilitate the sliding of the central piece. The top part was designed to hold the two longer prisms while the bottom part holding the sliding piece (Figure 5.2). Both parts were held at the respective top and bottom grips of the MTS hydraulic dynamic and static fatigue-rated 55-kip capacity uniaxial testing machine of 6" stroke. Normal force was applied using a hydraulic jack and four prestressing rods. The Enerpac hydraulic cylinder used had a maximum stroke length of 6-1/8" and a maximum operating pressure of 10,000 psi.

The MTS machine is equipped with a 20-kip load cell for measuring the axial force applied. A donut type load cell with a capacity of 50-kips was used to record the normal force applied on the specimen. Although the MTS machine is equipped with an internal transducer for measuring the applied stroke, two LVDTs (Linear Variable Displacement Transducer) with a stroke of +/- 1 in. were used to record the sliding displacement of the intermediate specimen, in order to avoid contamination of the measurements from the flexibility of the loading frame (Figure 5.5). All the sensor signals were recorded at a sampling rate of 512 readings per second using National Instruments-Lab View data acquisition system. This sampling rate was much larger than the loading frequencies of the applied load and the specimen response.

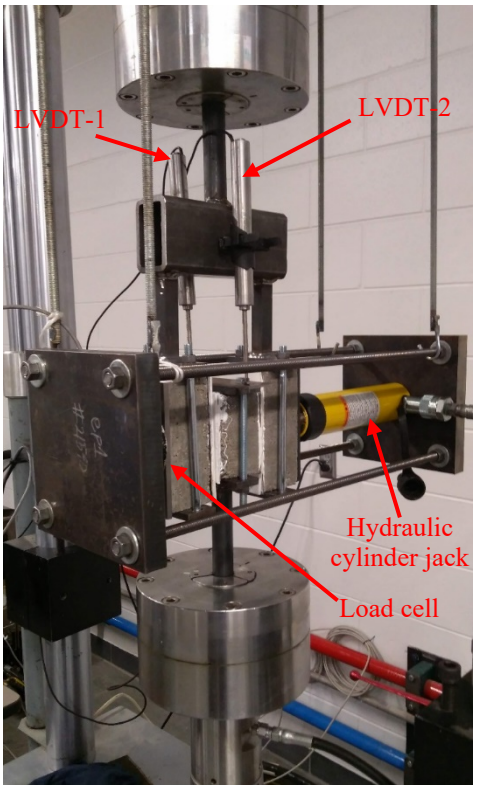

Figure 5.5. Experimental setup with instrumentation

5.3. Test Procedure

5.3.1. Specimen Configurations and Test Parameters

Four types of specimens were considered in this experimental study, Specimen types 1 and 2 considered dry friction interface with different sliding protocols for the sliding displacement and contact pressure, whereas the specimen types 3 and 4 had lubricated interfaces, one with NLGI grade 1 grease and the other with grade 2 grease. Three specimens were considered for each test or specimen type to ensure repeatability of the observed/measured properties and the average of results are reported.

The frictional response due to variation in contact pressure was investigated by applying six different contact pressures on each type of specimen. The contact pressures considered were 250, 500, 750, 1000, 1500 and 2000 psi. To investigate the frictional response due to variation in sliding velocity, four different velocities were considered ranging between 0.4 in/s and 5 in/s. A sinusoidal motion with constant sliding amplitude of 0.25 in. was used for all the tests and the sliding velocity was varied by changing the actuator frequency. The frequencies used were 0.25, 1, 2 and 3 Hz (cycles per second).

5.3.2. Sliding Protocols and Testing Program

Each specimen type was subjected to six different (constant) contact pressures with the same sliding protocol followed for each contact pressure. The sliding protocol followed is mentioned in Table 5.2. As shown in the table, each sliding protocol considered four different sliding velocities by varying the frequencies of the applied sliding displacements. The sliding was applied in three cycles for each frequency, which added to 12 cycles of sliding, each time a sliding protocol was applied to a specimen for

each contact pressure. That sums up to 72 cycles of sliding on a single type of specimen. Detailed description of the testing sequence is mentioned in Table 5.3. The MTS machine was programmed to maintain a one second gap between changing frequencies in the sliding protocol and a 10 to 15-minute wait time was considered between the test and normal load application for first two contact pressures. This procedure facilitated to record and identify the breakaway friction and dynamic friction separately.

The nomenclature considered for the specimen type in this study had five fields as mentioned in Table 5.1. The first field was 'HSR' denoting the tests performed, are part of research on Hybrid Sliding-Rocking columns, the second field distinguishes the tests based on dry (D) or lubricated (L) interfaces, the third field identifies the sliding protocol (S1/S2), the fourth field labels the sequence of applied normal pressures (P1/P2) and the fifth field identifies the specimen number (SP) as the tests were repeated on three specimens. The test with lubricated interfaces had an extra field denoting the grease type used for lubrication (G1 or G2).

Table 5.1. Testing program

Set	**Test #**	**Test Name**	**Sliding protocol**	**Pressure Protocol**	**Approximate duration of each test**
1	1	HSR_D_S1_P1_SP1	S1	P1	45 minutes
	2	HSR_D_S1_P1_SP2			
	3	HSR_D_S1_P1_SP3			
2	4	HSR_D_S2_P2_SP1	S2	P2	45 minutes
	5	HSR_D_S2_P2_SP2			
	6	HSR_D_S2_P2_SP3			

Table 5.1. Continued

3	7	HSR_L_S1_P1_SP1_G1	S1	P1	45 minutes
	8	HSR_L_S1_P1_SP2_G1			
	9	HSR_L_S1_P1_SP3_G1			
4	10	HSR_L_S1_P1_SP1_G2	S1	P1	45 minutes
	11	HSR_L_S1_P1_SP2_G2			
	12	HSR_L_S1_P1_SP3_G2			

Table 5.2. Sliding protocol for each set of tests at fixed contact pressure

No.	**ID**	**Displacement Amplitude (in)**	**Frequency (Hz)**	**No. of cycles**	**Maximum velocity (in/s)**	**Duration (seconds)**
1	S1	0.25	0.25	3	0.39	20
			1	3	1.57	
			2	3	3.14	
			3	3	4.71	
2	S2	0.25	1	3	1.57	20
			2	3	3.14	
			3	3	4.71	
			0.25	3	0.39	

Table 5.3. Pressure protocol

ID	Sequence for Pressure
P1	1. Normal force 4000 lb. (500 psi) - Wait time: 15 min → run S# → 2. Normal force 2000 lb. (250 psi) - Wait time: 10 min → run S# → 3. Normal force 6000 lb. (750 psi) - Wait time: 0 min→ run S# → 4. Normal force 8000 lb. (1000 psi) - Wait time: 0 min → run S# → 5. Normal force 12000 lb. (1500 psi) - Wait time: 0 min→ run S# → 6. Normal force 16000 lb. (2000 psi) - Wait time: 0 min→ run S# → end
P2	1. Normal force 6000 lb. (750 psi) - Wait time: 15 min → run S# → 2. Normal force 2000 lb. (250 psi) - Wait time: 10 min → run S# → 3. Normal force 8000 lb. (1000 psi) - Wait time: 0 min → run S# → 4. Normal force 4000 lb. (500 psi) - Wait time: 0 min → run S# → 5. Normal force 12000 lb. (1500 psi) - Wait time: 0 min → run S# → 6. Normal force 16000 lb. (2000 psi) - Wait time: 0 min→ run S# → end

5.4. Test Results

The sliding displacements recorded with two LVDTs were initialized first to remove any offset, filtered by a low pass filter (corner frequency-50) to remove inherent signal noise, and then averaged. The average sliding displacement was used to calculate the sliding velocity of the intermediate concrete prism. The coefficient of friction was calculated by normalizing the frictional force recorded from the actuator with the normal force recorded from the load cell. The frictional force was assumed to distribute equally between both the sliding surfaces while calculating the coefficient of friction (COF).

5.4.1. Dry Interface Tests with Pressure Protocol P1

Two different testing sequences were used in the tests on dry PTFE-on-PTFE interfaces as mentioned in Table 5.3. A typical response of the sliding displacement and sliding velocity recorded in HSR_D_S1_P1_SP1 test with fixed contact pressure of 500 psi are shown in Figure 5.6 and Figure 5.7 respectively.

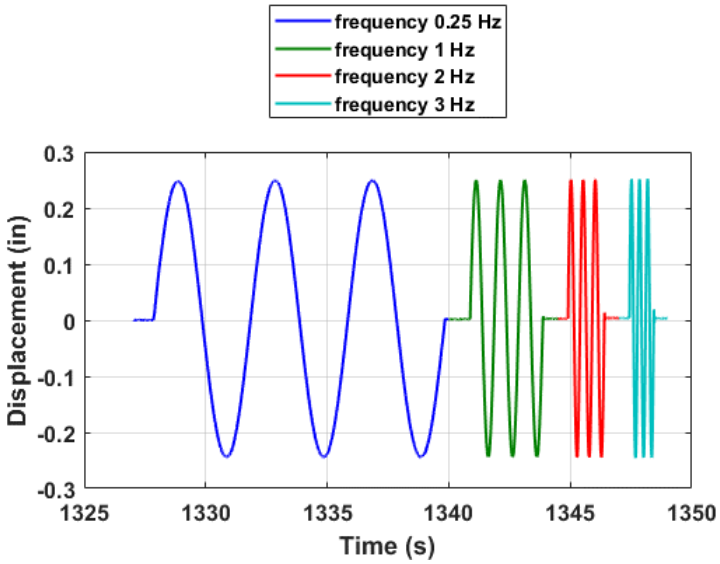

Figure 5.6. Test HSR_D_S1_P1_SP1: sliding displacement of the intermediate concrete prism

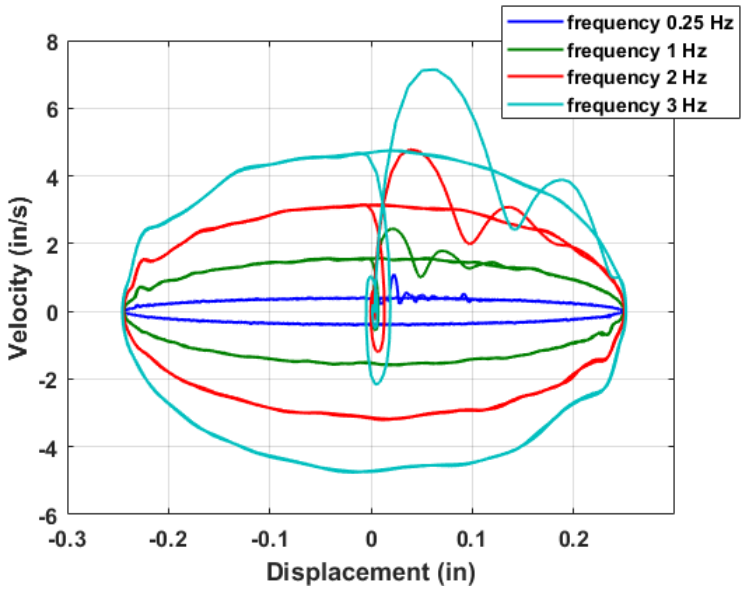

Figure 5.7. Test HSR_D_S1_P1_SP1: sliding velocity vs. sliding displacement

Figure 5.8 shows a plot of the coefficient of friction vs. sliding displacement for HSR_D_S1_P1_SP1 at the first pressure in the testing sequence which is 500 psi. The plot shows a total 12 cycles of sliding displacement applied on the specimen as shown in Figure 5.6. Both breakaway friction and kinetic (dynamic) friction can be identified from examining the figure. A slight increase in COF followed by a rapid decrease at the diagonally opposite ends of the rectangular loop is due to the sliding reversal which is defined as a stick-slip phenomena (Dolce et al., 2005) and typically referred as static friction. The figure clearly depicts the dependence of coefficient of friction on the sliding velocity, where the COF increases with increase in the frequency of sliding i.e. sliding velocity. The observed trend in not in accordance with the Coulomb's law of friction, which states that the kinetic COF of dry sliding surfaces is independent of the magnitude of sliding velocity. It can also be observed that the COF values almost coincide for

frequencies 2 and 3 Hz and a variation in COF is noticeable as the number of cycles increases at a single frequency.

Figure 5.9 shows the response of COF vs. sliding displacement of HSR_D_S1_P1_SP1 for the whole test sequence. It clearly shows the variation and dependence of COF on the normal pressure. It can be observed that the COF friction decreases with increase in normal pressure. Though the average normal pressures are mentioned in the figure, the normal pressures recorded showed up to a maximum of +/- 50 psi offset as the line of normal force deviates from the mid axis of the specimen, which also induces moments in the setup.

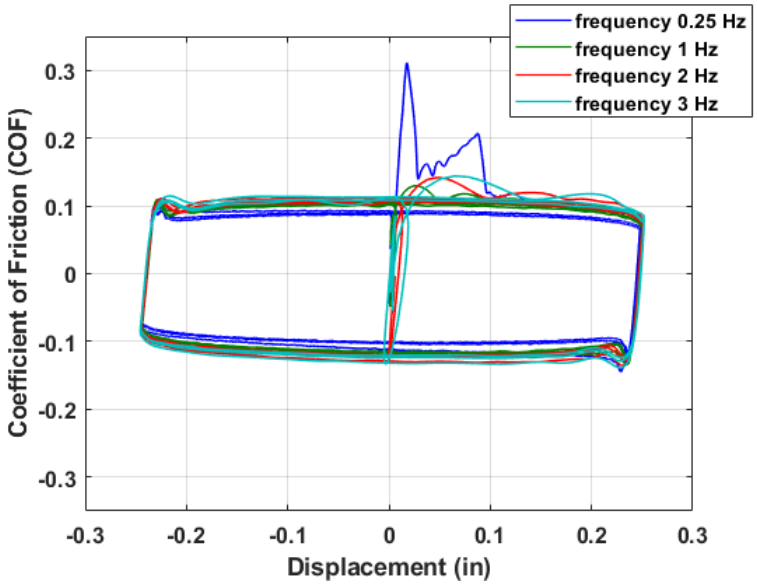

Figure 5.8. Test HSR_D_S1_P1_SP1: coefficient of friction vs. sliding displacement at contact pressure 500 psi

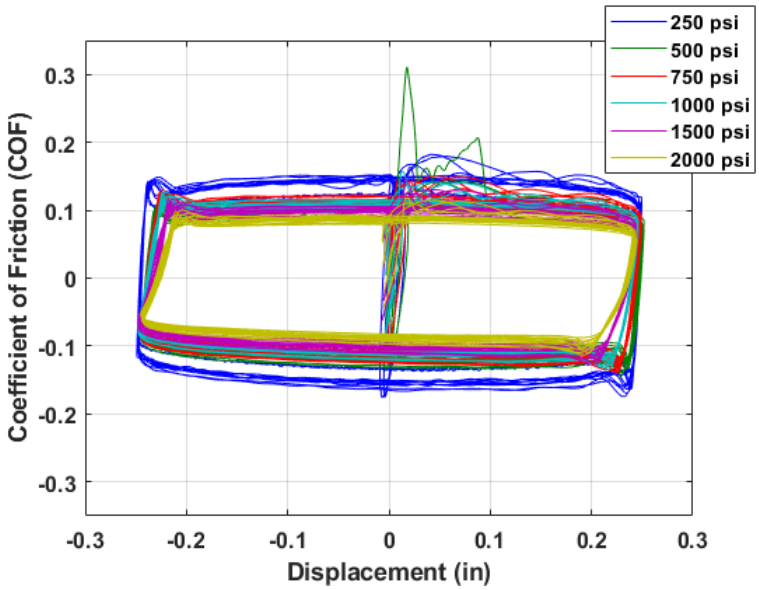

Figure 5.9. Test HSR_D_S1_P1_SP1: coefficient of friction vs. sliding displacement for all contact pressures

5.4.2. Dry Interface Tests with Pressure Protocol P2

A typical response of the sliding displacement and sliding velocity with pressure protocol P2 are shown in Figure 5.10 and Figure 5.11 respectively. Figure 5.12 shows a plot of the coefficient of friction vs. sliding displacement for HSR_D_S2_P2_SP1 at the fourth pressure in the testing sequence which is 500 psi. Comparing it with Figure 5.8, which shows the testing sequence S1-P1, it can be observed that the breakaway friction coefficient is comparatively lower in the testing sequence S2-P2 at same contact pressure of 500 psi. The difference is due to the order of normal load application, where the contact pressure, 500 psi is fourth in the sequence and the breakaway friction coefficient is highest for the first contact pressure of 750 psi which is shown in Figure 5.13.

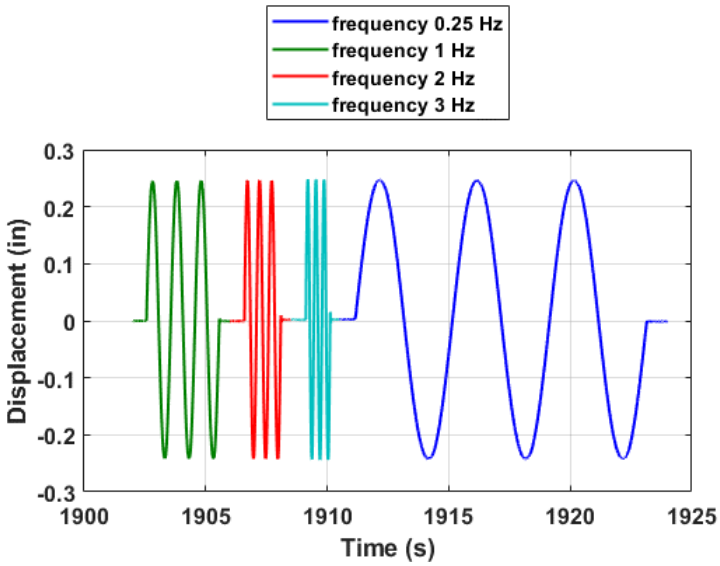

Figure 5.10. Test HSR_D_S2_P2_SP1: sliding displacement of the intermediate concrete prism

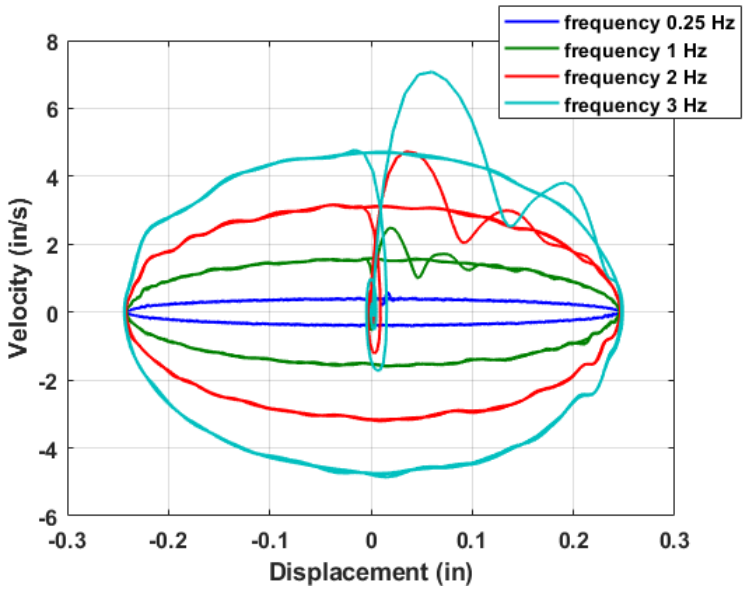

Figure 5.11. Test HSR_D_S2_P2_SP1: sliding velocity vs. sliding displacement

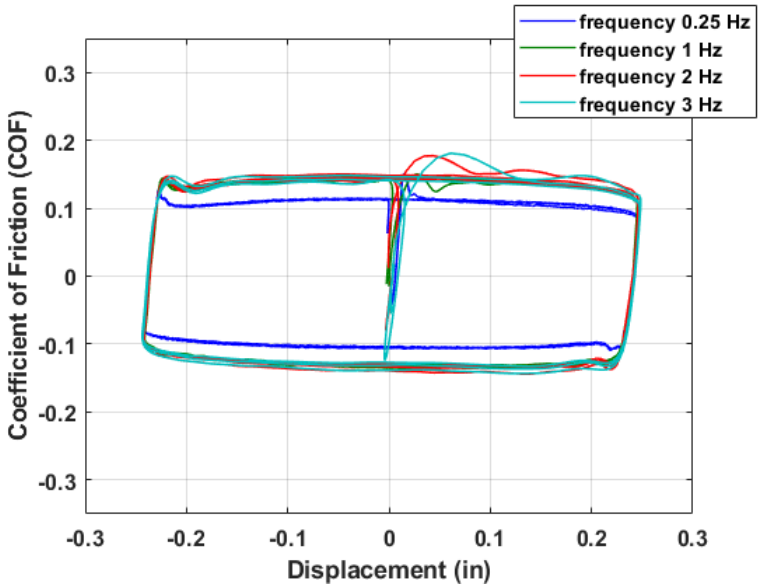

Figure 5.12. Test HSR_D_S2_P2_SP1: coefficient of friction vs. sliding displacement at contact pressure 500 psi

Figure 5.12 shows a kinetic COF of approximately 0.15 at high velocities, which is higher than the kinetic COF (~0.1) in Figure 5.8. The reason for this difference in COF at same contact pressure could be due to the wear in HSR_D_S2_P2_SP1 specimen as it has already experienced 36 cycles of sliding motion.

No significant difference can be observed in the overall frictional response of the two specimens with different testing sequences. It can be concluded from Figure 5.9 and Figure 5.13 that both the breakaway COF and kinetic COF decrease with increasing pressures, with the exception that the breakaway COF is highest for the first cycle in the testing sequence irrespective of the contact pressure and frequency of loading. The observed kinetic coefficients of friction for dry interfaces can be compared to the values in literature, where the kinetic coefficient of friction for plain PTFE-on-PTFE was reported as 0.13 (Vaziri et al., 1988).

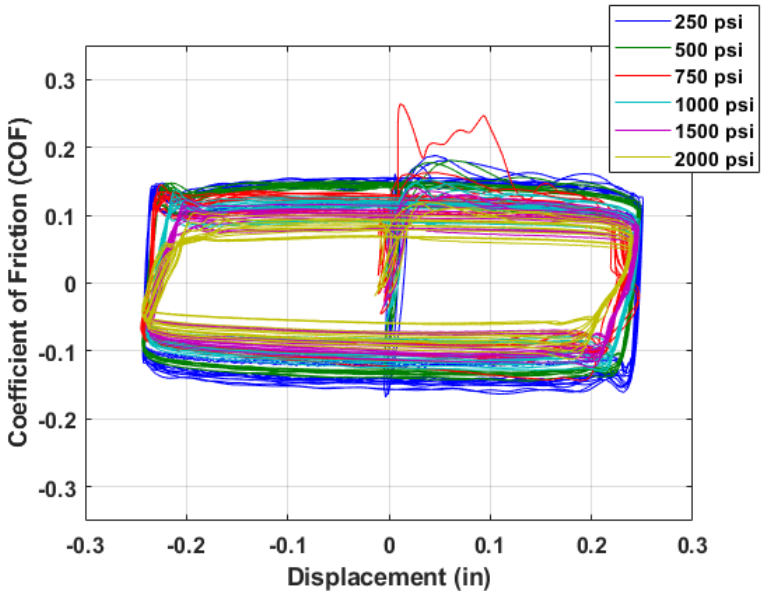

Figure 5.13. Test HSR_D_S2_P2_SP1: coefficient of friction vs. sliding displacement for all contact pressures

5.4.3. Lubricated Interfaces with Pressure Protocol P1

A total of six specimens were tested by lubricating the interfaces with two different grades of same grease. Figure 5.14 and Figure 5.15 show the plots of COF vs. sliding velocity for an individual contact pressure of 500 psi and all contact pressures respectively of HSR_L_S1_P1_SP1_G1 test which had grade-1 grease, while Figure 5.16 and Figure 5.17 show the frictional response of HSR_L_S1_P1_SP1_G2 test, which used grade-2 grease for lubrication. The stick-slip phenomenon is minimal in the lubricated specimens compared to the dry interfaces and the COF vs. sliding displacement hysteresis has a smooth transition at loading reversals.

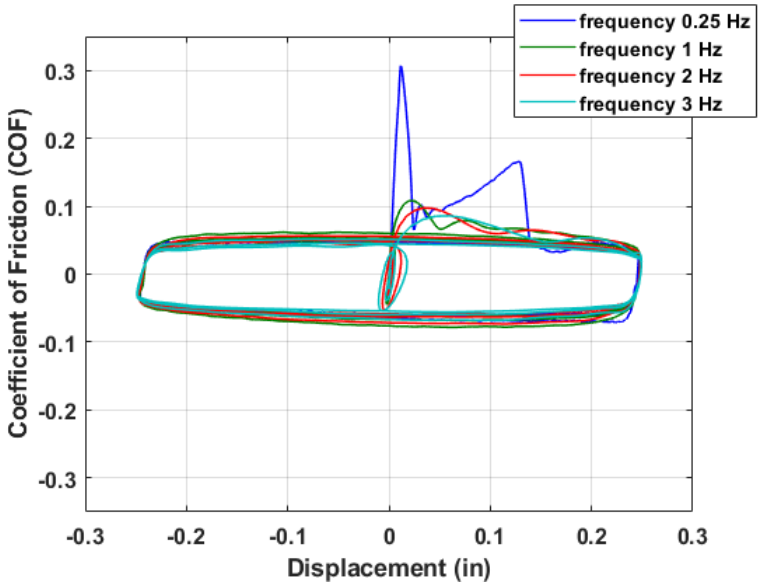

Figure 5.14. Test HSR_L_S1_P1_SP1_G1: coefficient of friction vs. sliding displacement at contact pressure 500 psi

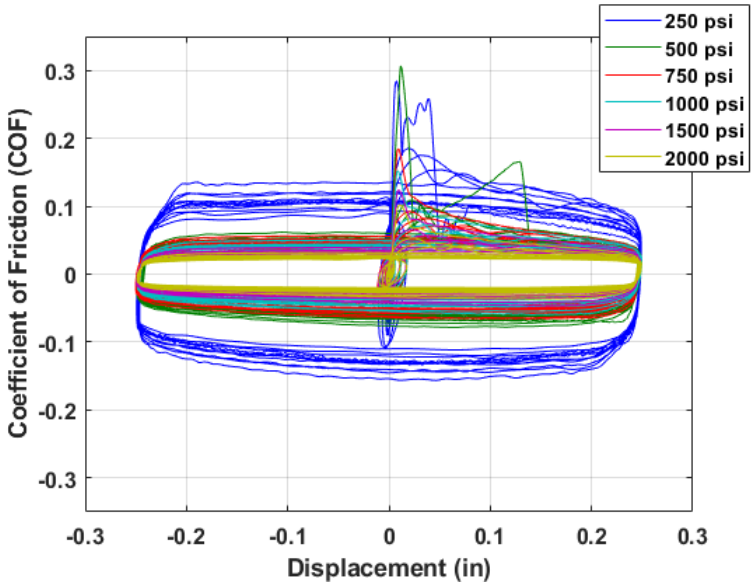

Figure 5.15. Test HSR_L_S1_P1_SP1_G1: coefficient of friction vs. sliding displacement for all contact pressures

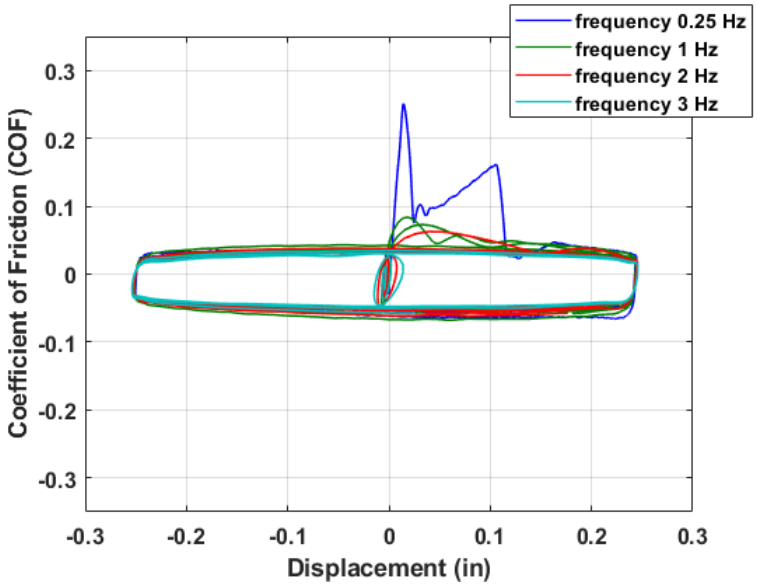

Figure 5.16. Test HSR_L_S1_P1_SP3_G2: coefficient of friction vs. sliding displacement at contact pressure 500 psi

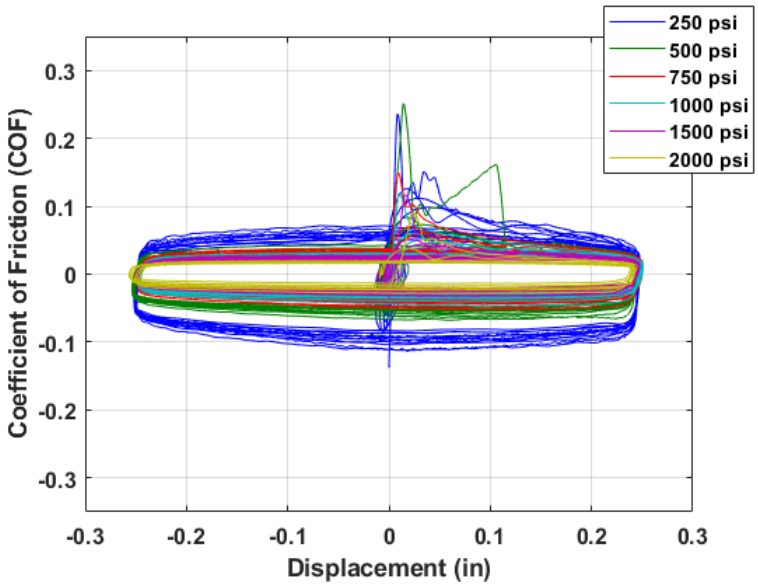

Figure 5.17. Test HSR_L_S1_P1_SP3_G2: coefficient of friction vs. sliding displacement for all contact pressures

Comparison of the above plots show a relatively lower coefficient of breakaway friction and kinetic friction for specimen lubricated with grade-2 grease, because of its

ability to retain between the sliding surfaces and superior performance at high pressures compared to the grade-1 grease. After examining the plots from both dry and lubricated interface tests, it can be concluded that lubrication decreases the coefficient of kinetic friction approximately by 50%.

5.4.4. Observations

Most of the specimens experienced either no damage or minimal damage. The minimal damage was concrete spalling at the edges in the form of small dust particles for higher contact pressures in the case of dry interfaces. The epoxy bond between concrete-steel and steel-PTFE had not experienced any damage for all the specimens tested even at large pressures and sliding velocities. Post visual inspection of the specimen after the whole testing sequence revealed a large amount of wear on the dry PTFE surfaces as compared to the lubricated surfaces which had not experienced any wear, however the grease used for lubrication was squeezed towards the boundaries of the specimen's sliding surfaces (Figure 5.18). The wear or damage to the top sliding surface material may have affected the frictional response of the interface, however, the variation of COF with wear is not investigated in this research.

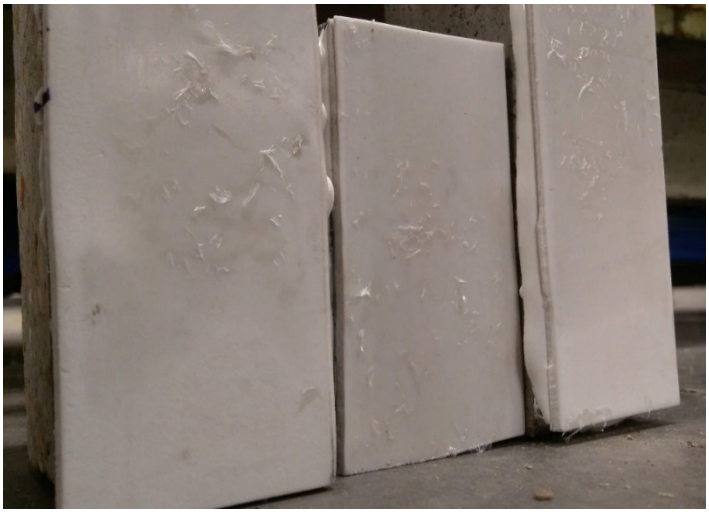

(a)

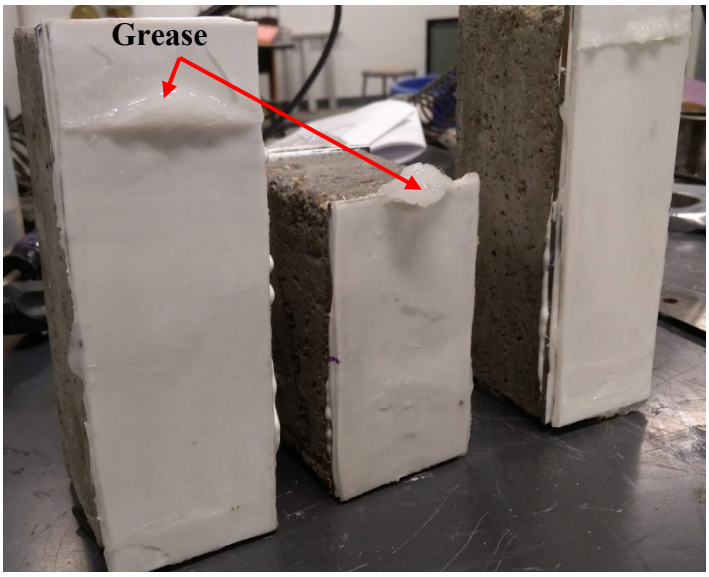

(b)

Figure 5.18. PTFE interfaces after testing (a) dry interface; (b) lubricated interface

5.4.5. Effect of Normal Pressure, Sliding Velocity and Lubrication on the Coefficient of Friction

In order to investigate the effects of normal pressure, sliding velocity and lubrication on the coefficient of friction of the PTFE-on-PTFE interfaces, selective data

points are picked from the overall frictional response recorded for each test specimen. The data points at zero and maximum displacement are chosen and the corresponding values of coefficient of friction, normal pressure and sliding velocity are stored as shown in Figure 5.19. Maximum sliding velocity occurs at zero displacement and the points corresponding to negative frictional force are chosen. These points are located on the mid region of the bottom edge in the COF-Sliding displacement loop. The maximum displacement is observed twice in each cycle in the positive and negative direction where the velocity becomes zero instantaneously. These points are located on the top right corner and bottom left corner which are diagonally opposite on the COF-Sliding displacement loop.

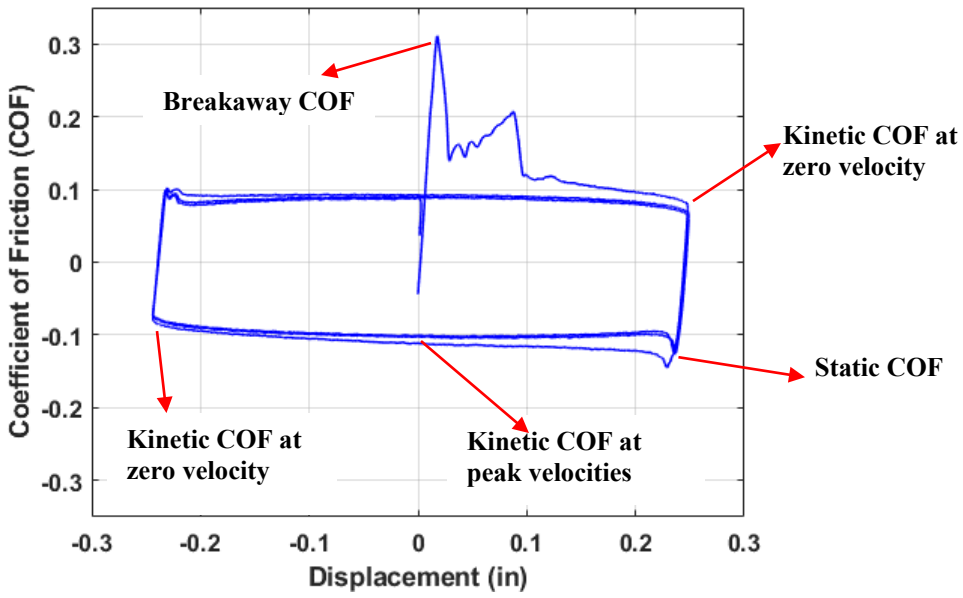

Figure 5.19. Location of data points used in curve fitting

In order to observe the effect of normal pressure, the data points corresponding to zero displacement/maximum sliding velocity are fitted into a three-parameter exponential law given by (5-1)

$$\mu = \mu_{min} + (\mu_{max} - \mu_{min})exp(-\alpha\sigma_N) \tag{5-1}$$

where:

μ_{max} is the coefficient of friction at low pressures

μ_{min} is the coefficient of friction at high pressures

α is constant for a given velocity and other testing conditions

σ_N is the normal pressure

Three specimens were tested for each type of test, and all the data points are grouped together and used in fitting the curve as shown in Figure 5.20 and Figure 5.21.

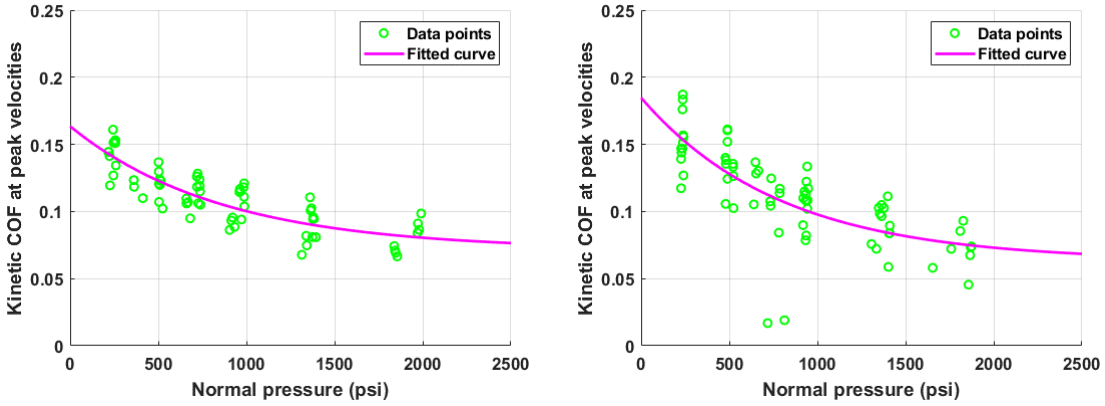

(a) (b)

Figure 5.20. Variation of coefficient of friction with normal pressure for dry interfaces (a) HSR_D_S1_P1; (b) HSR_D_S2_P2

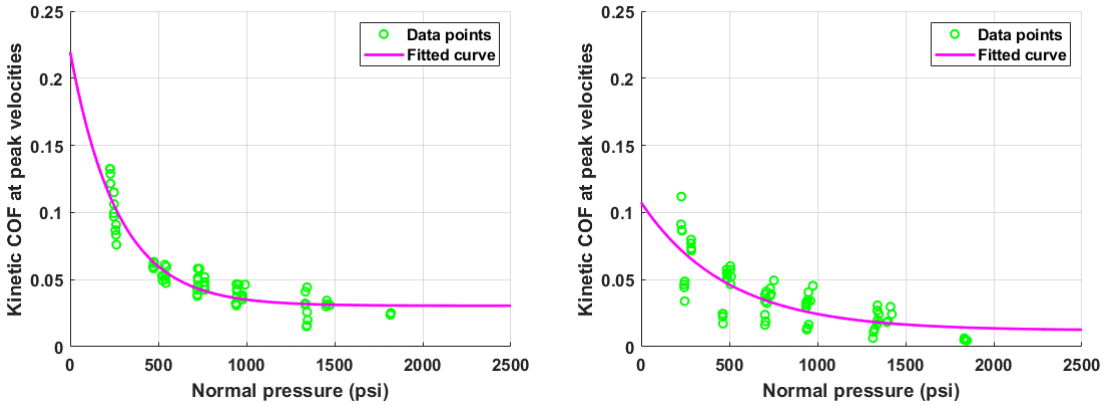

(a) (b)

Figure 5.21. Variation of coefficient of friction with normal pressure for lubricated interfaces (a) HSR_L_S1_P1_G1; (b) HSR_L_S1_P1_G2

Table 5.4. Calibrated parameters for variation of COF with normal pressure

Test	μ_{min}	μ_{max}	α
HSR_D_S1_P1	0.0584	0.1375	0.000974
HSR_D_S2_P2	0.0500	0.1866	0.001062
HSR_L_S1_P1_G1	0.0305	0.2196	0.003722
HSR_L_S1_P1_G2	0.0121	0.1074	0.002050

The plots of fitted curves and the parameters from Table 5.4 show that a decrease in the coefficient of friction with increase in normal/contact pressure. COF reduces with lubrication almost by two times with grade-1 grease and five times with grade-2 grease. The higher value of μ_{max} for lubricated tests with grade-1 grease than the dry interface tests is due to the curve fitting and projection for zero pressure as the lowest pressure tested in the experiment is only 250 psi. The reduction in COF due to increase in normal pressure is higher for low pressures and the rate of reduction decreases for high pressure ranges and approximately gets constant at pressures greater than 1500 psi.

Figure 5.22 summarizes the variation of COF with normal pressure for all test types. It can be observed that the variation in COF is minimal for both the dry interface testing types which employed two different sliding protocols and testing sequence. Lubrication has a significant effect on the variation of COF and the type of grease used also effects the frictional performance of the interface. The specimen lubricated with grade-2 grease had the minimum COF for any given pressure at maximum sliding velocity.

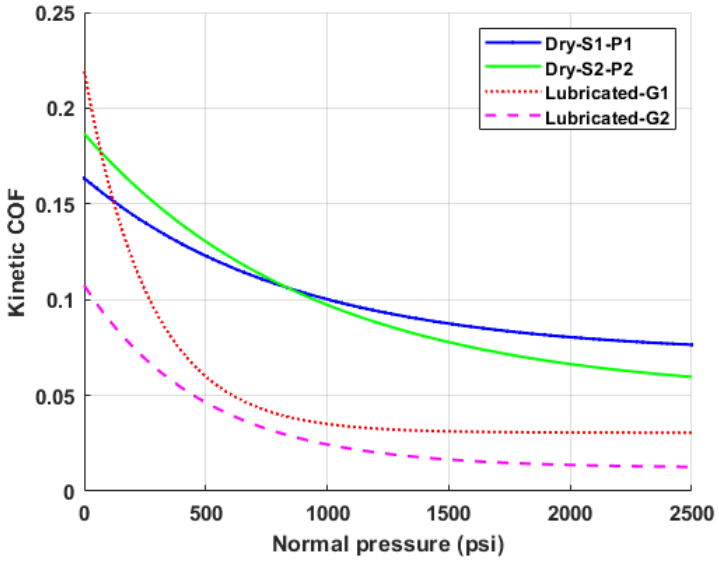

Figure 5.22. Variation of coefficient of friction with normal pressure for all test types

In order to investigate the effect of sliding velocity, similar procedure was followed. The data points corresponding to maximum sliding velocities and zero velocity at a single contact pressure are fitted into a three-parameter exponential law given by (5-2)

$$\mu = \mu_{max} - (\mu_{max} - \mu_{min}) exp(-\alpha v) \tag{5-2}$$

where:

μ_{max} is the coefficient of friction at high velocities

μ_{min} is the coefficient of friction at very low velocities

α is constant for a given normal pressure and other testing conditions

v is the sliding velocity

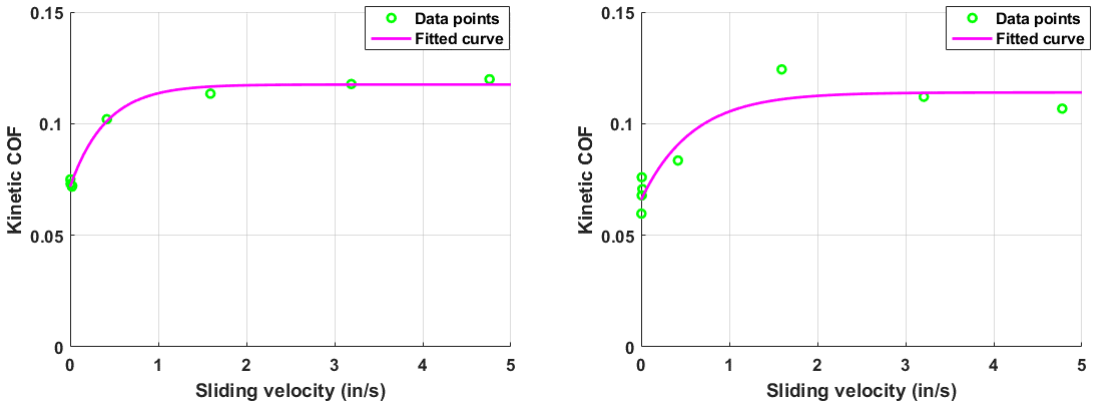

(a) (b)

Figure 5.23. Variation of coefficient of friction with sliding velocity for dry interfaces at 1000 psi contact pressure (a) HSR_D_S1_P1; (b) HSR_D_S2_P2

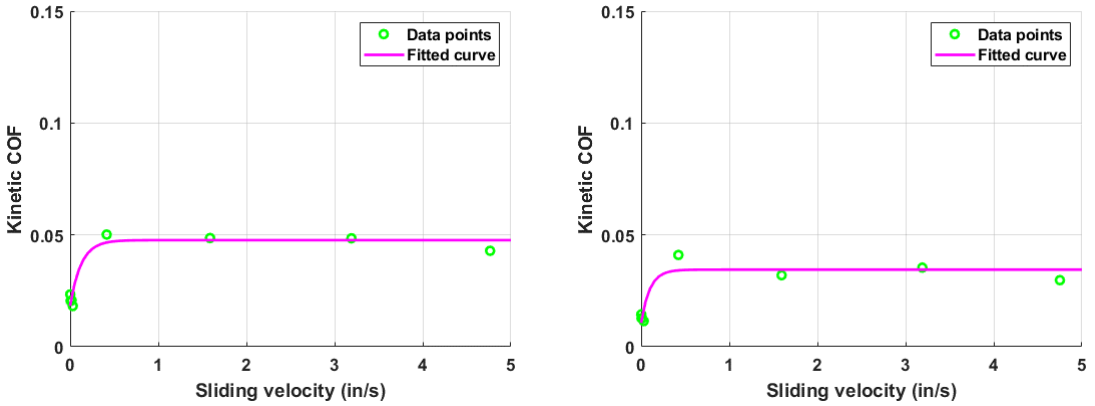

(a) (b)

Figure 5.24. Variation of coefficient of friction with sliding velocity for lubricated interfaces at 1000 psi contact pressure (a) HSR_L_S1_P1_G1; (b) HSR_L_S1_P1_G2

The fitted curves for data points corresponding to 1000 psi contact pressure are shown in Figure 5.23 and Figure 5.24. The average coefficient of friction values from the three specimens for each type were used in fitting the curves. The calibrated parameters are summarized in Table 5.5.

Table 5.5. Calibrated parameters for variation of COF with sliding velocity

Test	$\boldsymbol{\mu_{min}}$	$\boldsymbol{\mu_{max}}$	$\boldsymbol{\alpha}$
HSR_D_S1_P1	0.066606	0.10813	2.800629
HSR_D_S2_P2	0.065914	0.113983	1.724894
HSR_L_S1_P1_G1	0.015019	0.038744	10.05998
HSR_L_S1_P1_G2	0.009563	0.028211	9.266765

The plots show an increase in coefficient of friction with increase in sliding velocity and the coefficient of friction tending to be constant at high sliding velocities. It can also be observed that the COF values excluding the points closer to zero velocity show a decreasing trend with increasing velocity as the COF recorded at first cycle of each sliding protocol is higher irrespective of the sliding velocity, however the overall curve shows an increasing trend with the COF values nearly tending to be constant at velocities greater than 1 in/s.

Figure 5.25 summarizes the variation of COF with sliding velocities for all test types at a given contact pressure of 1000 psi. It can be observed that the variation in COF is minimal for both the dry interface testing types which employed two different sliding protocols and testing sequence. Looking at the figure we can also observe that the lubrication has a significant effect on the variation of COF, where the COF reduces

approximately by three times due to lubrication. The specimen lubricated with grade-2 grease had the minimum COF for a given pressure at any sliding velocity.

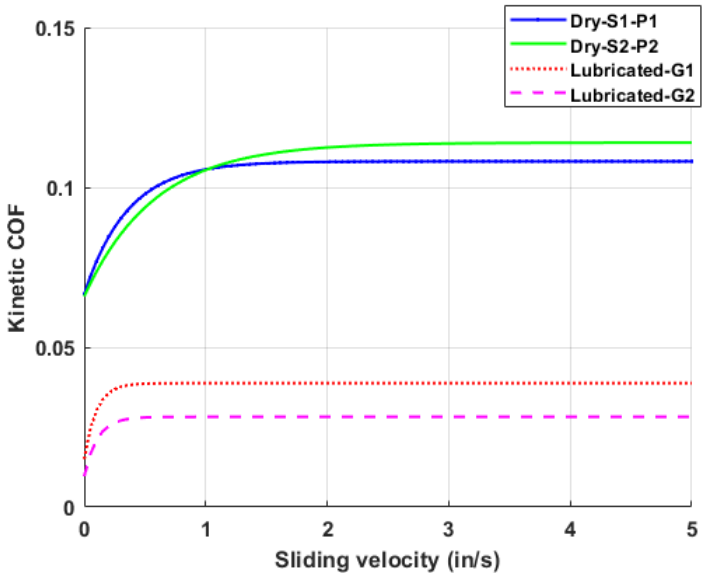

Figure 5.25. Variation of coefficient of friction with sliding velocity for all test types at 1000 psi

5.5. Numerical Model

5.5.1. Introduction

A numerical model is developed to capture the observed frictional behavior of dry and lubricated PTFE-on-PTFE interfaces tested in the experimental program. The model is developed based on the analytical model proposed by Sideris (2012) based on Bouc-Wen smooth hysteretic rule (Bouc, 1971; Wen, 1976). The following section describes the model formulation, selection of parameters for use in the model and evaluation of the developed model by comparing the analytical response with experimental results.

5.5.2. Model Description

The shear or frictional stress is given by

$$\sigma_s = \mu_{BP}\sigma_N Z \tag{5-3}$$

where, μ_{BP} is the apparent coefficient of friction, σ_N is the normal pressure and Z is a dimensionless hysteretic parameter ranging between -1 and 1, and obtained by solving the differential equation (3-8). The apparent coefficient of friction, μ_{BP} given in the equation (5-4) incorporates both breakaway coefficient of friction, μ_B, and the permanent coefficient of friction, μ_P.

$$\mu_{BP} = \mu_P + \langle \mu_B - \mu_P \rangle \, exp(-\alpha_{BP} I_{BP}) \tag{5-4}$$

where, $\langle . \rangle$ are the Macaulay brackets, and I_{BP} is the accumulated plastic travelling given by the following expression:

$$I_{BP} = \begin{cases} \int |dx| \, , |Z| \geq Z_{max} (= 0.995) \\ I_{BP}(nochange), otherwise \end{cases} \tag{5-5}$$

The breakaway coefficient of friction, μ_B, is given as a function of the normal pressure by the following equation:

$$\mu_B = \mu_{B,min} + \langle \mu_{B,max} - \mu_{B,min} \rangle \, exp(-\alpha_B \sigma_N) \geq \mu_{B,bound} \tag{5-6}$$

where, $\mu_{B,min}$ and $\mu_{B,max}$ are coefficients of breakaway friction at high and zero pressure respectively. $\mu_{B,bound}$ is the limiting value of breakaway friction at high pressures, incorporated to avoid negative coefficient of friction due to curve fitting. The permanent coefficient of friction incorporates the effects of static and kinetic friction and

their variation with the contact pressure and sliding velocity, and is given by the following expressions:

$$\mu_P = \begin{cases} \mu_{P-h} - \langle \mu_{P-h} - \mu_{P-l} \rangle \, exp(-\alpha_v |\dot{x}|) + \langle \mu_{P,st} - \mu_{P-l} \rangle \, exp(-\alpha_I I_{st}) \\ \qquad\qquad , Z\dot{x} \geq 0 \\ \mu_{P-h} - \langle \mu_{P-h} - \mu_{P-l} \rangle + \langle \mu_{P,st} - \mu_{P-l} \rangle \, exp(-\alpha_I I_{st}) \\ \qquad\qquad , Z\dot{x} < 0 \end{cases} \tag{5-7}$$

$$I_{st} = \begin{cases} \int |dx| \, , |Z| \geq Z_{max} \, (= 0.995) \\ 0 \qquad , Z = 0 (i.e. when Z_i Z_{i-1} \leq 0) \\ I_{st}(nochange), otherwise \end{cases} \tag{5-8}$$

where, μ_{P-h} and μ_{P-l} refer to the kinetic coefficient of friction at high and zero velocities, respectively, and $\mu_{P,st}$ refers to the static coefficient of friction. The parameter α_v controls the variation of coefficient of friction with velocity, while the parameter α_I controls the transition from static friction to kinetic friction. These are calibrated as a function of contact pressure using the following expressions:

$$\begin{cases} \mu_{P-l} = \mu_{P-l,min} + \langle \mu_{P-l,max} - \mu_{P-l,min} \rangle \, exp(-\alpha_{P-l} \sigma_N) \geq \mu_{P-l,bound} \\ \mu_{P-h} = \mu_{P-h,min} + \langle \mu_{P-h,max} - \mu_{P-h,min} \rangle \, exp(-\alpha_{P-h} \sigma_N) \geq \mu_{P-h,bound} \\ \mu_{P,st} = \mu_{P,st,min} + \langle \mu_{P,st,max} - \mu_{P,st,min} \rangle \, exp(-\alpha_{p,st} \sigma_N) \geq \mu_{P,st,bound} \end{cases} \tag{5-9}$$

The first order ordinary differential equation used in solving the parameter Z is essentially a Bouc-Wen rule (Bouc, 1971; Wen, 1976) and is given by the following expression:

$$\dot{Z} = \frac{K_c}{\mu_{BP} \sigma_N} [A - |Z|^n (\beta + \gamma \, sgn(Z\dot{x}))] \dot{x} \tag{5-10}$$

The parameters A, β, and γ are positive constants, with A=1, and $\beta + \gamma = 1$, always. Also, Kc is the stiffness of the response. The exponent, n, is given by the following expression:

$$n = n_{min} + (n_{max} - n_{min})\, exp(-\alpha_{BP} I_{BP}) \tag{5-11}$$

where, α_{BP} and I_{BP} are the parameters given in equations (5-4) and (5-5).

The values considered for the Bouc-Wen parameters are: $A = 1$, $\beta = \gamma = 0.5$, $n_{max} = 50$ and $n_{min} = 20$.

5.5.3. Calibration of Parameters

Discrete data points are chosen from the overall frictional response of each type of test and fitted as explained earlier in 5.4.5 and 5.5.2. Additional data points corresponding to static friction are also chosen to capture the stick-slip phenomenon observed in the frictional response observed at each cycle reversal, especially in dry interface tests. These points are located on the bottom-right corner of the COF-sliding displacement loops. The points corresponding to maximum sliding displacements are referred as points at low velocities here, as the recorded sliding velocities at these points is not exactly equal to zero. Figure 5.26 through Figure 5.29 show the curve fitting of the data points used for each type of specimen, while Table 5.6 through Table 5.9 summarize the calibrated parameters.

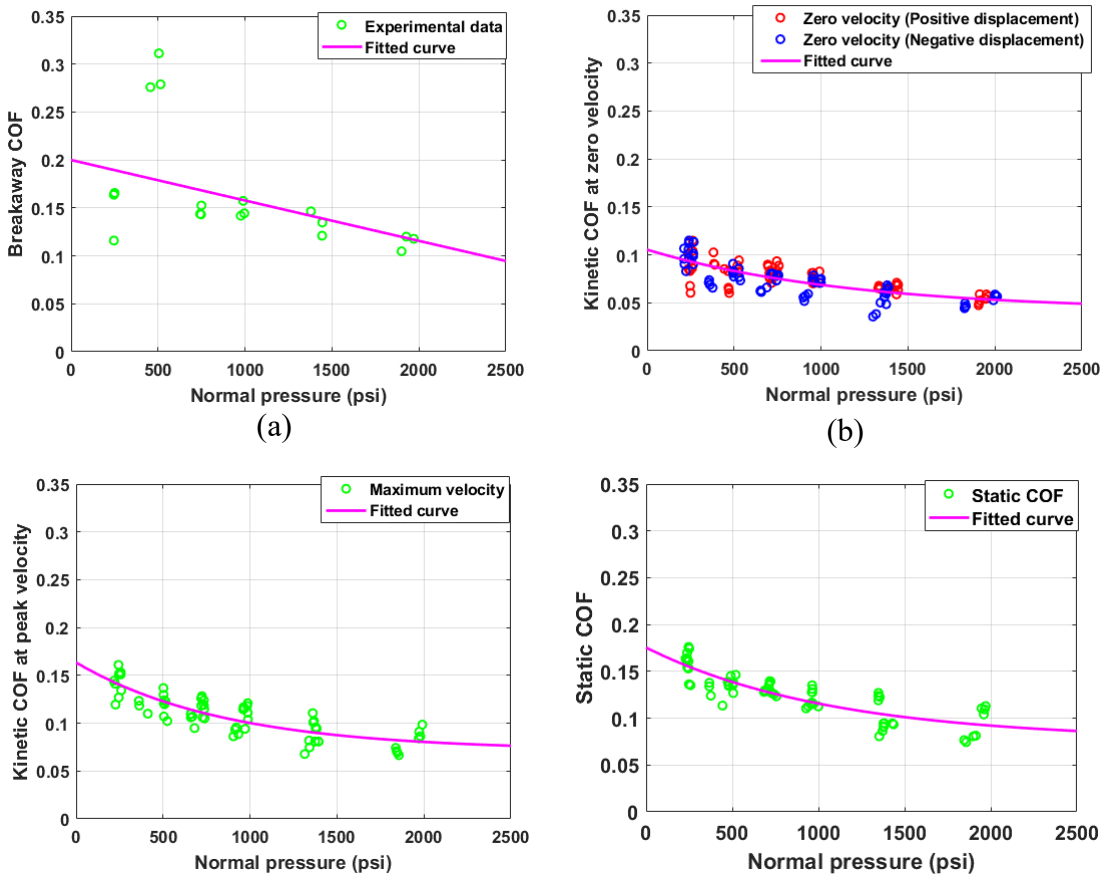

Figure 5.26. Calibration of parameters for tests HSR_D_S1_P1: (a) breakaway friction; (b) low velocities; (c) high velocities; (d) static friction

Table 5.6. Calibrated parameters of HSR_D_S1_P1

Data type	μ_{min}	μ_{max}	α	μ_{bound}
Breakaway friction (μ_B)	-11.872*	0.199	0.0000035	0.10
Low velocities (μ_{P-l})	0.041	0.105	0.0008542	0.05
High velocities (μ_{P-h})	0.071	0.163	0.0011625	0.08
Static friction ($\mu_{P,st}$)	0.076	0.175	0.0009294	0.09

* Negative value was obtained in curve fitting and as data is available only up to 2000 psi. The breakaway friction is corrected for pressures above 2000 psi by using a lower bound, $\mu_{B,bound}$.

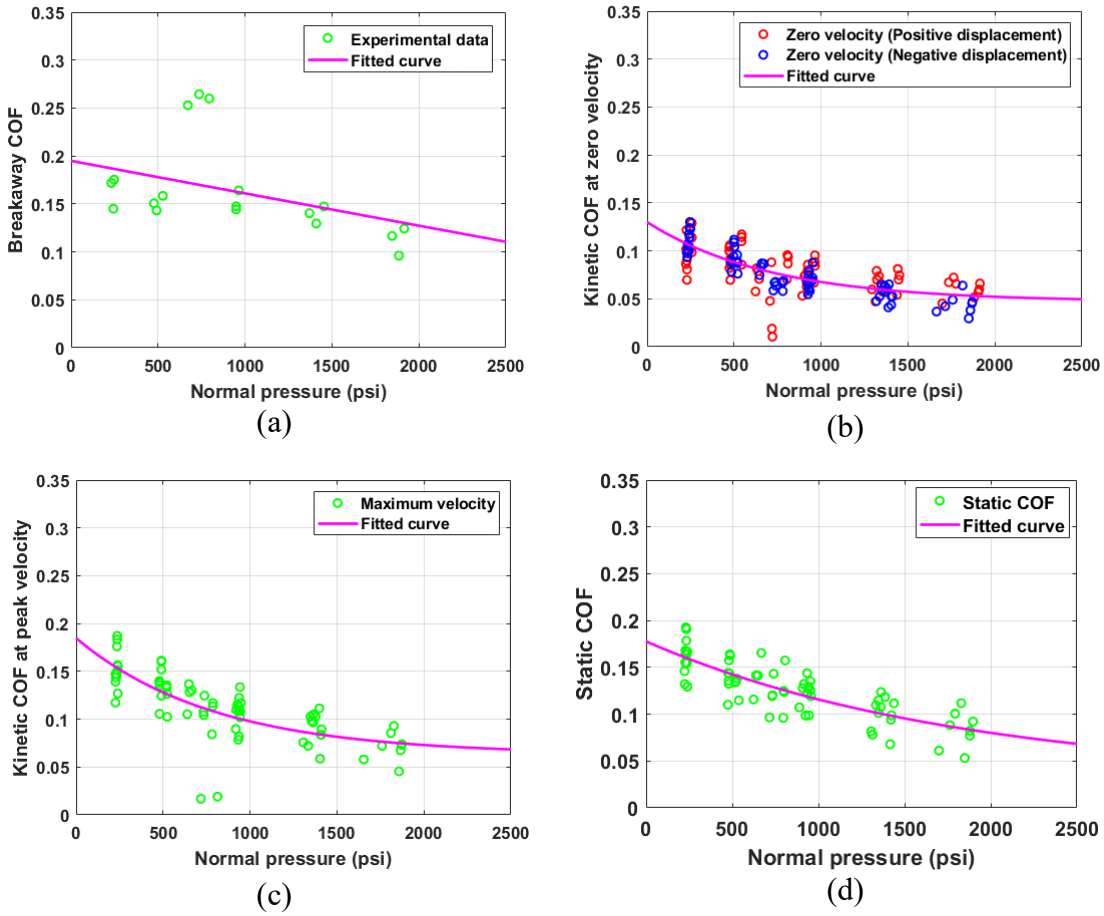

Figure 5.27. Calibration of parameters for tests HSR_D_S2_P2: (a) breakaway friction; (b) low velocities; (c) high velocities; (d) static friction

Table 5.7. Calibrated parameters of HSR_D_S2_P2

Data type	μ_{min}	μ_{max}	α	μ_{bound}
Breakaway friction (μ_B)	-5.007*	0.194	0.0000065	0.10
Low velocities (μ_{P-l})	0.047	0.129	0.0013970	0.05
High velocities (μ_{P-h})	0.063	0.184	0.0012579	0.07
Static friction ($\mu_{P,st}$)	0.031	0.177	0.0005505	0.07

* Negative value was obtained in curve fitting and as data is available only up to 2000 psi. The breakaway friction is corrected for pressures above 2000 psi by using a lower bound, $\mu_{B,bound}$.

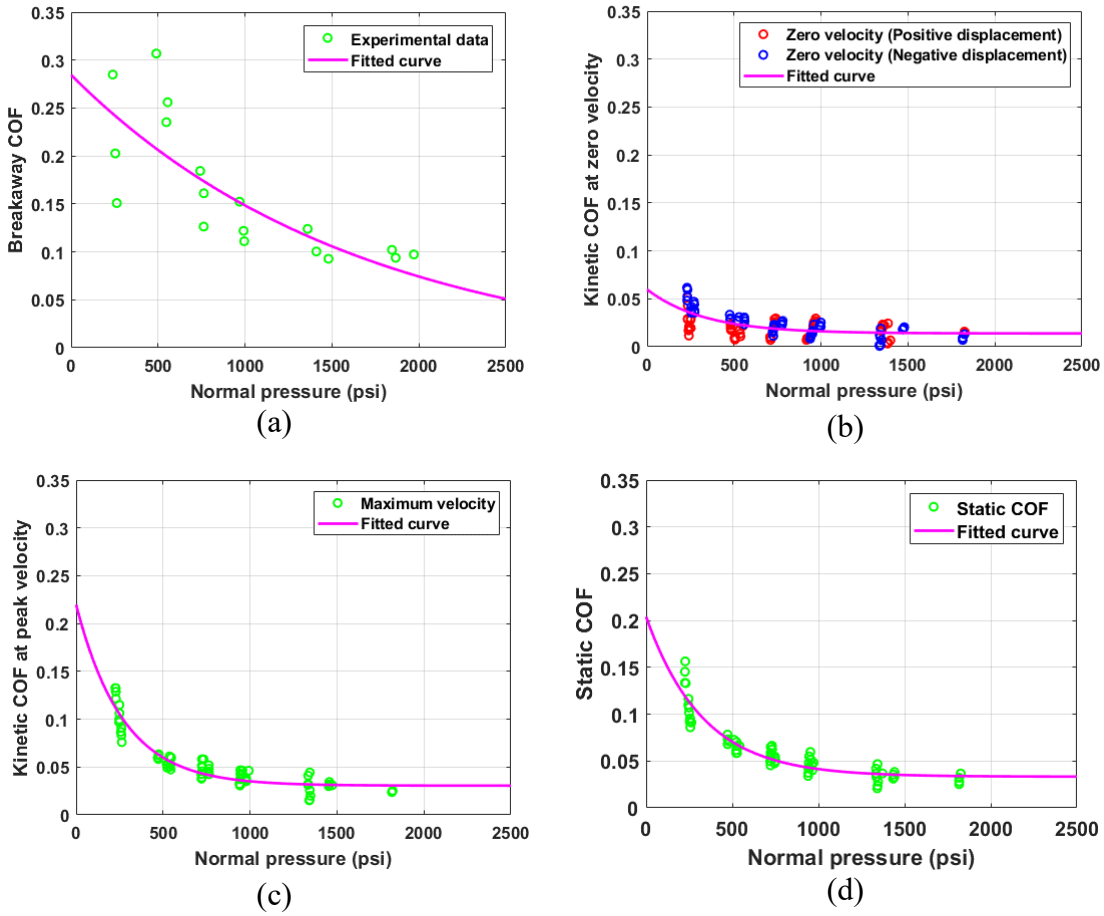

Figure 5.28. Calibration of parameters for tests HSR_L_S1_P1_G1: (a) breakaway friction; (b) low velocities; (c) high velocities; (d) static friction

Table 5.8. Calibrated parameters of HSR_L_S1_P1_G1

Data type	μ_{min}	μ_{max}	α	μ_{bound}
Breakaway friction (μ_B)	-0.014*	0.284	0.0006061	0.05
Low velocities (μ_{P-l})	0.013	0.059	0.0030261	0.015
High velocities (μ_{P-h})	0.031	0.219	0.0037222	0.03
Static friction ($\mu_{P,st}$)	0.033	0.203	0.0030434	0.03

* Negative value was obtained in curve fitting and as data is available only up to 2000 psi. The breakaway friction is corrected for pressures above 2000 psi by using a lower bound, $\mu_{B,bound}$.

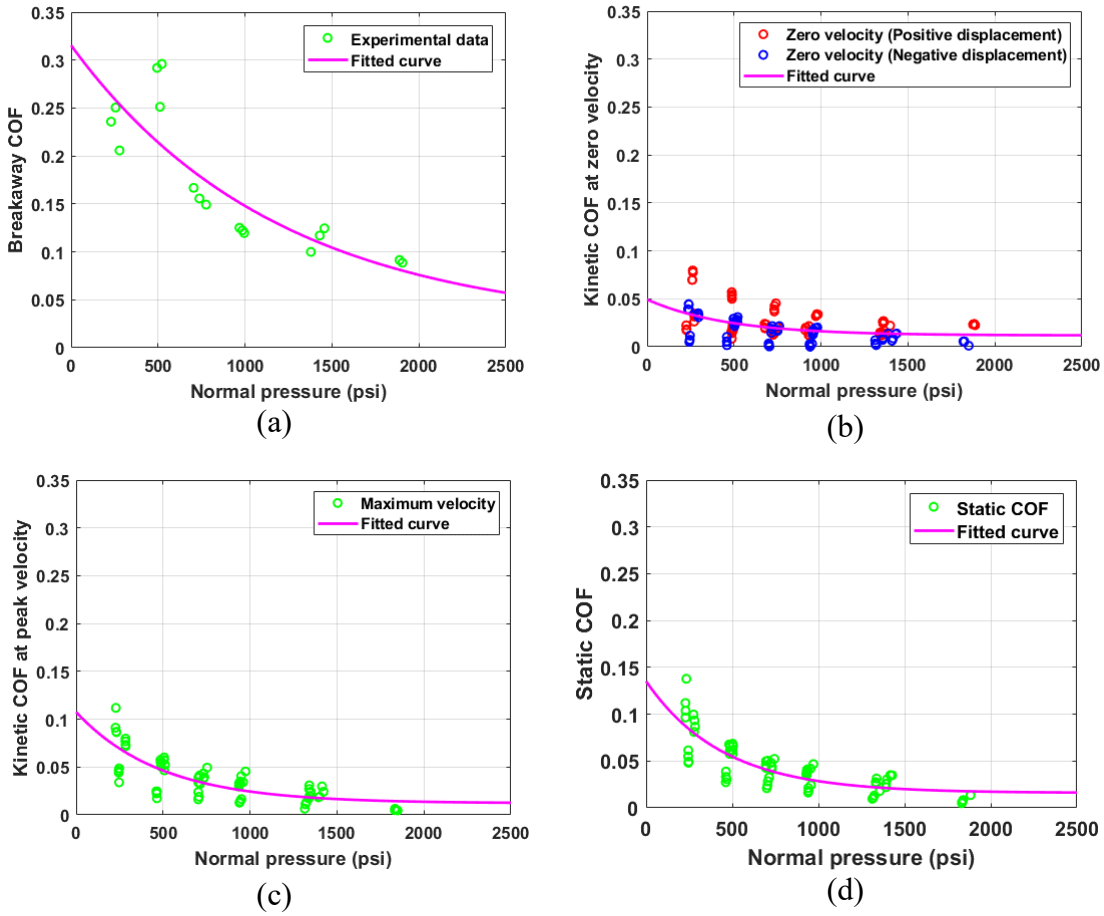

Figure 5.29. Calibration of parameters for tests HSR_L_S1_P1_G2: (a) breakaway friction; (b) low velocities; (c) high velocities; (d) static friction

Table 5.9. Calibrated parameters of HSR_L_S1_P1_G2

Data type	μ_{min}	μ_{max}	α	μ_{bound}
Breakaway friction (μ_B)	0.021	0.315	0.0008450	0.05
Low velocities (μ_{P-l})	0.011	0.049	0.0021559	0.012
High velocities (μ_{P-h})	0.012	0.107	0.0020496	0.015
Static friction ($\mu_{P,st}$)	0.015	0.135	0.0022455	0.015

5.5.4. Model Evaluation

The proposed numerical model is evaluated by comparing the frictional response captured analytically with the experimental results. The Bouc-Wen parameters are kept constant for all type of tests, while the parameters α_v, α_I and α_{BP} are chosen by a trial and error approach for each type of test. The comparison plots are presented for four tests; one from each test category at a single contact pressure chosen from the testing sequence. Figure 5.30 and Figure 5.31 show the comparison of experimental and analytical results of tests on dry interfaces with different sliding protocols and testing sequences at a contact pressure of 1000 psi. The numerical model satisfactorily captures the breakaway and static friction observed in dry interface testing. The model reasonably captures the variation of coefficient of friction with sliding velocity though the parameters are calibrated as a function of normal pressure.

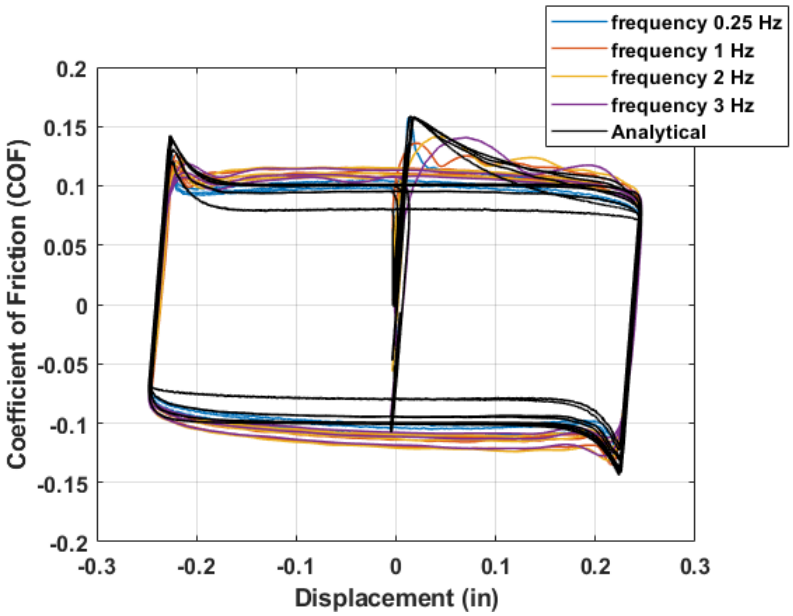

Figure 5.30. Test HSR_D_S1_P1_SP1: Comparison of experimental and analytical friction response at a contact pressure of 1000 psi

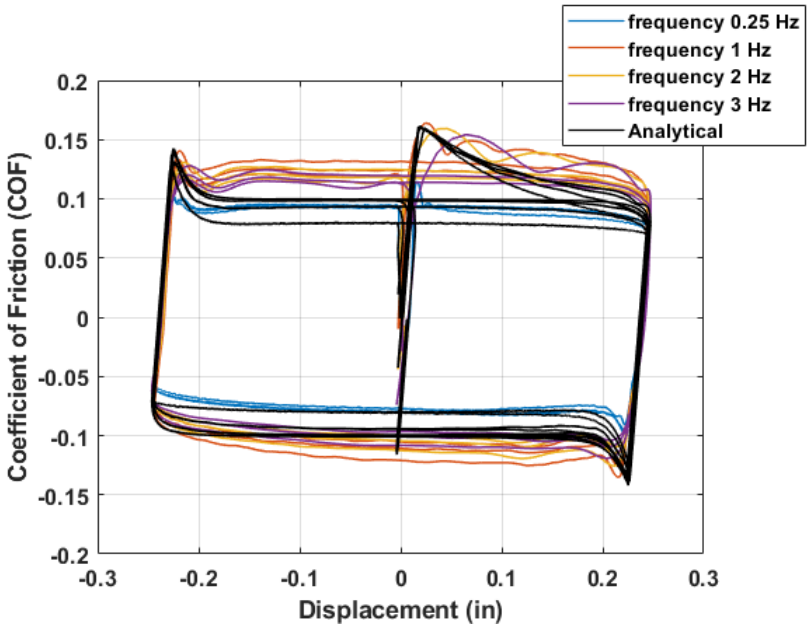

Figure 5.31. Test HSR_D_S2_P2_SP1: Comparison of experimental and analytical friction response at a contact pressure of 1000 psi

A symmetric frictional response is not observed from the experimental plots in the Figure 5.31. This could be due to the testing conditions where the faces of the concrete specimens are not perpendicular. Figure 5.32 and Figure 5.33 show the comparison of tests on lubricated interfaces with different grades of grease at a contact pressure of 750 psi. The model satisfactorily captures both the breakaway and permanent coefficient of friction.

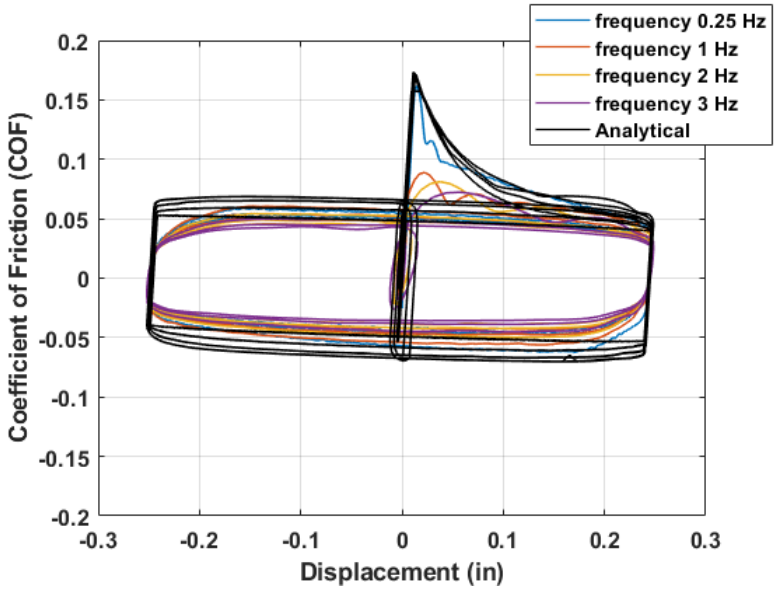

Figure 5.32. Test HSR_L_S1_P1_SP2_G1: Comparison of experimental and analytical friction response at a contact pressure of 750 psi

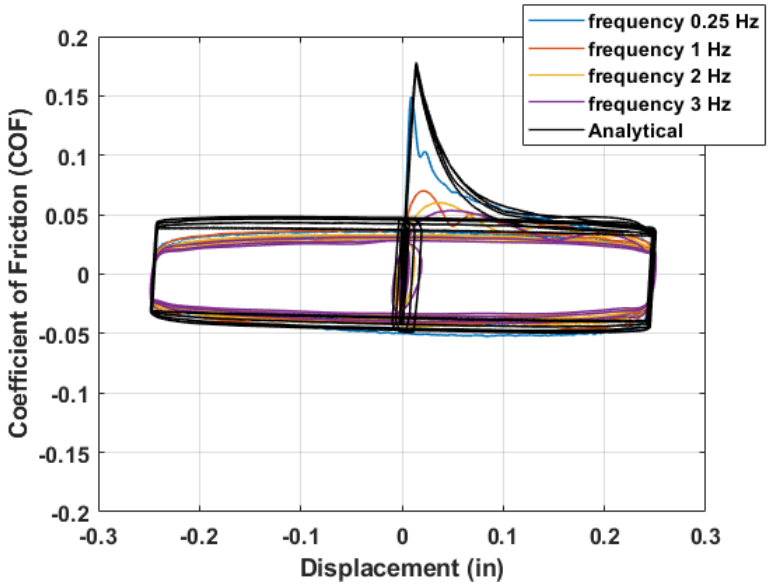

Figure 5.33. Test HSR_L_S1_P1_SP2_G2: Comparison of experimental and analytical friction response at a contact pressure of 750 psi

6. SUMMARY, CONCLUSIONS AND RECOMMENDATIONS

6.1. Summary

The research objectives were achieved by performing two tasks. The first task involved the performance evaluation and comparison of monolithic cast-in-place column bridge with skewed angle abutment and the same bridge with hybrid sliding-rocking (HSR) column. A two-span single-column bent bridge in Ripon, California was selected as the case study bridge. The bridge had an abutment skew of 33^{o} with a total length of 220ft. and two lanes of traffic. Both bridges, namely, the original bridge with a monolithic cast-in-place column, and the HSR bridge, i.e. the same bridge but with an HSR column, instead of the monolithic one, were considered with five different abutment skew angles (0^{o}, 15^{o}, 30^{o}, 45^{o} and 60^{o}) and modeled in the OpenSees structural analysis software (McKenna et al., 2000). The modeling of bridge was done according to the guidelines in Chapter 4 of Bridge Design and Practice by Caltrans (Caltrans, 2015). A gradient-inelastic flexibility-based (GI FB) beam column element (Salehi & Sideris, 2017) was used to model the monolithic column with nonlinear hysteretic models for torsion and shear to accurately predict the column behavior in time history analyses. The HSR column was designed and modeled based on the guidelines proposed by Sideris et al. (2014) and Salehi et al. (2017). Two seismic hazard levels with return periods of 1000 years and 2500 years were considered in this study as design earthquake (DE) and maximum considered earthquake (MCE). The 1971 Northridge earthquake was used as ground motion in the time history analyses by scaling it to two hazard levels. The design spectrum was

generated according to the guidelines in AASHTO (2012). A total of 20 analyses were performed, where each type of bridge with a varying skew angle was analyzed for two hazard levels. All the recorded responses were post-processed to evaluate the performance of bridges with varying abutment skew angle. A comparative study of both monolithic column bridge and HSR column bridge was carried out to evaluate the difference in response and check their damage states.

The second task was an experimental program carried out to investigate the frictional properties of PTFE-on-PTFE interfaces used in HSR joints. Four types of specimens were tested, where the first two had dry interfaces with different sliding and pressure protocols, while the third and fourth specimen types had lubricated interfaces with two grades of the same grease. The variation of coefficient of the friction with normal pressure and sliding velocity was investigated by testing the specimens for six different normal pressures (250 psi, 500 psi, 750 psi, 1000 psi, 1500 psi and 2000 psi) and four different sliding velocities by varying the frequency of sliding amplitude (0.25 Hz, 1 Hz, 2 Hz and 3 Hz). The sliding displacement was recorded using two LVDTs and the normal load and frictional force were recorded using two load cells. Each test was repeated with three different specimens and the recorded data was postprocessed to check the variation of coefficient of friction with normal pressure, sliding velocity, lubrication. The results were used to develop a friction model based on the model proposed by Sideris (2012) which incorporated the Bouc-Wen smooth hysteresis rule (Bouc, 1971; Wen, 1976). The friction model was evaluated by comparing its predictions with the experimental data.

6.2. Conclusions

The following conclusions were made based on the results obtained from both the tasks:

1. Collapse was not observed in both the monolithic bridge and HSR bridge for both 1000-yr (DE) and 2500-yr (MCE) return period hazard levels.
2. The bridge designs with skewed angle abutments, both with monolithic and HSR column have higher demands of column drift, abutment seat length and shear key strength, compared to bridge designs without skewed abutments
3. The bridge with the HSR column showed higher seismic demand in terms of peak column drift ratios, deck rotation and displacement, because of the lower torsional strength of the HSR column (approximately by a factor of 5) compared to the torsional strength of the monolithic column. This implies that either a higher coefficient of friction has to be used at the sliding interface, or that HSR column should be used in substructure bents of two or more columns, so that torsional stiffness of the bent is developed through bending action of the individual HSR columns. Unlike the monolithic column, the HSR column exhibited no cover spalling.
4. At the DE hazard level, the base shear response of the analyzed bridge with HSR column was lower than the bridge with the monolithic column, although both columns had similar strengths, because of the HSR joint sliding. The lower base shear demands result in lower force demands in the design of foundations for HSR columns.

5. For both hazard levels, lesser damage was observed in the column of HSR bridge than monolithic column bridge, where the damage was in the form of spalling of the cover concrete at MCE hazard level. Tendon yielding (in the HSR columns) was not observed for either hazard levels.
6. From the results of experimental testing on dry PTFE-on-PTFE interfaces, it was concluded that the sliding and pressure protocols had minimal effect on the overall frictional response.
7. The coefficient of friction decreased with increase in normal pressure and followed a constant trend at pressures greater than 1500 psi in case of lubricated interfaces. The coefficient of friction increased with increase in sliding velocity and any variation was not observed for velocities greater than 2 in/s.
8. Lubrication decreased the coefficient of friction significantly, approximately by 50% and an increase in coefficient of friction at sliding reversals (static COF) was *not* observed in the case of lubricated interfaces. The interfaces lubricated with grade-2 grease had the lowest coefficient of friction at any given pressure.
9. The developed friction model was in good agreement with experimental results by accounting for breakaway, kinetic and static coefficients of frictions. The model can be used for both dry and lubricated interfaces with calibrated parameters for any interface testing and can be incorporated in the modeling of HSR joints.

6.3. Recommendations for Future Research

The work in this thesis is limited to two-span single-column bent bridge with all analyses performed using a single ground motion. Hence, the results cannot be generalized to all bridge types. The following list outlines some of the recommendations for future research in both seismic analysis of HSR column bridges with skewed angle abutments and frictional testing.

1. Multiple ground motions are required in the time history analyses of HSR column bridges to account for uncertainties related to the ground shaking, and allow more general conclusions.
2. Analyses of bridges with multiple column bents and multiple spans with/without skewed angle abutments. Also, for the two-span bridge of this study, further HSR column designs should be explored, including a higher coefficient of friction.
3. More advanced models are necessary in the modeling of both monolithic and HSR columns to evaluate the shear damage in columns. Models combining shear and flexural interactions are scarce.
4. The variation of coefficient of friction of PTFE-on-PTFE interfaces with wear and temperature at contact pressures and sliding velocities, exceeding the range investigated in this study, is required.

REFERENCES

AASHTO. (2012). AASHTO LRFD Bridge Design Specifications. *American Association of State Highway and Transportation Officials, Washington, D.C.*

Ala, N., Power, E. H., & Azizinamini, A. (2016). Experimental Evaluation of High-Performance Sliding Surfaces for Bridge Bearings. *Journal of Bridge Engineering*, *21*(2), 04015034.

Aviram, A., Mackie, K. R., & Stojadinovic, B. (2008). Guidelines for Nonlinear Analysis of Bridge Structures in California (Report PEER 2008/3). *Pacific Earthquake Engineering Research Center, University of California, Berkeley, CA.*

Baker, J. W., & Cornell, C. A. (2006). Which Spectral Acceleration Are You Using? *Earthquake Spectra*, *22*(2), 293–312.

Bouc, R. (1971). A Mathematical Model for Hysteresis. *Acta Acustica United with Acustica*, *24*(1), 16–25.

Caltrans. (2013). Seismic Design Criteria Version 1.7. *California Department of Transportation, Sacramento, CA*.

Caltrans. (2015). Bridge Design Practice. *California Department of Transportation, Sacramento, CA*.

Chen, J., Han, Q., Liang, X., & Du, X. (2017). Effect of Pounding on Nonlinear Seismic Response of Skewed Highway Bridges. *Soil Dynamics and Earthquake Engineering*, *103*, 151–165.

Chopra, A. K. (2012). *Dynamics of Structures: Theory and Applications to Earthquake Engineering* (4th ed.). New Jersey, NJ: Prentice Hall.

Dolce, M., Cardone, D., & Croatto, F. (2005). Frictional Behavior of Steel-PTFE Interfaces for Seismic Isolation. *Bulletin of Earthquake Engineering*, *3*(1), 75–99.

JRA. (1996). Design Specifications of Highway Bridges, Part V: Seismic Design. *Japan Road Association, Tokyo, Japan*.

Karthik, M. M., & Mander, J. B. (2010). Stress-Block Parameters for Unconfined and Confined Concrete Based on a Unified Stress-Strain Model. *Journal of Structural Engineering*, *137*(2), 270–273.

Kaviani, P., Zareian, F., & Taciroglu, E. (2014). Performance-Based Seismic Assessment of Skewed Bridges (Report PEER 2014/1). *Pacific Earthquake Engineering Research Center, University of California, Berkeley, CA*.

Mander, J. B., Priestley, M. J. N., & Park, R. (1988). Theoretical Stress-Strain Model for Confined Concrete. *Journal of Structural Engineering*, *114*(8), 1804–1826.

Mattock, A. H. (1979). Flexural Strength of Prestressed Concrete Sections by Programmable Calculator. *PCI Journal*, *24*(1), 32–54.

McKenna, F., Fenves, G. L., Scott, M. H., & Jeremic, B. (2000). Open System for Earthquake Engineering Simulation (OpenSees). *University of California, Berkeley, CA*.

Mondal, T. G., & Prakash, S. S. (2015). Improved Softened Truss Model for RC Circular Columns Under Combined Torsion and Axial Compression. *Magazine of Concrete Research*, *67*(16), 855–866.

Prakash, S. S., Li, Q., & Belarbi, A. (2012). Behavior of circular and square reinforced concrete bridge columns under combined loading including torsion. *ACI Structural Journal*, *109*(3), 317–327.

Salehi, M., & Sideris, P. (2017). Refined Gradient Inelastic Flexibility-Based Formulation

for Members Subjected to Arbitrary Loading. *Journal of Engineering Mechanics*, *143*(9), 04017090.

Salehi, M., Sideris, P., & Liel, A. B. (2017). Numerical Simulation of Hybrid Sliding-Rocking Columns Subjected to Earthquake Excitation. *Journal of Structural Engineering*, *143*(11), 04017149.

Sideris, P. (2012). *Seismic analysis and design of precast concrete segmental bridges*. (Doctoral dissertation). Available from ProQuest Dissertations and Theses. (UMI No. 3541300).

Sideris, P., Aref, A. J., & Filiatrault, A. (2014a). Large-Scale Seismic Testing of a Hybrid Sliding-Rocking Posttensioned Segmental Bridge System. *Journal of Structural Engineering*, *140*(6), 04014025.

Sideris, P., Aref, A. J., & Filiatrault, A. (2014b). Quasi-Static Cyclic Testing of a Large-Scale Hybrid Sliding-Rocking Segmental Column with Slip-Dominant Joints. *Journal of Bridge Engineering*, *19*(10), 04014036.

Sideris, P., & Salehi, M. (2016). A Gradient Inelastic Flexibility-Based Frame Element Formulation. *Journal of Engineering Mechanics*, *142*(7), 04016039.

Vaziri, M., Stott, F. H., & Spurr, R. T. (1988). Studies of the Friction of Polymeric Materials. *Wear*, *122*(3), 313–327.

Wang, L., & Helwig, T. A. (2008). Stability Bracing Requirements for Steel Bridge Girders with Skewed Supports. *Journal of Bridge Engineering*, *13*(2), 149–157.

Wen, Y. K. (1976). Method for Random Vibration of Hysteretic Systems. , ASCE, 102 (EM2). *Journal of the Engineering Mechanic Division*, *102*(2), 249–263.